Analysis of rotational energy of nuclei with semi-realistic interaction

January 2023

Kohei Abe

Department of Physics,
Division of Advanced Science and Engineering,
Graduate School of Science and Engineering,
CHIBA UNIVERSITY

(千葉大学審査学位論文)

Analysis of rotational energy of nuclei with semi-realistic interaction

January 2023

Kohei Abe

Department of Physics,
Division of Advanced Science and Engineering,
Graduate School of Science and Engineering,
CHIBA UNIVERSITY

Abstract

The rotational band is a well-known energy spectrum in nuclear physics, which is interpreted as a rotation of the deformed intrinsic state of nuclei. In the classical mechanics, the rotational energy arises from the kinetic energy, while the rotation in the quantum many-body systems is treated by the angular-momentum projection, where interactions between constituent particles could affect it.

The M3Y-type interactions have been developed as semi-realistic nucleonic interactions, which are treated on the mean-field (MF) calculations with the Gaussian expansion method. According to the MF calculations with the M3Y-type interactions, it has been revealed that the magic number, the shell structure, and the deformation of nuclei are almost consistent with experiments over a wide range of the nuclear chart.

In this study, the angular-momentum projection (AMP) calculations have been newly implemented for the axially-deformed MF solutions with the semi-realistic effective Hamiltonian, M3Y-P6. In order to understand the rotational energy of the quantum many-body systems, the rotational energy of even-even nuclei for the fixed intrinsic state has been analyzed. The rotational energy is decomposed into the constituent terms of the Hamiltonian, and their ratios to the total rotational energy are calculated.

In the case of the HF solutions, except for light or weakly-deformed nuclei, the ratios of the individual terms of the Hamiltonian are insensitive to nuclides and deformation. The contributions of kinetic energies are large and close to the rigid-rotor values, although those of central forces are sizable. For light or weakly-deformed nuclei, the ratios significantly depend on nuclei and deformation. The contributions of non-central forces are not negligible. Regardless of nuclides, the attractive forces decrease the moment of inertia, and the repulsive forces increase it.

The pair correlations significantly change the composition of the rotational energy, especially the contributions of the effective interactions to the rotational energy. The nucleons spread as the angular momentum increases, while the pair correlations can reduce or change the effect.

A general formula for the rotational energy with axial symmetry is derived on the basis of the AMP, which suggests that higher-order terms of the cumulant expansion play roles in the rotational energy and the moment of inertia for light or weakly-deformed nuclei.

Contents

Chapter 1

Introduction

1.1 Background

In nuclear physics, the rotational band [1] is a well-known energy spectrum near the ground state of even-even nuclei, $E_{\rm x}(J^+) \approx J(J+1)/(2\mathcal{I})$, $J^\pi = 0^+, 2^+, 4^+, \cdots$. It is observed experimentally over a wide range of the nuclear chart, including not only stable nuclei but also unstable ones [2]. It indicates that the intrinsic state of nuclei is deformed and rotates with the moment of inertia $\mathcal{I}$.

From a microscopic standpoint, nuclei have been described self-consistently by the mean-field (MF) theory, such as the Hartree-Fock (HF), the HF+Bardeen-Cooper-Schrieffer (BCS), and the Hartree-Fock-Bogoliubov (HFB) approximations [3]. Because nuclei are isolated systems, the nuclear Hamiltonian has rotational symmetry, and the angular momentum is a good quantum number in energy eigenstates. However, spontaneous breaking of the rotational symmetry often occurs in the MF approximation. The rotational symmetry breaking of the MF state corresponds with a deformation of the intrinsic state. The deformed intrinsic state in nuclei is not observed directly. The Nambu-Goldstone (NG) mode is accompanied by the symmetry breaking, and it restores the corresponding symmetry in energy eigenstates. The restoration of the rotational symmetry corresponds with a whole rotational motion of the deformed nuclei.

Several methods that treat the rotation of nuclei have been developed. As a microscopic theory, the cranking model [3] has been proposed. The Inglis formula [4] and the Belyaev formula [5] have been derived for the moment of inertia from the cranking model. The Thouless-Valatin (TV) formula [6] has been obtained in connection to the random phase approximation (RPA). The angular-momentum projection (AMP) has been developed [3, 7–19], in which the degenerate intrinsic states along the NG mode are superposed. The $J(J+1)$ rule of the excitation energy with the moment of inertia is derived from the AMP under a reasonable approximation for well-deformed heavy nuclei [3, 7, 8, 10, 11, 13]. However, for light or weakly-deformed nuclei, it is not sufficiently clear whether the same arguments hold. It should also be noted that the rotation significantly affects the intrinsic state, as handled in the cranking model [3, 9, 13] and the variation after projection (VAP) schemes [3].

In the classical mechanics, the rotational energy arises from the kinetic energy. On the other hand, the rotational energy of nuclei should be formed from the effective Hamiltonian including the nucleonic interaction. In principle, the nucleonic interaction

originates from the quantum chromodynamics (QCD) [20]. However, it is not yet easy to derive the nucleonic interaction from the QCD which is applicable to a variety of nuclei with good accuracy. Because the nucleonic interactions are effectively mediated by mesons, they are represented by the Yukawa functions [21]. The Michigan-three-range-Yukawa (M3Y)-type interactions [22–28] are composed of the Yukawa functions except for density-dependent terms. The parameters of the effective interactions have been determined based on the G-matrix with some phenomenological modifications [27]. In this respect, the M3Y-type interactions are *semi-realistic* effective interactions. The tensor force is also included, whose parameters are fixed from the G-matrix. It has been pointed out via the nuclear matter response functions that the M3Y-type interactions are free from most of the instabilities, which sometimes occur in other interactions [29]. The MF calculations using the M3Y-P6 have described well the magic number of nuclei over a wide range of the nuclear chart [30] and the deformation of nuclei [31, 32].

1.2 Motivation

We explain the motivation for studying the rotational energy of nuclei.

The rotational energy of the rigid rotor is the kinetic energy in the classical mechanics. On the other hand, the rotational energy of atomic nuclei could be composed of not only the kinetic energy but also the nucleonic interaction, which is treated by the AMP. Many AMP calculations have already been done by using the phenomenological nucleonic interaction with small configuration spaces, *e.g.*, in Refs. [16, 33–35], or without truncation of the model space, *e.g.*, by using the Skyrme interaction [36, 37] or the Gogny interaction [38]. However, since their interactions are fully phenomenological nucleonic interactions, components of the rotational energy have not been investigated yet by separating the rotational energy into constituent terms of the Hamiltonian of nuclei. The study of the rotational energy by using a more realistic nucleonic interaction is desired. The nucleonic interactions, which are able to achieve the accuracy for the systematic nuclear-structure calculations, have not yet been perfectly established. There will be some feedback on the interaction by examining the contributions of the individual terms of the effective Hamiltonian to the rotational energy.

The AMP is regarded as a method of the symmetry restoration [3, 19], which is also considered in other mesoscopic systems beyond atomic nuclei, including artificial atoms and molecules, *e.g.*, quantum dots, trapped ultracold neutral atomic gases and ions, [1] where the finite-size effects of the systems are not negligible [19]. We would like to shed light on some unknown aspects of the rotation of quantum many-body systems. Since nuclei have complicated quantum correlations, including both deformation and pair correlations, it is interesting to re-examine the contributions of the nucleonic interaction to the rotational energy.

The framework of the symmetry restoration including the AMP is well established in terms of the group theory [18, 19] and often regarded as one of the generator coordinate method (GCM) [19]. The AMP is often regarded as a superposition of the rotated HF or HFB states with the Euler angles and is interpreted as a collective rotational motion

[1] The artificial atoms and molecules seem to be related to the quantum information science [19].

of the deformed intrinsic states. In the case of the rotational symmetry for the MF state is broken substantially, the Yoccoz moment of inertia [7, 8] is derived approximately from the AMP under the Gaussian approximation. However, it is not sufficiently clear whether the same argument holds particularly for the light or the weakly-deformed nuclei. We would like to present a general formula for the rotational energy and the moment of inertia derived on the basis of the AMP.

1.3 Purpose

We explain the purpose of the present study.

Under the backgrounds in Sec. 1.1 and the motivations in Sec. 1.2, we shall re-examine from the microscopic point of view how the rotational energy of quantum many-body systems including nuclei is formed. The author and H. Nakada have newly developed the source code of the AMP calculation by using the Gaussian expansion method (GEM) with the M3Y-type interactions. The AMP is applied to the MF wave functions obtained by self-consistent axial-MF calculations by using the M3Y-type interactions for the first time. In the present study, the rotational energies arising from a fixed intrinsic state are inspected. Namely, we restrict ourselves to the energies arising solely from the rotation of the intrinsic state, separating them out from the effects of the rotation on the intrinsic state in this study. In this paper, we call this energy *pure rotational energy*. For the axially-deformed HF solutions, the pure rotational energy is called *Peierls-Yoccoz rotational energy* in Ref. [39]. It should be kept in mind that the pure rotational energy is often not enough to describe the rotational spectra in actual nuclei [9]. The contributions of the individual terms of the semi-realistic Hamiltonian to the rotational energy for the fixed intrinsic state are focused on; in concrete, those of the kinetic energy, the density-independent and dependent central forces, the LS force, the tensor force, and the central part of the one-pion-exchange-potential (OPEP), which is the longest-range term and an example of spin-dependent channels. It is noted that the nucleonic interactions have spin-dependence, both in these central and noncentral channels, which could contribute to the rotational energy.

Additionally, we derive a general formula for the rotational energy and the moment of inertia with axial symmetry on the basis of the AMP in order to understand the rotational energy for light or weakly-deformed nuclei.

1.4 Advantage and characteristic

We explain advantages and characteristics of the present study.

The AMP calculations have been implemented by using the GEM with the M3Y-type interactions for the first time. Since there had been no source code of the AMP calculation by using the GEM with the M3Y-type interactions, we have newly developed it from scratch with high-performance computing, including hybrid parallelization. By using it, the components of the pure rotational energy have been calculated for the self-consistent axial-MF states of even-even nuclei by using the semi-realistic nucleonic interaction interaction M3Y-P6. Although the moment of inertia is calculated by using the Inglis [4] formula or the Belyaev formula [5], they can not separate

the rotational energy into the constituent terms of the Hamiltonian that contains the nucleonic interactions.

We explain the advantage of the M3Y-type interactions. Since the constituent terms of the effective Hamiltonian are separated in order to investigate the rotational energy, it is desired to use the effective interaction which respects the bare nucleonic interaction as possible. The M3Y-type interactions [26–28] have been developed based on the M3Y-Paris interaction [23–25]. The M3Y-type interactions are composed of three-range Yukawa functions except for the density-dependent interaction. The longest range force in the M3Y-type interactions is the OPEP. The parameters of the M3Y-P6 are based on the M3Y-Paris interaction [24] with minimal modifications [26–28]. The parameters of the M3Y-Paris interaction are fitted with the G-matrix derived from by the Paris potential [25]. Especially, the parameters of the tensor force are fitted with the G-matrix. The G-matrix enables to deal with the repulsive core in the bare nucleonic interaction. The instability of the isotropic spin-saturated symmetric nuclear matter has been improved by using the M3Y-P6 interaction [27]. The MF calculations using the M3Y-P6 have described well the magic number of nuclei over a wide range of the nuclear chart [30]. Because it has a certain connection to the bare nucleonic interaction and is applicable to self-consistent MF calculations including deformation [31, 32], the M3Y-type interaction is suitable for analyzing the rotational energy of nuclei. Details of the M3Y-P6 interaction will be given in Sec. 2.6.

The GEM enables to treat many nuclei over a wide range of the nuclear chart efficiently, including unstable nuclei which have exotic structures such as the halo structure. Since the interaction is a finite-range interaction, the numerical cost of the MF and the AMP calculations is high. The matrix elements of the finite-range interactions are calculated and stocked once by using the GEM. Then, the GEM enables to reuse matrix elements repeatedly. The spherical bases are adopted, which have an advantage of numerical accuracy in the AMP calculation compared with the mesh method for the coordinate space. Details of the GEM will be given in Sec. 6.1.

Since the nucleonic interaction is a short range force, the components of the interactions for the rotational energy could be associated with spatial correlations between nucleons via the expectation value of the two-body delta function. Details of the spatial correlations between nucleons will be given in Sec. 5.

Additionally, we have generalized the previous theory of the AMP with rotation by using the cumulant expansion. Compared with the previous formulas [3, 7, 8, 10, 11, 13], we find additional terms which could be important for light or weakly-deformed nuclei.

1.5 Published and unpublished parts in this paper

Since this paper includes both published and unpublished parts, we mention them here.

This paper is written based on Ref. [39]. As published parts in this paper, numerical results of the AMP by using the M3Y-P6 interaction with the GEM for the deformed HF states are shown in Secs. 7.1, 7.2, and 7.3. The revised theory of the AMP and the rotation with the cumulant expansion is presented in Secs. 4.2 and 4.4, and the Gaussian approximation in Appendix F. As a minor point, the AMP for the nonorthogonal bases are presented in Sec. 6.4, and the non-negativity of the overlap function for the HF states is proven in Appendix H.

The unpublished parts in this paper are numerical results containing the pair correlations in Secs. 7.4, 7.5, and 7.6. The nucleonic correlations, especially the spatial correlations between nucleons, are introduced in Chap. 5, which is connected with numerical results in Sec. 7.5.

Chapter 2

Effective Hamiltonian of nuclei

In this chapter, the effective Hamiltonian of nuclei is discussed. This chapter will help the readers to understand the nucleonic interaction.

2.1 Introduction to effective Hamiltonian of nuclei

In this section, the effective Hamiltonian of nuclei is discussed. One of the serious problems in nuclear physics is that the nucleonic interaction has not been established completely. Although the nucleonic interaction originates from the QCD [20] in principle, it is still challenging to derive it from the QCD, which is applicable to a variety of nuclear structures with good accuracy. In spite of the progress in the lattice QCD calculations [40–42], there is still a gap between the accuracy for the lattice QCD calculations [43] and the accuracy required for the nuclear structure study. The chiral effective field theory (χEFT) [44–46] has advanced as *ab initio* calculations for the study of the nuclear structure. However, the χEFT has not yet been able to be described for the deformation of nuclei in the MF theory.

As a bare nucleonic interaction, some models fitted so as to reproduce experimental data of the two-nucleon scattering via the T-matrix have been developed, *e.g.*, the Hamada-Johnston potential [47–49], the Reid potential [50], the Paris potential [23, 24], and the Bonn potential [51–53]. The bare nucleonic interaction overall is short-range, attractive, and stronger than the Coulomb force. The nucleonic interaction includes a finite-range interaction. The longest-range interaction between two nucleons is dominated by the attractive OPEP. In contrast, the medium- or the short-range interactions are influenced by the two-pion exchange, the heavy meson, or the degree-of-freedom of quarks. The bare nucleonic interaction overall has a strong repulsive core in the short distance between two nucleons, which is connected with the sign of the phase shift obtained by the proton-proton scattering experiments. The strong repulsive core prevents the MF calculation with complicated quantum many-body correlations in nuclei. Since the nucleonic interaction also depends on the spin, it could include the central and the noncentral ones. The nucleonic interaction has the isospin symmetry approximately.

The Brückner's G-matrix [54–56] enables to avoid the strong repulsion, then respect the bare nucleonic interaction. The G-matrix depends on the energy of two scattering particles and the density of nuclei. The effective interaction based on the G-matrix has

often been used for nuclear scattering calculations. The effective interaction based on the bare nucleonic interaction which is applicable to the nuclear structure calculations has been developed [57], *e.g.*, the Bonn potential [53] or the Paris potential [28].

For the nuclear structure calculations, the Skyrme interaction [36, 37, 58–63] is one of the popular nucleonic interactions. It enables to implement the numerical calculations without the truncation of the model space. The radial function of the Skyrme interaction is the two-body delta interaction. The derivative terms are included there, which consider the finite-range interaction. The saturation property of the binding energy for the density should be satisfied. In order to avoid compression of bound states, the density-dependent interactions are phenomenologically introduced, which is often related to the density-functional theory (DFT) [64–66]. Since the Fourier transform of the delta function is constant, the high-momentum components $|\mathbf{p}| \to \infty$ make an attractive force strong with the pair correlations, then the high compression of nuclei occurs. Therefore, it is necessary to introduce a cut-off parameter for high momentum or repulsive forces.

As a finite-range interaction, one of the popular nucleonic interactions is the Gogny interaction [38]. The radial function of the Gogny interaction is the Gauss function which explicitly includes the finite-range interaction. Since there is no density-dependent interaction in the SE channel of the Gogny interaction, the instability of the nuclear matter arises.

In this study, the M3Y-type interaction M3Y-P6 has been used, as will be explained in Sec. 2.6, which has some advantages compared with the Skyrme or the Gogny interactions.

2.2 Binding energy

In this section, the binding energy of nuclei is summarized.

The speed of light in the vacuum is denoted as c, and the reduced Planck constant $\hbar$. The Coulomb potential $V(r)$ between two electrons is $V(r) = k_c e^2/r$, where k_c is a constant value, and e is the elementary charge. In the following, the CGS Gauss unit is applied, $k_c = 1$ with $\hbar = c = 1$.

A nucleus is composed of nucleons (protons and neutrons). The number of protons is Z, and that of neutrons is N. The mass number of nuclei is $A = Z + N$.

The binding energy $B(Z, N)$ of nuclei is the energy separating a nucleus into nucleons, which is defined as

$$B(Z, N) := ZM_p + NM_n - M(Z, N), \tag{2.1}$$

where M_p (M_n) is the mass of the proton (neutron), and $M(Z, N)$ is the mass of the nucleus. In the following, $M_p \approx M_n$ is assumed. By the definition in Eq. (2.1), $B(Z, N)$ is positive. The binding energy of nuclei could be observed experimentally via the mass of nucleons and nuclei.

The Bethe-Weizsäcker formula [3] is well known as the semi-empirical mass formula,

$$\begin{aligned} &B(Z, N) \approx b_{\mathrm{V}} A - b_{\mathrm{S}} A^{2/3} - b_{\mathrm{A}} \frac{(N-Z)^2}{A} - b_{\mathrm{C}} \frac{Z^2}{A^{1/3}} + (\text{pairing energy}), \\ &b_{\mathrm{V}} \approx 16\,\mathrm{MeV}, \quad b_{\mathrm{S}} \approx 17\,\mathrm{MeV}, \quad b_{\mathrm{A}} \approx 25\,\mathrm{MeV}, \quad b_{\mathrm{C}} \approx 0.7\,\mathrm{MeV}, \end{aligned} \tag{2.2}$$

where the binding energy is represented by the function of Z and N with a few parameters. Equation (2.2) is composed of the volume energy, the surface energy, the symmetry energy, the Coulomb energy, and the pair energy. Empirically, the binding energy per nucleon has almost a constant value, $B(Z,N)/A \approx 8\,\mathrm{MeV}$, except some light nuclei. Equation (2.2) will be one of the clues for understanding the effective Hamiltonian of nuclei.

2.3 Effective Hamiltonian and G-matrix

In this section, the effective Hamiltonian and the G-matrix are summarized [3]. We consider that the Hilbert space of quantum many-body systems $\mathcal{H}$ forms the direct sum of the subspaces $\mathcal{H}_\mathcal{P}$ and $\mathcal{H}_\mathcal{Q}$ as $\mathcal{H} = \mathcal{H}_\mathcal{P} \oplus \mathcal{H}_\mathcal{Q}$. For example, $\mathcal{H}_\mathcal{P}$ is the subspace spanned by states which belongs to low energies, and $\mathcal{H}_\mathcal{Q}$ is the other one. The operator $\hat{\mathcal{P}}$ is defined as the projection operator on the subspace $\mathcal{H}_\mathcal{P}$. The Schrödinger equation is replaced by the projection operator $\hat{\mathcal{P}}$ as follows:

$$\hat{H}\,|\Psi\rangle = E\,|\Psi\rangle \quad \rightarrow \quad \hat{H}_{\text{eff}}\,|\Phi\rangle = E\,|\Phi\rangle\,, \tag{2.3}$$

where we have defined the effective Hamiltonian as $\hat{H}_{\text{eff}} := \hat{\mathcal{P}}\hat{H}\hat{\mathcal{P}}^\dagger$ and the state $|\Phi\rangle$ as $|\Phi\rangle := \hat{\mathcal{P}}\,|\Psi\rangle$. In Eq. (2.3), the energy E is the same value, while the Hamiltonian and the state differ from the original ones. The effects from the subspace $\mathcal{H}_\mathcal{Q}$ could be renormalized into the effective Hamiltonian $\hat{H}_{\text{eff}}$.

The T-matrix describes the scattering of two free particles, whose operator is derived from the Lippmann-Schwinger equation [67],

$$\hat{T} = \hat{V} + \hat{V}\frac{1}{E-\hat{K}}\hat{T}, \tag{2.4}$$

where E is the scattering energy of the particles, $\hat{K} = \sum_i \mathbf{p}_i^2/2M$ is the kinetic energy of the free particles, and $\hat{V}$ is an interaction between the particles.

In analogy with the T-matrix, the two-body scattering in the medium (*e.g.*, nuclei) is described by the Brückner's G-matrix [54–56] whose operator $\hat{G}$ satisfies

$$\hat{G} = \hat{V} + \hat{V}\frac{\hat{Q}}{E-\hat{h}}\hat{G}, \tag{2.5}$$

where the scattering energy of the particles is denoted as E. The Pauli exclusion operator $\hat{Q}$ and the HF Hamiltonian $\hat{h}$ is defined as

$$\hat{Q} := \sum_{\substack{i<i',\\ \varepsilon_\mathrm{F}<\varepsilon_i,\varepsilon_{i'}}} |i\,i'\rangle\langle i\,i'|\,, \tag{2.6a}$$

$$\hat{h} := \sum_i \varepsilon_i\, a_i^\dagger a_i, \tag{2.6b}$$

with the Fermi energy ε_F and the single particle (s.p.) energies ε_i. The indices i, i' represent the s.p. states obtained by the HF solutions. The HF theory will be briefly

explained as a special case of the HFB theory in Sec. 6.2. Equation (2.5) is called the Bethe-Goldstone equation [68–70]. Equation (2.5) can be written as

$$\hat{G} = \frac{1}{1 - \hat{V}\frac{\hat{Q}}{E-\hat{h}}}\hat{V}, \tag{2.7}$$

thus the matrix elements of $\hat{G}$ converge even if those of $\hat{V}$ diverge. We define the one-body potential for the intermediate states as

$$\hat{U}' := \sum_{k_1,k_2} \sum_{\substack{i, \\ \varepsilon_i < \varepsilon_{\rm F}}} \langle k_1\, i|\hat{V}|k_2\, i\rangle\, a^\dagger_{k_1} a_{k_2} - \langle {\rm HF}|\hat{V}|{\rm HF}\rangle\,, \tag{2.8}$$

which could be regarded as a potential in the medium. The propagator $\hat{Q}/(E-\hat{h})$ in Eq. (2.5) considers the following infinite repetition of interactions between two particles in the medium by a propagator $\hat{Q}/(E_{\rm kin} - \hat{K})$,

$$\begin{aligned}\frac{\hat{Q}}{E-\hat{h}} &= \frac{\hat{Q}}{E_{\rm kin} - \hat{K} - \hat{U}'} \\ &= \frac{\hat{Q}}{E_{\rm kin} - \hat{K}} + \frac{\hat{Q}}{E_{\rm kin} - \hat{K}}\,\hat{U}'\,\frac{\hat{Q}}{E_{\rm kin} - \hat{K}} \\ &\quad + \frac{\hat{Q}}{E_{\rm kin} - \hat{K}}\,\hat{U}'\,\frac{\hat{Q}}{E_{\rm kin} - \hat{K}}\,\hat{U}'\,\frac{\hat{Q}}{E_{\rm kin} - \hat{K}} + \cdots\,,\end{aligned} \tag{2.9}$$

where $E_{\rm kin} := E - \langle {\rm HF}|\hat{V}|{\rm HF}\rangle$. By using the Goldstone diagram, the G-matrix is graphically represented as a summation of ladder diagrams [3,53], which is a part of the connected diagrams in the perturbation theory. Thus, high-momentum components are renormalized into parameters in the G-matrix. From Eq. (2.5), the G-matrix depends on the energy E and the density via $\hat{Q}$.

In this study, the effective interactions fitted with the G-matrix has been used, explicitly consider the density dependence and ignore the energy dependence, as will be presented in Sec. 2.6.

2.4 Symmetry of effective Hamiltonian of nuclei

In this section, the symmetry of the effective Hamiltonian of nuclei is summarized [3]. In the following, the nucleonic interaction between two nucleons is considered in the non-relativity. The weak interaction and the gravity are ignored. The s.p. wave function of the nucleons is characterized in the coordinate space, the spin space, and the isospin space $\varphi_i(\mathbf{r}\sigma\tau) := \langle \mathbf{r}\sigma\tau|i\rangle$, where i is the index of states.

The s.p. wave function of the two nucleons in the coordinate space is rewritten by using the center-of-mass and the relative coordinates, where the angular function in the latter coordinates can be represented by the spherical harmonics $Y^{(L)}_{L_z}(\theta_{ij}, \phi_{ij})$. The exchange operator of two coordinates is defined as $P_{\mathbf{r}}$ which satisfies

$$\hat{P}_{\mathbf{r}}\,|LL_z\rangle_{ij} = (-)^L\,|LL_z\rangle_{ij}\,, \tag{2.10}$$

where the even (odd) value of L corresponds with the even (odd) parity.

For the spin states, we define $|\pm\rangle_i := |s_i = \frac{1}{2}\ s_{z,i} = \pm\frac{1}{2}\rangle$ and $|\pm\mp\rangle_{ij} := |\pm\rangle_i \otimes |\mp\rangle_j$ for simplicity. The state of the two nucleons, where the two spins $\frac{1}{2}$ are coupled as $|S\,S_z\rangle_{ij}$, is represented as

$$\begin{aligned} |1\,1\rangle_{ij} &= |{+}{+}\rangle_{ij}\,, \\ |1\,0\rangle_{ij} &= \frac{1}{\sqrt{2}}\Big(|{+}{-}\rangle_{ij} + |{-}{+}\rangle_{ij}\Big)\,, \\ |1\,{-1}\rangle_{ij} &= |{-}{-}\rangle_{ij}\,, \\ |0\,0\rangle_{ij} &= \frac{1}{\sqrt{2}}\Big(|{+}{-}\rangle_{ij} - |{-}{+}\rangle_{ij}\Big)\,. \end{aligned} \tag{2.11}$$

The spin-exchange operator between two nucleons is defined as

$$P_\sigma := \frac{1 + \boldsymbol{\sigma}_i \cdot \boldsymbol{\sigma}_j}{2}, \tag{2.12}$$

where $\boldsymbol{\sigma}$ is the Pauli matrix,

$$\sigma_x = \begin{pmatrix} 0 & 1 \\ 1 & 0 \end{pmatrix}, \quad \sigma_y = \begin{pmatrix} 0 & -i \\ i & 0 \end{pmatrix}, \quad \sigma_z = \begin{pmatrix} 1 & 0 \\ 0 & -1 \end{pmatrix}. \tag{2.13}$$

We have

$$\hat{P}_\sigma\,|S\,S_z\rangle_{ij} = (-)^{S+1}\,|S\,S_z\rangle_{ij}\,. \tag{2.14}$$

We represent protons (neutrons) as p (n). The isospin is similarly represented by the spin $\frac{1}{2}$: $p = \frac{1}{2}$ and $n = -\frac{1}{2}$. For the isospin states, we define $|p\rangle_i := |t_i = \frac{1}{2}\ t_{z,i} = \frac{1}{2}\rangle$ and $|n\rangle_i := |t_i = \frac{1}{2}\ t_{z,i} = -\frac{1}{2}\rangle$, for simplicity. The state of the two nucleons, where the two isospins $\frac{1}{2}$ are added as $|T\,T_z\rangle_{ij}$, is represented

$$\begin{aligned} |11\rangle_{ij} &= |pp\rangle_{ij}\,, \\ |10\rangle_{ij} &= \frac{1}{\sqrt{2}}\Big(|pn\rangle_{ij} + |np\rangle_{ij}\Big)\,, \\ |1\,{-1}\rangle_{ij} &= |nn\rangle_{ij}\,, \\ |00\rangle_{ij} &= \frac{1}{\sqrt{2}}\Big(|pn\rangle_{ij} - |np\rangle_{ij}\Big)\,. \end{aligned} \tag{2.15}$$

The isospin-exchange operator between two nucleons is defined as

$$P_\tau := \frac{1 + \boldsymbol{\tau}_i \cdot \boldsymbol{\tau}_j}{2}, \tag{2.16}$$

where $\boldsymbol{\tau}$ is the Pauli matrix,

$$\tau_x = \begin{pmatrix} 0 & 1 \\ 1 & 0 \end{pmatrix}, \quad \tau_y = \begin{pmatrix} 0 & -i \\ i & 0 \end{pmatrix}, \quad \tau_z = \begin{pmatrix} 1 & 0 \\ 0 & -1 \end{pmatrix}. \tag{2.17}$$

We have

$$\hat{P}_\tau\,|T\,T_z\rangle_{ij} = (-)^{T+1}\,|T\,T_z\rangle_{ij}\,. \tag{2.18}$$

Since nucleons are fermion which has the antisymmetry for the exchange of two particles, we get $\hat{P}_{\mathbf{r}}\hat{P}_\sigma\hat{P}_\tau = -1$. Then, channels in two nucleons are restricted to the following four channels; singlet-even (SE), triplet-even (TE), singlet-odd (SO), and triplet-odd (TO) channels. The projection operators on the SE, TE, SO, and TO channels are defined as,

$$\begin{aligned} P_{\mathrm{SE}} &:= \frac{1-P_\sigma}{2}\frac{1+P_\tau}{2}, \quad P_{\mathrm{TE}} := \frac{1+P_\sigma}{2}\frac{1-P_\tau}{2}, \\ P_{\mathrm{SO}} &:= \frac{1-P_\sigma}{2}\frac{1-P_\tau}{2}, \quad P_{\mathrm{TO}} := \frac{1+P_\sigma}{2}\frac{1+P_\tau}{2}. \end{aligned} \tag{2.19}$$

The values of parity $(-)^L$, spin S, and isospin T of two nucleons are shown in Table 2.1.

Table 2.1: The values of parity, spin, and isospin of two nucleons.

Channel	$(-)^L$	S	T
SE	0	0	1
TE	0	1	0
SO	1	0	0
TO	1	1	1

Since nuclei are isolated systems, the nucleonic interactions have translational invariance, rotational invariance, Galilean invariance, parity invariance, time-reversal invariance, and number conservation for both protons and neutrons. The nucleonic interactions also have rotational invariance in the isospin space except for the Coulomb force. The Hamiltonian of nuclei is composed of the following terms:

$$H = K + V_{\mathrm{nucl}} + V_{\mathrm{Coulomb}} - H_{\mathrm{c.m.}}. \tag{2.20}$$

The kinetic energy is $K = \sum_i \mathbf{p}_i^2/(2M)$, the nucleonic interaction between two nucleons is $V_{\mathrm{nucl}} = \sum_{i<j} v_{ij}$, the Coulomb interaction between protons is denoted as V_{Coulomb}, and the center-of-mass term is $H_{\mathrm{c.m.}} = \mathbf{P}^2/(2AM)$, with the total momentum $\mathbf{P} = \sum_i \mathbf{p}_i$, where we assumed that the mass of proton and neutron are same values M. Since $K - H_{\mathrm{c.m.}}$ in Eq. (2.20) does not depend on the total momentum $\mathbf{P}$ and depends on only the relative momentum defined as $\mathbf{p}_{ij} := (\mathbf{p}_i - \mathbf{p}_j)/2$, we get $[\hat{K} - \hat{H}_{\mathrm{c.m.}}, \hat{\mathbf{R}}] = \mathbf{0}$, where $\mathbf{R} := (1/A)\sum_i \mathbf{r}_i$. The following equations are satisfied for the Hamiltonian in Eq. (2.20):

$$[\hat{H}, \hat{\mathbf{P}}] = \mathbf{0}, \tag{2.21a}$$
$$[\hat{H}, \hat{\boldsymbol{J}}] = \mathbf{0}, \tag{2.21b}$$
$$[\hat{H}, \hat{\mathbf{B}}] = \mathbf{0}, \tag{2.21c}$$
$$[\hat{H}, \hat{\mathcal{P}}] = 0, \tag{2.21d}$$
$$[\hat{H}, \hat{\mathcal{T}}] = 0, \tag{2.21e}$$
$$[\hat{H}, \hat{N}_\tau] = 0, \qquad \tau = p, n, \tag{2.21f}$$

with the total momentum $\mathbf{P}$, the total angular momentum operator $\hat{\boldsymbol{J}}$, the boost operator of the Galilean transformation $\hat{\mathbf{B}}$ defined as $\hat{\mathbf{B}} := \hat{\mathbf{P}}t - AM\hat{\mathbf{R}}$, the parity operator $\hat{\mathcal{P}}$, the time-reversal operator $\hat{\mathcal{T}}$, and the number operator for protons (neutrons) $\hat{N}_p$ ($\hat{N}_n$). From Eq. (2.21a), the Hamiltonian does not depend on the center-of-mass $\mathbf{R}$ and depends on only the relative coordinate. From Eq. (2.21b), the Hamiltonian is composed of only the rotational-scalar terms. From Eq. (2.21c), the Hamiltonian depends on only the relative momentum $\mathbf{p}_{ij}$. The Galilean transformation operator $\hat{\mathcal{G}}(\mathbf{V})$ is represented as

$$\hat{\mathcal{G}}(\mathbf{V}) := \exp\Big\{-i\hat{\mathbf{B}}\cdot\mathbf{V}\Big\}, \tag{2.22}$$

where $\mathbf{V}$ is the velocity parameter. If $V_{\rm nucl}$ has density dependence, some of Eqs. (2.21a), (2.21b), (2.21c), and (2.21d) are not satisfied exactly.

We will present constituent terms of the nucleonic interaction $V_{\rm nucl}$ used for studying the rotational energy of nuclei in Sec. 2.6.

2.5 OPEP and tensor force

In this section, we introduce the well-known model of the one-pion-exchange-potential (OPEP). H. Yukawa has predicted that nucleonic interactions are effectively mediated by mesons, and they are represented by the Yukawa functions [21]. The longest range force in the nucleonic interactions is described by the OPEP, which is accompanied by the chiral symmetry breaking in QCD [71, 72]. The nucleonic interactions in the close distance between nucleons have not yet been clear.

The π-mesons (often called *pions*) are bosons, whose three charged states are π^+, π^-, and π^0. The π^- particle is the antiparticle of π^+, whereas an antiparticle of π^0 is itself. The mass of the pions, which is represented as m_π, is lightest in the meson. By using $m_\pi c^2 \approx 140$ MeV, their Compton wavelengths are approximated as $\hbar/m_\pi c \approx 1.4$ fm. Thus, the OPEP explains the nucleonic interactions in the region of $r \gtrsim 1.4\,$fm. The spinor field of nucleons is represented as $\psi(x) := \psi^{s\tau}(\mathbf{r}, t)$, where the indices s and τ are the four-component spinor and the isospin, respectively. The relativistic Lagrangian density of the pseudo-vector coupling model [1] between the pions $\Pi^a(x)$, $(a = 1, 2, 3)$ and the nucleons $\psi(x)$, which satisfies the Lorentz invariance and the isoscalar, is presented as follows: [2]

$$\mathcal{L}(x) = \mathcal{L}_{\rm nucl}(x) + \mathcal{L}_\pi(x) + \mathcal{L}_{\rm int\_R}(x), \tag{2.24a}$$

$$\mathcal{L}_\pi(x) = \frac{1}{2}(\partial_\mu \Pi^a(x))(\partial^\mu \Pi^a(x)) - \frac{1}{2}(m_\pi)^2\, \Pi^a(x)\, \Pi^a(x), \tag{2.24b}$$

$$\mathcal{L}_{\rm int\_R}(x) = -g_\pi\, \bar{\psi}(x)\, \gamma_5\, \gamma_\mu\, \tau^a\, \psi(x)\, \partial^\mu\, \Pi^a(x), \tag{2.24c}$$

where g_π is a parameter of strength, γ_μ is the gamma matrices, $\bar{\psi}(x) := \psi^\dagger(x)\gamma^0$, $\gamma^5 := i\gamma^1\gamma^2\gamma^3\gamma^4 = \gamma_5 = \begin{pmatrix} 0 & 1 \\ 1 & 0 \end{pmatrix}$. Although this model in Eq. (2.24) is not renormalizable

[1] The original Lagrangian density of the OPEP is the pseudo-scalar coupling interactions as

$$\mathcal{L}_{\rm int\_R}(x) = -g_\pi^{\rm (PS)}\, \bar{\psi}(x)\, \gamma_5\, \tau^a\, \psi(x)\, \Pi^a(x), \tag{2.23}$$

which is renormalizable.

[2] The spin and isospin indices are summed implicitly.

due to ∂^μ in Eq. (2.24c), it enables to derive both the Yukawa function and the tensor force naturally, as will be shown in the following. By using the non-relativistic limit, the Lagrangian densities in Eqs. (2.24b) and (2.24c) are approximated as

$$\mathcal{L}_\pi(x) \approx \mathcal{L}_\pi(\mathbf{r}) = -\frac{1}{2}(\nabla \Pi^a(\mathbf{r})) \cdot (\nabla \Pi^a(\mathbf{r})) - \frac{1}{2}(m_\pi)^2 \Pi^a(\mathbf{r}) \Pi^a(\mathbf{r}), \tag{2.25a}$$

$$\mathcal{L}_{\text{int\_R}}(x) \approx \mathcal{L}_{\text{int\_NR}}(\mathbf{r}) = g_\pi \, \psi^\dagger(\mathbf{r}) \, \sigma_i \, \tau^a \, \psi(\mathbf{r}) \, \partial_i \, \Pi^a(\mathbf{r}), \tag{2.25b}$$

with the static fields $\Pi^a(\mathbf{r})$ and $\psi(\mathbf{r}\sigma\tau)$, where the number of the spin index of $\psi(\mathbf{r}\sigma\tau)$ is reduced by two components. By using the Euler Lagrange equation for $\Pi^a(\mathbf{r})$ in Eq. (2.25), we get

$$\left[\boldsymbol{\nabla}^2 - (m_\pi)^2\right] \Pi^a(\mathbf{r}) = g_\pi \, \partial_i \left[\psi^\dagger(\mathbf{r}) \, \sigma_i \, \tau^a \, \psi(\mathbf{r})\right], \tag{2.26}$$

then

$$\Pi^a(\mathbf{r}) = -\frac{g_\pi}{4\pi} \int d^3r' \left\{\partial_i \left[\psi^\dagger(\mathbf{r}') \, \sigma_i \, \tau^a \, \psi(\mathbf{r}')\right]\right\} \frac{e^{-m_\pi r_{ij}}}{r_{ij}}, \tag{2.27}$$

where $\mathbf{r}_{ij} := \mathbf{r}_i - \mathbf{r}_j$ and $r_{ij} := |\mathbf{r}_{ij}|$. By using Eqs. (2.25b) and (2.27), the Hamiltonian of the effective interaction between nucleons is obtained as

$$\begin{aligned} H_{\text{int\_NR}} :=& - \int d^3r \, \mathcal{L}_{\text{int\_NR}}(\mathbf{r}) \\ =& - \frac{(g_\pi)^2}{4\pi} \int d^3r \int d^3r' \left[\psi^\dagger(\mathbf{r}) \, \sigma_i \, \tau^a \, \psi(\mathbf{r})\right] \left[\psi^\dagger(\mathbf{r}') \, \sigma_j \, \tau^a \, \psi(\mathbf{r}')\right] \partial_i \, \partial_j{}' \, \frac{e^{-m_\pi r_{ij}}}{r_{ij}}. \end{aligned} \tag{2.28}$$

Therefore, the effective interaction between two nucleons v_{ij} is derived:

$$\begin{aligned} v_{ij} =& - \frac{(g_\pi)^2}{4\pi} \, (\boldsymbol{\tau}_i \cdot \boldsymbol{\tau}_j)(\boldsymbol{\sigma}_i \cdot \boldsymbol{\nabla}_i)(\boldsymbol{\sigma}_j \cdot \boldsymbol{\nabla}_j) \, \frac{e^{-m_\pi r_{ij}}}{r_{ij}} \\ =& \frac{(g_\pi)^2}{4\pi} \, (\boldsymbol{\tau}_i \cdot \boldsymbol{\tau}_j) \left\{ \frac{1}{3} \, (m_\pi)^3 \, \frac{e^{-m_\pi r_{ij}}}{m_\pi r_{ij}} \left[(\boldsymbol{\sigma}_i \cdot \boldsymbol{\sigma}_j) + \left(1 + \frac{3}{m_\pi r_{ij}} + \frac{3}{(m_\pi r_{ij})^2}\right) S_{ij} \right] \right. \\ & \left. - \, \frac{4\pi}{3} \, (\boldsymbol{\sigma}_i \cdot \boldsymbol{\sigma}_j) \, \delta(\mathbf{r}_{ij}) \right\}, \end{aligned} \tag{2.29}$$

where the tensor force is defined as

$$\begin{aligned} S_{ij} :=& \, 3 \, (\boldsymbol{\sigma}_i \cdot \hat{\mathbf{r}}_{ij})(\boldsymbol{\sigma}_j \cdot \hat{\mathbf{r}}_{ij}) - \boldsymbol{\sigma}_i \cdot \boldsymbol{\sigma}_j \\ =& \, 3 \left[\hat{r}_{ij}^{(1)} \otimes \hat{r}_{ij}^{(1)}\right]^{(2)} \cdot \left[\sigma_i^{(1)} \otimes \sigma_j^{(1)}\right]^{(2)} \\ =& \sqrt{\frac{24\pi}{5}} \, Y^{(2)}(\hat{\mathbf{r}}_{ij}) \cdot \left[\sigma_i^{(1)} \otimes \sigma_j^{(1)}\right]^{(2)}, \end{aligned} \tag{2.30}$$

with $\hat{\mathbf{r}}_{ij} := \mathbf{r}_{ij}/r_{ij}$. We have defined the scalar product $\cdot$ between the spherical tensors

$U^{(\lambda)}$ and $V^{(\lambda)}$,

$$\begin{aligned} U^{(\lambda)} \cdot V^{(\lambda)} &:= (-)^{\lambda}\sqrt{2\lambda+1}\left[U^{(\lambda)} \otimes V^{(\lambda)}\right]_0^{(0)} \\ &= \sum_{\mu=-\lambda}^{\lambda} (-)^{\mu} U_{\mu}^{(\lambda)} V_{-\mu}^{(\lambda)}, \\ \left[U^{(\lambda_1)} \otimes V^{(\lambda_2)}\right]_{\mu}^{(\lambda)} &:= \sum_{\mu_1=-\lambda_1}^{\lambda_1} \sum_{\mu_2=-\lambda_2}^{\lambda_2} \langle \lambda_1\lambda_2\mu_1\mu_2 | (\lambda_1\lambda_2)\lambda\mu \rangle \, U_{\mu_1}^{(\lambda_1)} V_{\mu_2}^{(\lambda_2)}, \end{aligned} \tag{2.31}$$

where $\langle \lambda_1\lambda_2\mu_1\mu_2 | (\lambda_1\lambda_2)\lambda\mu \rangle$ are the Clebsch-Gordan coefficients [1, 73]. The OPEP in Eq. (2.29) has now been derived. The radial function of the OPEP is the Yukawa function $e^{-m_\pi r_{ij}}/(m_\pi r_{ij})$ except the delta function $\delta(\mathbf{r}_{ij})$. The tensor force S_{ij} is naturally included in Eq. (2.29). [3]

In this study, the effective interaction including the OPEP and the tensor force has been used, as will be shown in Sec. 2.6.

2.6 Semi-realistic effective Hamiltonian M3Y-P6

In this section, the semi-realistic effective Hamiltonian M3Y-P6 is discussed in detail. First, the M3Y-type interaction is given, then the history of the M3Y-type interactions is introduced with the parameter set M3Y-P6.

We have used the effective Hamiltonian of nuclei in Eq. (2.20), which satisfies the symmetry in Eq. (2.21). We assume that the individual terms of the Hamiltonian also have isospin symmetries except for the Coulomb force. The effective nucleonic interaction is formed by the following terms:

$$V_{\rm nucl} = V^{(\rm C)} + V^{(\rm LS)} + V^{(\rm TN)} + V^{(\rm C\rho)}, \tag{2.32a}$$

$$V^{(\rm X)} = \sum_{i<j} v_{ij}^{(\rm X)}, \quad ({\rm X} = {\rm C}, {\rm LS}, {\rm TN}, {\rm C}\rho), \tag{2.32b}$$

where $V^{(\rm C)}$, $V^{(\rm LS)}$, and $V^{(\rm TN)}$ are the central, the LS, and the tensor forces. The central density-dependent term is distinguished from $V^{(\rm C)}$ and represented by $V^{(\rm C\rho)}$.

[3] The tensor force is necessary to explain the experimental fact that the bound state of the deuteron contains not only the S-state but also the D-state, then its ground state could have the small value of the quadrupole moment.

The individual terms of Eq. (2.32a) have the following forms:

$$
\begin{aligned}
v_{ij}^{(\mathrm{C})} &= \sum_n \left(t_n^{(1)} + t_n^{(\sigma)} (\boldsymbol{\sigma}_i \cdot \boldsymbol{\sigma}_j) + t_n^{(\tau)} (\boldsymbol{\tau}_i \cdot \boldsymbol{\tau}_j) + t_n^{(\sigma\tau)} (\boldsymbol{\sigma}_i \cdot \boldsymbol{\sigma}_j)(\boldsymbol{\tau}_i \cdot \boldsymbol{\tau}_j) \right) f_n^{(\mathrm{C})}(r_{ij}) \\
&= \sum_n \left(t_n^{(\mathrm{W})} + t_n^{(\mathrm{B})} P_\sigma - t_n^{(\mathrm{H})} P_\tau - t_n^{(\mathrm{M})} P_\sigma P_\tau \right) f_n^{(\mathrm{C})}(r_{ij}) \\
&= \sum_n \left(t_n^{(\mathrm{SE})} P_{\mathrm{SE}} + t_n^{(\mathrm{TE})} P_{\mathrm{TE}} + t_n^{(\mathrm{SO})} P_{\mathrm{SO}} + t_n^{(\mathrm{TO})} P_{\mathrm{TO}} \right) f_n^{(\mathrm{C})}(r_{ij}), \\
v_{ij}^{(\mathrm{LS})} &= \sum_n \left(t_n^{(\mathrm{LSE})} P_{\mathrm{TE}} + t_n^{(\mathrm{LSO})} P_{\mathrm{TO}} \right) f_n^{(\mathrm{LS})}(r_{ij}) \, \mathbf{L}_{ij} \cdot (\mathbf{s}_i + \mathbf{s}_j), \\
v_{ij}^{(\mathrm{TN})} &= \sum_n \left(t_n^{(\mathrm{TNE})} P_{\mathrm{TE}} + t_n^{(\mathrm{TNO})} P_{\mathrm{TO}} \right) f_n^{(\mathrm{TN})}(r_{ij}) \, r_{ij}^2 \, S_{ij}, \\
v_{ij}^{(\mathrm{C}\rho)} &= \left(t_\rho^{(\mathrm{SE})} P_{\mathrm{SE}} \cdot [\rho(\mathbf{r}_i)]^{\alpha^{(\mathrm{SE})}} + t_\rho^{(\mathrm{TE})} P_{\mathrm{TE}} \cdot [\rho(\mathbf{r}_i)]^{\alpha^{(\mathrm{TE})}} \right) \delta(\mathbf{r}_{ij}),
\end{aligned}
\tag{2.33}
$$

where $\mathbf{L}_{ij} := \mathbf{r}_{ij} \times \mathbf{p}_{ij}$. The spin- and isospin-exchange operators between two nucleons P_σ and P_τ, and the projection operators on SE, TE, SO, and TO channels are defined in Eq. (2.19). The tensor force S_{ij} is defined in Eq. (2.30). We used the Yukawa function $f_n^{(\cdot)}(r) = e^{-\mu_n^{(\cdot)} r}/(\mu_n^{(\cdot)} r)$ for the radial functions, except for $v_{ij}^{(\mathrm{C}\rho)}$. The longest-range term in $v_{ij}^{(\mathrm{C})}$ is fixed to be that of the OPEP. This central OPEP, which is denoted by $V^{(\mathrm{OPEP})}$, is an example of spin-dependent interactions. The LS interaction $v_{ij}^{(\mathrm{LS})}$ is needed to describe the shell structure, especially to explain the magic number of nuclei. The parameters are $t_n^{(\cdot)}$, $t_\rho^{(\cdot)}$, $\mu_n^{(\cdot)}$, and $\alpha^{(\cdot)}$. The relations between the parameters $t_n^{(\cdot)}$ are represented as

$$
\begin{pmatrix} t_n^{(\mathrm{SE})} \\ t_n^{(\mathrm{TE})} \\ t_n^{(\mathrm{SO})} \\ t_n^{(\mathrm{TO})} \end{pmatrix}
= \begin{pmatrix} 1 & -1 & -1 & 1 \\ 1 & 1 & 1 & 1 \\ 1 & -1 & 1 & -1 \\ 1 & 1 & -1 & -1 \end{pmatrix}
\begin{pmatrix} t_n^{(\mathrm{W})} \\ t_n^{(\mathrm{B})} \\ t_n^{(\mathrm{H})} \\ t_n^{(\mathrm{M})} \end{pmatrix}
= \begin{pmatrix} 1 & -3 & 1 & -3 \\ 1 & 1 & -3 & -3 \\ 1 & -3 & -3 & 9 \\ 1 & 1 & 1 & 1 \end{pmatrix}
\begin{pmatrix} t_n^{(1)} \\ t_n^{(\sigma)} \\ t_n^{(\tau)} \\ t_n^{(\sigma\tau)} \end{pmatrix}.
\tag{2.34}
$$

In the original M3Y-type interaction [22], the three-range Yukawa-type interactions are superposed. Some phenomenological bare nucleonic interactions are used in the T-matrix calculations, then the G-matrix in Eq. (2.5) is calculated. The parameters in the M3Y-type interactions are fitted with the G-matrix. The central force, the LS force, and the tensor force are considered in the M3Y-type interactions, especially the OPEP in the tensor force is treated precisely. As a bare nucleonic interaction, the Paris potential [23] is derived based on a more fundamental meson theory, and the parameters are fitted with the two nucleon scattering by using the T-matrix [24]. The M3Y-Paris interaction [25] is the M3Y-type interaction whose parameters are fitted with the G-matrix derived from the Paris potential. While the long-range part in the central force is the OPEP, the medium-range part in the central force is $(\pi + 2\pi + \omega)$ potential, and the short-range part ($r \lesssim 0.8\,\mathrm{fm}$) is treated phenomenologically by using the Yukawa functions. The radial part of the OPEP in the tensor force is changed to be handled easily. Although Eq. (2.5) depends on the energy, the value of the energy in Eq. (2.5) is fixed on 40 MeV, and the energy dependence is ignored in Eq. (2.33). [4]

[4] It is not easy to treat the energy dependence of the G-matrix in Eq. (2.5) explicitly.

At the nuclear-theory group in Chiba university, the M3Y-type interactions have been developed both the parameters and the interactions with minimal modifications to respect for the M3Y-Paris interaction, led by Prof. H. Nakada [28]. The density-dependent term $v_{ij}^{(\mathrm{C}\rho)}$ in Eq. (2.33) is introduced phenomenologically to satisfy the saturation property of the binding energy [3, 26–28], which is considered the density dependence in Eq. (2.5). Although the function of the effective interaction $\hat{V}_{\mathrm{nucl}}$ is different from that of the G-matrix derived from the Paris potential, the matrix elements of $\hat{V}_{\mathrm{nucl}}$ is fitted with those of $\hat{G}$ in Eq. (2.5). Thus, there is a model limitation in the M3Y-type interactions in Eqs. (2.32) and (2.33). On the other hand, the M3Y-type interactions have a certain connection with the bare nucleonic interaction and is applicable to the MF calculation [28]. The M3Y-type interaction is applicable to a wide range of energy compared with fully-phenomenological interactions used in the structure calculations, such as the Skyrme or the Gogny interactions. Especially, the MF calculations using the M3Y-P6 have described well the magic number of nuclei over a wide range of the nuclear chart [30] and deformation of nuclei [31, 32]. Therefore, considering the above situation, the M3Y-type interactions are called semi-realistic nucleonic interactions [27, 28].

The M3Y-P6 interaction enables to improve the instability of the isotopic spin-saturated symmetric nuclear-matter in $\rho(\mathbf{r}) \gtrsim 0.6\,\mathrm{fm}^{-3}$ by introducing the repulsive force between neutrons in the SE channel [27]. The density-dependent interaction is mathematically generalized as $\alpha^{(\mathrm{SE})} \neq \alpha^{(\mathrm{TE})}$ in Eq. (2.33). The values of the parameters for M3Y-P6 are given in Table 2.2 [27]. There are 31 parameters in the M3Y-P6, 16 of them are unchanged from the M3Y-Paris interaction in order to respect the G-matrix derived from the M3Y-Paris interaction as possible. In concrete, the tensor force and the OPEP of the π-meson in the central force are fixed to the M3Y-Paris interaction. The strengths of the LS interactions are multiplied by 2.2, phenomenologically. The range parameters $\mu_n^{(\cdot)}$ are fixed in all channels, and the parameter $t_2^{(\mathrm{TE})}$ is unchanged.

In this study, the semi-realistic interaction M3Y-P6 has been used for studying the pure rotational energy of nuclei.

Table 2.2: Parameters of M3Y-type interactions. See Eq. (2.33) for the definition.

Parameter	M3Y-Paris	M3Y-P6
$1/\mu_1^{(\mathrm{C})}$ (fm)	0.25	0.25
$t_1^{(\mathrm{SE})}$ (MeV)	11466	10766
$t_1^{(\mathrm{TE})}$ (MeV)	13967	8474
$t_1^{(\mathrm{SO})}$ (MeV)	−1418	−728
$t_1^{(\mathrm{TO})}$ (MeV)	11345	12453
$1/\mu_2^{(\mathrm{C})}$ (fm)	0.40	0.40
$t_2^{(\mathrm{SE})}$ (MeV)	−3556	−3520
$t_2^{(\mathrm{TE})}$ (MeV)	−4594	−4594
$t_2^{(\mathrm{SO})}$ (MeV)	950	1386
$t_2^{(\mathrm{TO})}$ (MeV)	−1900	−1588
$1/\mu_3^{(\mathrm{C})}$ (fm)	1.414	1.414
$t_3^{(\mathrm{SE})}$ (MeV)	−10.463	−10.463
$t_3^{(\mathrm{TE})}$ (MeV)	−10.463	−10.463
$t_3^{(\mathrm{SO})}$ (MeV)	31.389	31.389
$t_3^{(\mathrm{TO})}$ (MeV)	3.488	3.488
$1/\mu_1^{(\mathrm{LS})}$ (fm)	0.25	0.25
$t_1^{(\mathrm{LSE})}$ (MeV)	−5101	−11222.2
$t_1^{(\mathrm{LSO})}$ (MeV)	−1897	−4173.4
$1/\mu_2^{(\mathrm{LS})}$ (fm)	0.40	0.40
$t_2^{(\mathrm{LSE})}$ (MeV)	−337	−741.4
$t_2^{(\mathrm{LSO})}$ (MeV)	−632	−1390.4
$1/\mu_1^{(\mathrm{TN})}$ (fm)	0.40	0.40
$t_1^{(\mathrm{TNE})}$ (MeV·fm^{-2})	−1096	−1096
$t_1^{(\mathrm{TNO})}$ (MeV·fm^{-2})	244	244
$1/\mu_2^{(\mathrm{TN})}$ (fm)	0.70	0.70
$t_2^{(\mathrm{TNE})}$ (MeV·fm^{-2})	−30.9	−30.9
$t_2^{(\mathrm{TNO})}$ (MeV·fm^{-2})	15.6	15.6
$\alpha^{(\mathrm{SE})}$	—	1
$t_\rho^{(\mathrm{SE})}$ (MeV·fm^6)	0	384
$\alpha^{(\mathrm{TE})}$	—	1/3
$t_\rho^{(\mathrm{TE})}$ (MeV·fm^4)	0	1930

Chapter 3

Shell structure and symmetry breaking in MF theory

In this chapter, the shell structure and the symmetry breaking in MF theory of nuclei are introduced. It is necessary to introduce the shell structure for the symmetry breaking in MF theory, such as the deformation and the pair correlations.

3.1 Shell structure

In this section, the shell structure of nuclei is summarized. The magic numbers for stable nuclei are well known from experiments, where the binding energies of nuclei in Eq. (2.1) increase for specific numbers of protons and neutrons respectively,

$$\begin{aligned} Z &= 2, 8, 20, 28, 40, 50, 82, \\ N &= 2, 8, 20, 28, 40, 50, 82, 126. \end{aligned} \tag{3.1}$$

The magic numbers in Eq. (3.1) cannot be explained by the Bethe-Weizsäcker formula in Eq. (2.2) or in the classical mechanics. Based on the magic numbers of nuclei, the independent particle motion is established in the quantum mechanics, where the nuclei have the shell structure with the LS splitting. Since the Hamiltonian of nuclei has rotational symmetry, the ground state of even-even nuclei has spherical symmetry. The spherically-symmetric state is defined as

$$\hat{R}(\Omega) \left|\Phi_{J=M=0}\right\rangle = \left|\Phi_{J=M=0}\right\rangle , \quad \text{for any } \ \Omega, \tag{3.2}$$

where $\hat{R}(\Omega)$ is defined in Eq. (B.1). In the quantum mechanics, since nuclei are finite systems, where the mass number is finite ($1 \leq A \lesssim 300$) [2], it is not easy to occur spontaneous symmetry breaking in nuclei. Therefore, the shell structure is one of basic properties of nuclei and essential for constructing the ground state of nuclei. The MF theory, such as the HF or the HFB theories [3], have been established as basic theories and applied to quantum many-body problems. We discuss the HFB theory in Sec. 6.2.

According to the development of technologies and the progress of experiments, unstable nuclei could have been observed recently. The magic numbers in Eq. (3.1) often disappear or change for unstable nuclei. The shell structure of the intrinsic state with symmetry breaking in the MF theory, such as deformation and pair correlations,

could affect the magic numbers. The symmetry breaking in the MF theory will be introduced in Sec. 3.2.

3.2 Symmetry breaking in MF theory

In this section, the symmetry breaking in MF theory [1] is introduced, in concrete, deformation and pair correlations. The rotational band is the energy spectrum near the ground state of even-even nuclei, where the excitation energies are close to $E_{\rm x}(J^+) \approx J(J+1)/(2\mathcal{I})$, $J^\pi = 0^+, 2^+, 4^+, \cdots$, with the moment of inertia $\mathcal{I}$. It indicates that an intrinsic state of nuclei deforms and rotates collectively with the moment of inertia. The first excitation energy $E_{\rm x}(2^+)$ for the deformed nuclei is much smaller than that for the spherical nuclei, and the ratio $E_{\rm x}(4^+)/E_{\rm x}(2^+)$ is close to 10/3 there. If the moment of inertia $\mathcal{I}$ is a constant value, we obtain the ratios of the excitation energies as follows:

$$\frac{E_{\rm x}(4^+)}{E_{\rm x}(2^+)} = \frac{10}{3}, \quad \frac{E_{\rm x}(6^+)}{E_{\rm x}(2^+)} = 7, \quad \frac{E_{\rm x}(8^+)}{E_{\rm x}(2^+)} = 12, \quad \frac{E_{\rm x}(10^+)}{E_{\rm x}(2^+)} = \frac{55}{3}, \cdots . \tag{3.3}$$

The electromagnetic (EM) transitions are strong within the rotational band compared to those from the outside of the band. The rotational band has been observed experimentally and is well known over a wide range of the nuclear chart, including stable and unstable nuclei.

Since nuclei are isolated systems, the nuclear Hamiltonian has rotational symmetry, and angular momentum is a good quantum number in energy eigenstates. It is well-known that the spin and the parity of the ground state of even-even nuclei is 0^+ without exceptions. However, spontaneous breaking of the rotational symmetry often occurs in the MF approximation, which corresponds with a deformation of the intrinsic state of nuclei. The deformed intrinsic state $|\Phi\rangle$ is defined as

$$^\exists\beta \ \text{ such that } \ e^{-i\hat{J}_y\beta}|\Phi\rangle \not\propto |\Phi\rangle\,, \tag{3.4}$$

i.e., $|\Phi\rangle$ is a superposition of the angular-momentum eigenstates. While the deformed intrinsic state of nuclei is not observed directly, it is reasonable as an interpretation for many-body quantum states. The NG mode is accompanied by symmetry breaking, and it restores the corresponding symmetry in energy eigenstates. The restoration of the rotational symmetry corresponds with a whole rotational motion of the deformed nuclei. The phenomenological theory of the deformation and the rotation of nuclei is summarized in Appendix A, where the rotational energy arises from only the kinetic energy. However, there is no guarantee that the rotation of nuclei is identified with the rotation of the ellipsoid of inertia in the classical mechanics. The nucleonic interaction could contribute to the rotational energy of nuclei.

Many nuclei have the pair correlations with some exceptions. Some experimental facts for pair correlations are well known, e.g., for the Sn isotopes [3]. The even-odd staggering for the mass of nuclei $M_{A+1} > (M_A + M_{A+2})/2$ [A is a even number] is observed experimentally, where the binding energies of even-even nuclei are larger than

[1] The symmetry breaking in MF theory is also called as the quantum phase transition in nuclear physics.

those of odd nuclei. There is an energy gap between the ground state 0^+ and the first excited state 2^+ for even-even nuclei. The pairing rotation $E_{\mathrm{x}'}(n) \approx (n-n_0)^2/(2\mathcal{I}_{\mathrm{pair}})$ for $n = Z, N$ also implies the pair correlations, which is the spectrum of the "excitation energies" for different nuclei which have a different proton or neutron number. It is well known experimentally that the pair correlations between protons and neutrons are very small compared with the neutron-neutron or proton-proton pair correlations.

Since nuclei are isolated systems, the Hamiltonian of nuclei commutes with the proton- and the neutron-number operator, respectively. Thus, the proton and the neutron number are good quantum numbers in energy eigenstates. The pair correlations for the intrinsic state $|\Phi\rangle$ are defined as follows:

$$^{\exists}\phi_\tau \ \text{ such that } \ e^{-i\hat{N}_\tau\phi_\tau}|\Phi\rangle \not\propto |\Phi\rangle \quad \text{for } \tau = p, n. \tag{3.5}$$

In other words, the intrinsic state $|\Phi\rangle$ which has the pair correlations [2] is a superposition of the eigenstates of the proton or the neutron number, though it is not observed directly. The angles ϕ_τ for $\tau = p, n$ are often called global-gauge angles, then the pair correlations are regarded as a spontaneous breaking of the global-gauge symmetry in the MF approximation. The Nambu-Goldstone (NG) mode is accompanied by the symmetry breaking, and it restores the corresponding symmetry in energy eigenstates. The restoration of the global-gauge symmetry corresponds with a pairing rotation of the intrinsic state.

The interpretations of the collective deformation and the pair correlations for nuclei are established based on various experimental facts [1,3] and the MF theory discussed in Sec. 6.2.

[2]The intrinsic state $|\Phi\rangle$ which has the pair correlations is often called the superfluid state or the superconductivity state in the condensed-matter physics.

Chapter 4

Deformation and rotation

In this chapter, deformation and rotation of nuclei are discussed in the quantum mechanics. The phenomenological theory of the deformation and the rotation of nuclei is introduced in Appendix A.

4.1 Variational method with projection

There are two variational methods, the projection after variation (PAV) and the variation after projection (VAP) [3]. In this section, both the PAV and the VAP are explained.

Let us consider a hermitian operator $\hat{A}$ which commutes with the Hamiltonian $\hat{H}$, $[\hat{A}, \hat{H}] = 0$. The eigenvalue a and the eigenstate $|a\rangle$ of the operator $\hat{A}$ satisfies $\hat{A}\,|a\rangle = a\,|a\rangle$. The Hilbert space in our problem is expanded by the eigenstate $|a\rangle$. The projection operator on the state $|a\rangle$ is defined as $\hat{P}_a := |a\rangle\langle a|$ which is hermitian and idempotent,

$$(\hat{P}_a)^\dagger = \hat{P}_a, \tag{4.1a}$$

$$(\hat{P}_a)^2 = \hat{P}_a. \tag{4.1b}$$

By using $\hat{P}_a$, we get $\hat{A} = \sum_a a\hat{P}_a$. Since the completeness is represented as $\sum_a \hat{P}_a = \hat{1}$, an arbitrary state $|\Phi\rangle$ is represented as $|\Phi\rangle = \sum_a \hat{P}_a\,|\Phi\rangle$. For simplicity, $\langle\Phi|\Phi\rangle = 1$. We define the projected energy E_a as

$$E_a := \frac{\langle\Phi|\hat{P}_a^\dagger \hat{H} \hat{P}_a|\Phi\rangle}{\langle\Phi|\hat{P}_a^\dagger \hat{P}_a|\Phi\rangle}. \tag{4.2}$$

By using $[\hat{H}, \hat{P}_a]$ for all a and Eq. (4.1), we get

$$E_a = \frac{\langle\Phi|\hat{H}\hat{P}_a|\Phi\rangle}{\langle\Phi|\hat{P}_a|\Phi\rangle}, \tag{4.3}$$

and

$$\langle\Phi|\hat{H}|\Phi\rangle = \sum_a E_a\,\langle\Phi|\hat{P}_a|\Phi\rangle = \sum_a E_a\,|\,\langle a|\Phi\rangle\,|^2. \tag{4.4}$$

If $E_a > \langle\Phi|\hat{H}|\Phi\rangle$ for all a, it contradicts Eq. (4.4). Therefore, Eq. (4.4) derives the following statement:

$$^{\exists}a \ \text{ such that } \ E_a \leq \langle\Phi|\hat{H}|\Phi\rangle\,. \tag{4.5}$$

Since the observed states in finite quantum many-body systems have a good quantum number whose operator commutes with the Hamiltonian. Therefore, we should minimize not $\langle\Phi|\hat{H}|\Phi\rangle$ but the projected energy E_a. If the energy decreases, the solution gets close to the exact solution of the Hamiltonian by following the variational principle.

There are two ways for the variational method with the projection. In the VAP scheme, the state $|\Phi\rangle$ is calculated by the variation for the projected energy in Eq. (4.2) as

$$\delta E_a = 0. \tag{4.6}$$

On the other hand, in the PAV scheme, the state $|\Phi\rangle$ is once calculated by variation for the following energy,

$$\delta\,\langle\Phi|\hat{H}|\Phi\rangle = 0, \tag{4.7}$$

then, by using the solution $|\Phi\rangle$ in Eq. (4.7), the projected energy E_a is calculated. According to the variational principle, the VAP is a better method than the PAV. Therefore, the PAV is regarded as the approximation of the VAP.

In the MF approximation, spontaneous symmetry breaking often occurs. Then, the symmetry broken solution is projected on states which have good quantum numbers of the operator which commutes with the Hamiltonian in the PAV scheme. On the other hand, the MF results are not respected so much in the VAP scheme. Therefore, the PAV respects the MF results more than the VAP.

It is well known that the numerical calculations of the VAP for actual systems are not easy. Some VAP effects could be considered by using the generator coordinate method (GCM) [3] with the PAV or by using the cranking model [3, 9]. In this study, we have calculated rotational energies of deformed nuclei by the AMP in the framework of the PAV, as will be explained in Sec. 6.4.

4.2 AMP for eigenstate of $\hat{J}_z$

In this section, the theory of the AMP for the eigenstates of $\hat{J}_z$ is discussed. The AMP is the method by which an intrinsic state is projected on angular-momentum eigenstates [3]. The projection operator on the angular-momentum eigenstates is discussed with the Wigner D-function in Appendix B. In the following, we assume that $\hat{\mathcal{S}}$ is a rotational scalar, and the intrinsic state is an eigenstate of $\hat{J}_z$ whose eigenvalue is M. Both the PAV and the VAP effect could be considered in the AMP for the eigenstate of $\hat{J}_z$. Although the intrinsic state could become the superposition of the eigenstates of $\hat{J}_z$ [3, 19], we omit it for simplicity. [1]

[1] This effect is often called the K-mixing, and important for the γ-band [3, 37]. Although the ground-state rotational band will be mainly composed of the axially-symmetric intrinsic, it could be influenced by the K-mixing.

The intrinsic state $|\Phi_M\rangle$ is expanded by angular-momentum eigenstates $|JM\rangle$, where we omit indices other than J and M for simplicity,

$$|\Phi_M\rangle = \sum_J |JM\rangle \, \langle JM|\Phi_M\rangle \, . \tag{4.8}$$

The projection operator on the angular-momentum eigenstates $\hat{P}^{(J)}_{MM}$ is a special case of Eq. (B.4), which is hermitian and idempotent,

$$(\hat{P}^{(J)}_{MM})^\dagger = \hat{P}^{(J)}_{MM}, \tag{4.9a}$$

$$(\hat{P}^{(J)}_{MM})^2 = \hat{P}^{(J)}_{MM}. \tag{4.9b}$$

By using the orthogonal property of the Wigner D-function in Eq. (B.3), the projection operator is represented by the rotational operator in Eq. (B.1) and the Wigner D-function in Eq. (B.2) [see Eq. (B.4)]. The expectation values of the scalar operator $\hat{\mathcal{S}}$ on the angular momentum eigenstates are represented as follows:

$$\begin{aligned}
\langle J|\hat{\mathcal{S}}|J\rangle &= \frac{\langle\Phi_M|(\hat{P}^{(J)}_{MM})^\dagger \hat{\mathcal{S}} \hat{P}^{(J)}_{MM}|\Phi_M\rangle}{\langle\Phi_M|(\hat{P}^{(J)}_{MM})^\dagger \hat{P}^{(J)}_{MM}|\Phi_M\rangle} \\
&= \frac{\langle\Phi_M|\hat{\mathcal{S}} \hat{P}^{(J)}_{MM}|\Phi_M\rangle}{\langle\Phi_M|\hat{P}^{(J)}_{MM}|\Phi_M\rangle} \\
&= \frac{\langle\Phi_M|\hat{\mathcal{S}} \hat{P}^{J}_{MM}|\Phi_M\rangle}{\langle\Phi_M|\hat{P}^{J}_{MM}|\Phi_M\rangle} \\
&= \frac{\displaystyle\int_0^\pi d\beta \sin\beta \, d^{(J)}_{MM}(\beta) \, \langle\Phi_M|\hat{\mathcal{S}} \, e^{-i\hat{J}_y\beta}|\Phi_M\rangle}{\displaystyle\int_0^\pi d\beta \sin\beta \, d^{(J)}_{MM}(\beta) \, \langle\Phi_M|e^{-i\hat{J}_y\beta}|\Phi_M\rangle},
\end{aligned} \tag{4.10}$$

where β is the Euler angle around the y axis and $d^{(J)}_{MM}(\beta)$ is the Wigner d-function in Eq. (B.2b). Because the intrinsic state is the eigenstate of $\hat{J}_z$, the integrals of α and γ in Eq. (B.4) are done analytically. We omit the index M on the left-hand side (LHS) of Eq. (4.10) for simplicity. Since $e^{-i\hat{J}_y\beta}\,|\Phi_M\rangle$ is superposed with the weight function $d^{(J)}_{MM}(\beta)$ by the integral of the angle β in Eq. (4.10), the projection is often called the symmetry restoration, connected with the group theory [19].

By using the property [74] $d^{(J)}_{MM}(-\beta) = d^{(J)}_{MM}(\beta)$, the following relation is derived for $\hat{\mathcal{S}}$ and $|\Phi_M\rangle$:

$$\begin{aligned}
\langle\Phi_M|\hat{\mathcal{S}} \, e^{-i\hat{J}_y\beta}|\Phi_M\rangle &= \sum_J |\, \langle JM|\Phi_M\rangle \,|^2 \, \langle J|\hat{\mathcal{S}}|J\rangle \, d^{(J)}_{MM}(\beta) \\
&= \langle\Phi_M|\hat{\mathcal{S}} \, e^{i\hat{J}_y\beta}|\Phi_M\rangle \, .
\end{aligned} \tag{4.11}$$

Therefore, $\langle\Phi_M|\hat{\mathcal{S}} \, e^{-i\hat{J}_y\beta}|\Phi_M\rangle$ is an even function of β, and we have $\langle\Phi_M|\hat{\mathcal{S}} \, \hat{J}_y^{2n+1}|\Phi_M\rangle = 0$ for $n = 0, 1, 2, \ldots$, whose particular case is $\langle\Phi_M|\hat{J}_y|\Phi_M\rangle = 0$.

The following function is defined:

$$\mathcal{S}^{01}(\beta) := \frac{\langle\Phi_M|\hat{\mathcal{S}} \, e^{-i\hat{J}_y\beta}|\Phi_M\rangle}{\langle\Phi_M|e^{-i\hat{J}_y\beta}|\Phi_M\rangle}, \tag{4.12}$$

which is also an even function of β. The correlation function between operators $\hat{A}$ and $\hat{B}$ is defined as $C[\hat{A},\hat{B}] := \langle\hat{A}\hat{B}\rangle - \langle\hat{A}\rangle\,\langle\hat{B}\rangle$, where the bracket $\langle\,\rangle$ represents the expectation value at $|\Phi_M\rangle$. The above $\mathcal{S}^{01}(\beta)$ is related to the correlation function between $\hat{\mathcal{S}}$ and $\hat{J}_y^2$,

$$\frac{d^2}{d\beta^2}\,\mathcal{S}^{01}(\beta)\Big|_{\beta=0} = -\,C[\hat{\mathcal{S}},\hat{J}_y^2]. \tag{4.13}$$

The fluctuation of an operator $\hat{A}$ is defined as $\sigma[\hat{A}] := \sqrt{C[\hat{A},\hat{A}]}$. The overlap function $\langle\Phi_M|e^{-i\hat{J}_y\beta}|\Phi_M\rangle$ is related to the fluctuation of $\hat{J}_y$ as

$$\frac{d^2}{d\beta^2}\,\langle\Phi_M|e^{-i\hat{J}_y\beta}|\Phi_M\rangle\,\Big|_{\beta=0} = -\,(\sigma[\hat{J}_y])^2. \tag{4.14}$$

Concerning $C[\hat{\mathcal{S}},\hat{J}_y^2]$ and $(\sigma[\hat{J}_y])^2$, we have

$$C[\hat{\mathcal{S}},\hat{J}_x^2] = C[\hat{\mathcal{S}},\hat{J}_y^2] = \frac{1}{2}\,C[\hat{\mathcal{S}},\hat{\boldsymbol{J}}^2], \tag{4.15a}$$

$$(\sigma[\hat{J}_x])^2 = (\sigma[\hat{J}_y])^2 = \frac{1}{2}\,\Big(\,\langle\Phi_M|\hat{\boldsymbol{J}}^2|\Phi_M\rangle - M^2\Big)\,. \tag{4.15b}$$

Let us restrict ourselves to the even-even nuclei with $M = 0$. Extension to the $M \neq 0$ case is almost straightforward. We further assume that the state $|\Phi_0\rangle$ has the following symmetry:

$$\hat{\mathcal{R}}\,|\Phi_0\rangle = |\Phi_0\rangle\,, \quad \hat{\mathcal{R}} := e^{-i\hat{J}_y\pi}, \tag{4.16}$$

then $\langle J0|\Phi_0\rangle = 0$ for odd J. By using Eq. (4.11), the following equation is derived:

$$\langle\Phi_0|\hat{\mathcal{S}}\,e^{-i\hat{J}_y(\pi-\beta)}|\Phi_0\rangle = \langle\Phi_0|\hat{\mathcal{S}}\,e^{-i\hat{J}_y\beta}|\Phi_0\rangle\,. \tag{4.17}$$

From Eq. (4.17) and $d^{(J)}_{00}(\pi-\beta) = (-)^J d^{(J)}_{00}(\beta)$, the range of β integration in Eq. (4.10) can be reduced to $[0,\pi/2]$ [10, 17].

4.3 Previous derivation of $J(J+1)$ role with moment of inertia

In this section, the $J(J+1)$ rule is derived from the AMP for the well-deformed intrinsic state based on Refs. [3,7,8,10,11,13]. A more general and organized derivation is given in Sec. 4.4.

We derive the rotational energies for the axially-symmetric state $|\Phi_0\rangle$ here. By using Eq. (4.10) with $\hat{\mathcal{S}} = \hat{H}$ and $M = 0$, we get

$$\langle J|\hat{H}|J\rangle = \frac{\displaystyle\int_0^{\pi/2} d\beta\,\sin\beta\,d^{(J)}_{00}\,(\beta)\;\langle\Phi_0|\hat{H}e^{-i\hat{J}_y\beta}|\Phi_0\rangle}{\displaystyle\int_0^{\pi/2} d\beta\,\sin\beta\,d^{(J)}_{00}\,(\beta)\;\langle\Phi_0|e^{-i\hat{J}_y\beta}|\Phi_0\rangle}. \tag{4.18}$$

We assume that the integrands in Eq. (4.18) have contributions only near $\beta \approx 0$. The Wigner d-function is expanded as

$$d^{(J)}_{00}(\beta) = 1 - \frac{1}{4}J(J+1)\beta^2 + \frac{1}{192}\left[3\left\{J(J+1)\right\}^2 - 2J(J+1)\right]\beta^4 + O(\beta^6). \quad (4.19)$$

By using the following N_{2n} and H_{2n},

$$\begin{aligned} N_{2n} &:= \int_{\beta\approx 0} d\beta \sin\beta\, \beta^{2n} \langle\Phi_0|e^{-i\hat{J}_y\beta}|\Phi_0\rangle\,, \\ H_{2n} &:= \int_{\beta\approx 0} d\beta \sin\beta\, \beta^{2n} \langle\Phi_0|\hat{H}e^{-i\hat{J}_y\beta}|\Phi_0\rangle\,, \quad (n = 0, 1, 2, \cdots), \end{aligned} \quad (4.20)$$

Eq. (4.18) is expanded as follows:

$$\begin{aligned} \langle J|\hat{H}|J\rangle &\approx \frac{\displaystyle\int_{\beta\approx 0} d\beta \sin\beta\, d^{(J)}_{00}(\beta)\, \langle\Phi_0|\hat{H}e^{-i\hat{J}_y\beta}|\Phi_0\rangle}{\displaystyle\int_{\beta\approx 0} d\beta \sin\beta\, d^{(J)}_{00}(\beta)\, \langle\Phi_0|e^{-i\hat{J}_y\beta}|\Phi_0\rangle} \\ &\approx \frac{H_0 - \frac{1}{4}H_2 J(J+1) + \cdots}{N_0 - \frac{1}{4}N_2 J(J+1) + \cdots} \\ &\approx \frac{H_0}{N_0} + \frac{1}{4}\frac{H_0}{N_0}\left(\frac{N_2}{N_0} - \frac{H_2}{H_0}\right) J(J+1) + \cdots . \end{aligned} \quad (4.21)$$

We define the moment of inertia $\mathcal{I}_{\rm PY}$ as

$$\frac{1}{\mathcal{I}_{\rm PY}} := \frac{1}{2}\frac{H_0}{N_0}\left(\frac{N_2}{N_0} - \frac{H_2}{H_0}\right), \quad (4.22)$$

then, Eq. (4.21) is represented as

$$\langle J|\hat{H}|J\rangle \approx \langle 0|\hat{H}|0\rangle + \frac{J(J+1)}{2\,\mathcal{I}_{\rm PY}} + \cdots . \quad (4.23)$$

This is the original derivation of the moment of inertia by Peierls and Yoccoz [7].

By using Eq. (4.22), we shall derive the Yoccoz moment of inertia. The Gaussian approximation is applied for $\langle\Phi_0|e^{-i\hat{J}_y\beta}|\Phi_0\rangle$ and $\langle\Phi_0|\hat{H}e^{-i\hat{J}_y\beta}|\Phi_0\rangle$ as [2]

$$\begin{aligned} \langle\Phi_0|e^{-i\hat{J}_y\beta}|\Phi_0\rangle &\approx 1 - \frac{1}{2}\langle\Phi_0|\hat{J}_y^2|\Phi_0\rangle\,\beta^2 + O(\beta^4) \\ &\approx \exp\left(-\frac{1}{2}\langle\Phi_0|\hat{J}_y^2|\Phi_0\rangle\,\beta^2\right), \\ \langle\Phi_0|\hat{H}e^{-i\hat{J}_y\beta}|\Phi_0\rangle &\approx \langle\Phi_0|\hat{H}|\Phi_0\rangle - \frac{1}{2}\langle\Phi_0|\hat{H}\hat{J}_y^2|\Phi_0\rangle\,\beta^2 + O(\beta^4) \\ &\approx \exp\left(-\frac{1}{2}\langle\Phi_0|\hat{J}_y^2|\Phi_0\rangle\,\beta^2\right) \\ &\quad \times \left(\langle\Phi_0|\hat{H}|\Phi_0\rangle - \frac{1}{2}C[\hat{H}, \hat{J}_y^2]\beta^2 + O(\beta^4)\right), \\ C[\hat{H}, \hat{J}_y^2] &= \langle\Phi_0|\hat{H}\hat{J}_y^2|\Phi_0\rangle - \langle\Phi_0|\hat{H}|\Phi_0\rangle\,\langle\Phi_0|\hat{J}_y^2|\Phi_0\rangle\,, \end{aligned} \quad (4.24)$$

[2] If the intrinsic state $|\Phi_0\rangle$ is deformed well, this Gaussian approximation works well.

then by replacing the range of β integral with $[0, \infty)$ and using $\sin\beta \approx \beta$ in Eq. (4.20), Eq. (4.22) becomes

$$\frac{1}{\mathcal{I}_{\rm PY}} \approx \frac{1}{\mathcal{I}_{\rm Y}} := \frac{\langle\Phi_0|\hat{H}\hat{J}_y^2|\Phi_0\rangle - \langle\Phi_0|\hat{H}|\Phi_0\rangle\ \langle\Phi_0|\hat{J}_y^2|\Phi_0\rangle}{\langle\Phi_0|\hat{J}_y^2|\Phi_0\rangle^2}. \tag{4.25}$$

The Yoccoz moment of inertia $\mathcal{I}_{\rm Y}$ is now derived. The Kamlah expansion [3, 13] is introduced in Appendix C, where the Yoccoz moment of inertia is derived again. The cranking term is derived from the Kamlah expansion approximately. The moment of inertia derived from the cranking model and the RPA is summarized in Appendix D, where the intrinsic state has neither axial symmetry nor time-reversal symmetry.

We here summarize the rotational energy for the well-deformed intrinsic state. In the case of the axially-symmetric intrinsic state $|\Phi_0\rangle$, the Yoccoz moment of inertia $\mathcal{I}_{\rm Y}$ in Eq. (4.25) is good for approximation. The Yoccoz moment of inertia could also consider the VAP effect via the intrinsic state $|\Phi_0\rangle$. As J increases, the value of the Yoccoz moment of inertia could become large gradually with the axial symmetry, then the $J(J+1)$ rule for the rotational energy could be broken. In addition to the Yoccoz moment of inertia, Eq. (C.4) suggests that the intrinsic state without both axial and time-reversal symmetry could influence the $J(J+1)$ rule and the moment of inertia. The effect of the pair correlations for the rotational energy is omitted here, as will be discussed in Sec. 4.5.

However, it is not sufficiently clear whether the same argument holds particularly for the light or the weakly-deformed intrinsic states. In this study, the formulae in Eqs. (4.22) and (4.25) have been generalized, as will be presented in Sec. 4.4 and Chap. F.

4.4 Revised theory of AMP and rotation with cumulant expansion

In this section, the revised theory of the AMP and the rotation with cumulant expansion is discussed. The $J(J+1)$ rule of rotational energy and the moment of inertia connected with Eq. (4.10) for the well-deformed nuclei have discussed in Sec. 4.3 with Refs. [3, 7, 8, 10, 11, 13]. If the overlap function $\langle\Phi_0|e^{-i\hat{J}_y\beta}|\Phi_0\rangle$ has a sharp peak at $\beta \approx 0$, the energy spectrum is close to the $J(J+1)$ rule. However, it is not always clear whether $\langle\Phi_0|e^{-i\hat{J}_y\beta}|\Phi_0\rangle$ has a sharp peak at $\beta \approx 0$. In the following, we present a more general argument on the rotational energy than those in Refs. [7,10] by using the cumulant expansion [75]. The cumulant expansion is summarized in Appendix E. This formulation is useful in some cases, as will be discussed in Sec. 7.

We expand $d^{(J)}_{00}(\beta)$ by the power series of β,

$$d^{(J)}_{00}(\beta) = \sum_{n=0}^{\infty} c_{2n}\beta^{2n}, \tag{4.26a}$$

$$c_{2n} = \frac{(-)^n}{(2n)!}\langle J0|\hat{J}_y^{2n}|J0\rangle = \frac{\langle J0|(\hat{J}_+ - \hat{J}_-)^{2n}|J0\rangle}{(2n)!\,2^{2n}}. \tag{4.26b}$$

Equation (4.26b) leads to

$$c_0 = 1, \tag{4.27a}$$

$$c_2 = -\frac{1}{2!\,2}\,J(J+1), \tag{4.27b}$$

$$c_4 = \frac{1}{4!\,2^3}\,J(J+1)\left[3J(J+1)-2\right], \cdots . \tag{4.27c}$$

The coefficient c_{2n} depends only on J. In terms of the cumulant in Eq. (E.5), $\mathcal{S}^{01}(\beta)$ in Eq. (4.12) is expanded as follows:

$$\mathcal{S}^{01}(\beta) = \sum_{n=0}^{\infty} s_{2n}\beta^{2n}, \tag{4.28a}$$

$$s_{2n} = \frac{(-)^n}{(2n)!}\,\langle\Phi_0|\hat{\mathcal{S}};\underbrace{\hat{J}_y;\cdots;\hat{J}_y}_{2n}|\Phi_0\rangle_{\rm cum}\,. \tag{4.28b}$$

Equation (4.28b) leads to

$$s_0 = \langle\Phi_0|\hat{\mathcal{S}}|\Phi_0\rangle\,, \tag{4.29a}$$

$$s_2 = -\frac{1}{2!}\,C[\hat{\mathcal{S}},\hat{J}_y^2], \tag{4.29b}$$

$$s_4 = \frac{1}{4!}\left(C[\hat{\mathcal{S}},\hat{J}_y^4] - 6\,C[\hat{\mathcal{S}},\hat{J}_y^2](\sigma[\hat{J}_y])^2\right), \cdots . \tag{4.29c}$$

The coefficient s_{2n} is independent of J, depending only on $|\Phi_0\rangle$ and $\hat{\mathcal{S}}$. By defining the following quantities:

$$N_{2n} := \int_0^{\pi/2} d\beta \sin\beta\,\beta^{2n}\,\langle\Phi_0|e^{-i\hat{J}_y\beta}|\Phi_0\rangle\,, \tag{4.30a}$$

$$\Lambda_{2n} := \frac{N_{2n}}{N_0}, \quad (n=0,1,2,\ldots), \tag{4.30b}$$

which are determined only by $|\Phi_0\rangle$, Eq. (4.10) is rewritten as

$$\begin{aligned}\langle J|\hat{\mathcal{S}}|J\rangle &= \frac{\displaystyle\int_0^{\pi/2} d\beta \sin\beta\, d_{00}^{(J)}(\beta)\;\langle\Phi_0|e^{-i\hat{J}_y\beta}|\Phi_0\rangle\,\mathcal{S}^{01}(\beta)}{\displaystyle\int_0^{\pi/2} d\beta \sin\beta\, d_{00}^{(J)}(\beta)\;\langle\Phi_0|e^{-i\hat{J}_y\beta}|\Phi_0\rangle} \\ &= \frac{\displaystyle\sum_{m,n=0}^{\infty} c_{2m}s_{2n}N_{2m+2n}}{\displaystyle\sum_{\ell=0}^{\infty} c_{2\ell}N_{2\ell}} \\ &= \frac{\displaystyle\sum_{m,n=0}^{\infty} c_{2m}s_{2n}\Lambda_{2m+2n}}{\displaystyle\sum_{\ell=0}^{\infty} c_{2\ell}\Lambda_{2\ell}}.\end{aligned} \tag{4.31}$$

For $J = 0$, c_{2n} vanishes for $n \geq 1$, and the following equation is obtained:

$$\langle 0|\hat{\mathcal{S}}|0\rangle = \sum_{n=0}^{\infty} s_{2n}\Lambda_{2n} = \langle \Phi_0|\hat{\mathcal{S}}|\Phi_0\rangle + \sum_{n=1}^{\infty} s_{2n}\Lambda_{2n}. \tag{4.32}$$

In the present expression, the energy difference $\langle J|\hat{H}|J\rangle - \langle 0|\hat{H}|0\rangle$ for an axial-MF state $|\Phi_0\rangle$, where $\hat{H}$ is the Hamiltonian, is the rotational energy.

For the denominator on the right-hand side (RHS) of Eq. (4.31), we have

$$\sum_{n=0}^{\infty} c_{2n}\Lambda_{2n} = 1 + \sum_{n=1}^{\infty} c_{2n}\Lambda_{2n} = \frac{1}{2J+1}\left|\frac{\langle J0|\Phi_0\rangle}{\langle 00|\Phi_0\rangle}\right|^2, \tag{4.33}$$

where we used the relation $N_0 = |\langle 00|\Phi_0\rangle|^2$. The inequality $|\sum_{n=1}^{\infty} c_{2n}\Lambda_{2n}| < 1$ is usually satisfied. We have numerically confirmed via the RHS of Eq. (4.33) [see Sec. 7.2]. We then expand Eq. (4.31) as

$$\begin{aligned}
\langle J|\hat{\mathcal{S}}|J\rangle &= \left(\sum_{m,n=0}^{\infty} s_{2n}c_{2m}\Lambda_{2n+2m}\right)\left(1 + \sum_{\ell=1}^{\infty} c_{2\ell}\Lambda_{2\ell}\right)^{-1} \\
&= \left(\sum_{m=0}^{\infty}\sum_{n=0}^{\infty} s_{2n}c_{2m}\Lambda_{2n+2m}\right) \\
&\quad \times \left[1 - \sum_{\ell=1}^{\infty} c_{2\ell}\Lambda_{2\ell} + \left(\sum_{\ell=1}^{\infty} c_{2\ell}\Lambda_{2\ell}\right)^2 - \cdots\right].
\end{aligned} \tag{4.34}$$

In order to analyze J dependence of $\langle J|\hat{\mathcal{S}}|J\rangle$, with taking account of $c_{2n} \sim J^{2n}$, it is appropriate to arrange Eq. (4.34) by c_{2n} as

$$\begin{aligned}
\langle J|\hat{\mathcal{S}}|J\rangle &= \left(\sum_{n=0}^{\infty} s_{2n}\Lambda_{2n} + c_2\sum_{n=0}^{\infty} s_{2n}\Lambda_{2n+2} + c_4\sum_{n=0}^{\infty} s_{2n}\Lambda_{2n+4} + \cdots\right) \\
&\quad \times \left[1 - (c_2\Lambda_2 + c_4\Lambda_4 + \cdots) + (c_2\Lambda_2)^2 + \cdots\right] \\
&= \sum_{n=0}^{\infty} s_{2n}\Lambda_{2n} + c_2\sum_{n=1}^{\infty} s_{2n}\left(\Lambda_{2n+2} - \Lambda_{2n}\Lambda_2\right) \\
&\quad + c_4\left(\sum_{n=1}^{\infty} s_{2n}\left(\Lambda_{2n+4} - \Lambda_{2n}\Lambda_4\right)\right) \\
&\quad - (c_2)^2\left(\sum_{n=1}^{\infty} s_{2n}\left[\Lambda_{2n+2}\Lambda_2 - \Lambda_{2n}(\Lambda_2)^2\right]\right) + \cdots .
\end{aligned} \tag{4.35}$$

Compared with the Kamlah expansion [3, 13], the cumulant expansion of Eq. (4.28) enables a more organized expansion of the rotational energy. We call the $n \geq 2$ terms of c_{2n} in Eq. (4.35) *higher-c_{2n} terms*, and those of s_{2n} *higher-s_{2n} terms*. If the higher-c_{2n} terms are neglected, Eq. (4.35) is approximated as

$$\langle J|\hat{\mathcal{S}}|J\rangle \approx \langle 0|\hat{\mathcal{S}}|0\rangle + \frac{J(J+1)}{2\,\mathcal{I}[\mathcal{S}]}, \tag{4.36}$$

where,

$$\frac{1}{\mathcal{I}[\hat{\mathcal{S}}]} := \sum_{n=1}^{\infty} s_{2n} \left[-\frac{1}{2}(\Lambda_{2n+2} - \Lambda_{2n}\Lambda_2) \right]. \tag{4.37}$$

For $\hat{\mathcal{S}} = \hat{H}$, the parameter $\mathcal{I}[\hat{H}]$ is interpreted as the moment of inertia. If the higher-s_{2n} terms are neglected in Eqs. (4.32) and (4.37), $\langle 0|\hat{\mathcal{S}}|0\rangle$ and $\mathcal{I}[\hat{\mathcal{S}}]$ are approximated as

$$\langle 0|\hat{\mathcal{S}}|0\rangle \approx \langle \Phi_0|\hat{\mathcal{S}}|\Phi_0\rangle - \frac{1}{2} C[\hat{\mathcal{S}}, \hat{J}_y^2]\Lambda_2, \tag{4.38a}$$

$$\frac{1}{\mathcal{I}[\hat{\mathcal{S}}]} \approx \frac{1}{4} C[\hat{\mathcal{S}}, \hat{J}_y^2]\,[\Lambda_4 - (\Lambda_2)^2]. \tag{4.38b}$$

Equation (4.38b) gives the moment of inertia of Peierls and Yoccoz [7, 10]. Equation (4.37) is regarded as a generalization of Eq. (4.38b). From Eqs. (4.32), (4.37), and (4.38), it is noticed that the higher-s_{2n} terms may contribute to $\langle 0|\hat{\mathcal{S}}|0\rangle$ and $\mathcal{I}[\hat{\mathcal{S}}]$. We shall see such a situation in Sec. 7.2. Further approximation based on the Gaussian approximation [3, 8, 11, 13] with the higher-s_{2n} terms is discussed in Appendix F.

We here summarize the advantages and the disadvantages of the above re-formulation of the theory of rotation connected with the AMP compared with the previous theory in Sec. 4.3 with Refs. [3, 7, 8, 10, 11, 13]. The advantages are as follows:

- The expansion in Eq. (4.35) is the most general one in the axially-symmetric state. Especially, the moment of inertia is generalized in Eq. (4.37) with the $J(J+1)$ rule for both strong and weak symmetry broken states.
- This formulation will also be applicable to other symmetry restoration, e.g., the number projection (NP) or the double projection (both the AMP and the NP), straightforwardly. [3] It is essential that the cumulant in Eq. (E.1) is defined only for any operators which commute each other. [4]
- The cumulant for the intrinsic state would be reasonable for the interpretation of the symmetry restoration.

The disadvantage is as follows:

- The cumulant could not be defined for the operators which do not commute each other, *e.g.*, $\hat{J}_y$ and $\hat{J}_z$. [5] Since the projection operator on the angular-momentum eigenstates in Eq. (B.4) includes both the rotational operators $e^{-i\hat{J}_y\beta}$ and $e^{-i\hat{J}_z\alpha}$, we have needed to restrict ourselves in the eigenstate of $\hat{J}_z$ and treat the only β integral in Eq. (4.10). The cumulant expansion may not be applicable to the rotation accompanied by the breaking of the axial symmetry, i.e., the intrinsic state $|\Phi\rangle$ is the superposition of the eigenstates of both $\hat{\boldsymbol{J}}^2$ and $\hat{J}_z$.

In this study, the $J(J+1)$ rule and the moment of inertia are also investigated numerically by the AMP with the cumulant expansion, as will be discussed in Chap. 7.

[3] See Eqs. (E.5) and (E.6) for tips.

[4] The unitary operators which commute each other, *e.g.*, $e^{-i\hat{J}_y\beta}$ and $e^{-i\hat{J}_y\beta'}$, belong to the abelian group [19].

[5] The unitary operators which do not commute each other, *e.g.*, $e^{-i\hat{J}_y\beta}$ and $e^{-i\hat{J}_z\alpha}$, belong to the non-abelian group [19].

4.5 Pair correlation and rotation

In this section, the relation between the pair correlation and the rotation of nuclei is discussed. In the cranking model [see Appendix D], the cranking term $-\omega\hat{J}_x$ in Eq. (D.1) breaks both axial symmetry and time-reversal symmetry. Therefore, the solution obtained by the cranking equation in Eq. (C.5) has neither axial nor time-reversal symmetry. On the other hand, in the BCS, HF+BCS, or HFB theory, the time-reversed state is often used as a conjugate state in Eq. (6.23). The pair condensation for the time-reversal pair will be broken as the angular velocity ω increases, which is well known as the Mottelson-Valatin effect (or the nuclear Meissner effect) [3, 76]. The Belyaev formula in Eq. (D.3) suggests that the excitation energy increases because the moment of inertia becomes small. Thus, according to the Mottelson-Valatin effect and the Belyaev formula, the excitation energy will decrease from the $J(J+1)$ values as J increases.

It is fair to say that there could be other effects on the rotational energy except the cranking. The gradual stretching effect accompanied by increasing J could be allowed as a VAP effect even if the intrinsic state has axial symmetry ($M = 0$), irrespective of well-deformed or weakly-deformed nuclei. Since many even-even nuclei have the pair correlations, their states near the ground state will have the time-reversal pair. Therefore, the intrinsic states at a low angular momentum J in the ground-state rotational band of even-even nuclei could have time-reversal symmetry. The pairing correlations could decrease by increasing J as a VAP effect of the double projection (both the AMP and the NP) on the axially-symmetric intrinsic state.

Although there are some effects of the VAP and the cranking on the rotational energy, numerical calculations considering the VAP and the cranking with the M3Y-type interaction are not yet easy. In this study, the rotational energy for the fixed intrinsic state with the axial symmetry is focused on in the framework of the PAV, as will be explained in Sec. 6.4.

4.6 Electric moment and transition

In this section, the electric moment and transition related to the deformation and rotation of nuclei are introduced [1, 3, 77]. Since the theory of the EM transition (or the γ transition) in nuclear physics is well established, they are not so focused on in this paper. In this section, $\hbar$ and c are not 1.

We consider processes that an isolated nucleus emits or absorbs a photon. The Hamiltonian is composed of the nucleus term $H_{\text{nucl.}}$, the EM-field term H_{field}, and the interaction term between the nucleus and the EM field $H_{\text{int.}}$ as

$$H = H_{\text{nucl.}} + H_{\text{field}} + H_{\text{int.}}, \tag{4.39a}$$

$$H_{\text{int.}} = \frac{1}{c}\int d^3r\, j_\mu(\mathbf{r},t)A^\mu(\mathbf{r},t) \tag{4.39b}$$

$$= \int d^3r\, \rho(\mathbf{r},t)\phi(\mathbf{r},t) - \frac{1}{c}\int d^3r\, \boldsymbol{j}(\mathbf{r},t)\cdot\mathbf{A}(\mathbf{r},t), \tag{4.39c}$$

where $j^\mu = (c\rho, \boldsymbol{j})$, and $A^\mu = (\phi, \mathbf{A})$. Since the EM interaction is weak, the EM transition probability $w_{i\to f}$ in the unit of s^{-1} from the initial state $|i\rangle$ to the final state

$|f\rangle$ is calculated approximately by using the Fermi's golden rule,

$$w_{i\to f} \approx \frac{2\pi}{\hbar} |\langle f|\hat{H}_{\rm int.}|i\rangle|^2 g(E_f), \tag{4.40}$$

where $g(E_f)$ is the density of states at the energy E_f of the final states. [6]

In the perturbation theory, it is necessary to obtain the solution of the Maxwell equation without sources. The maxwell equation derives the wave equation for the vector potential $\mathbf{A}(\mathbf{r},t)$,

$$\left(\frac{1}{c^2}\frac{\partial}{\partial t} - \nabla^2\right)\mathbf{A}(\mathbf{r},t) = 0. \tag{4.41}$$

It is convenient to use the following gauge-fixing condition for the scalar potential $\phi(\mathbf{r},t)$ and the vector potential $\mathbf{A}(\mathbf{r},t)$:

$$\phi(\mathbf{r},t) = 0, \quad \nabla\cdot\mathbf{A}(\mathbf{r},t) = 0, \tag{4.42}$$

which is called the radiational gauge or the Coulomb gauge. The time dependence of the EM field is assumed to be periodic, i.e., e^{-ikct} or e^{ikct}, then the vector potential $\mathbf{A}(\mathbf{r})$ obeys the Helmholtz equation as

$$\left(\nabla^2 + k^2\right)\mathbf{A}(\mathbf{r}) = 0. \tag{4.43}$$

Since the photon is emitted or absorbed from the isolated nucleus, the Helmholtz equation in Eq. (4.43) is solved with the spherical boundary condition. The solution of Eq. (4.43) could be expanded by $j_\lambda(kr)\mathbf{Y}_\mu^{(\ell 1;\lambda)}(\hat{\mathbf{r}})$, where $j_\lambda(kr)$ is the spherical Bessel function, and $\mathbf{Y}_\mu^{(\ell 1;\lambda)}(\hat{\mathbf{r}})$ is the vector spherical harmonics,

$$\mathbf{Y}_\mu^{(\ell 1;\lambda)}(\hat{\mathbf{r}}) := \sum_{\ell_z\mu'} \langle \ell 1 \ell_z\mu'|(\ell 1)\lambda\mu\rangle\, Y_{\ell_z}^{(\ell)}(\hat{\mathbf{r}})\mathbf{e}_{\mu'}^{(1)}. \tag{4.44}$$

where $r := |\mathbf{r}|$, and $\hat{\mathbf{r}} := \mathbf{r}/r$. The vector spherical harmonics has the orthogonal property,

$$\int_0^{2\pi} d\phi \int_0^{\pi} d\theta \sin\theta\, \mathbf{Y}_\mu^{(\ell 1;\lambda)*}(\hat{\mathbf{r}})\cdot\mathbf{Y}_{\mu'}^{(\ell' 1;\lambda')}(\hat{\mathbf{r}}) = \delta_{\ell\ell'}\delta_{\lambda\lambda'}\delta_{\mu\mu'}. \tag{4.45}$$

The component of the EM field which has the parity $(-)^\lambda$ ($(-)^{\lambda+1}$) is called *electric (magnetic) component*. According to Eq. (4.42), the angular part of the vector potential $\mathbf{A}(\mathbf{r})$ is expanded by

$$\begin{pmatrix}\mathbf{Y}_\mu^{(L,\lambda)}\\ \mathbf{Y}_\mu^{(M,\lambda)}\\ \mathbf{Y}_\mu^{(E,\lambda)}\end{pmatrix} := \begin{pmatrix}\hat{\mathbf{r}}Y_\mu^{(\lambda)}\\ \frac{1}{\sqrt{\lambda(\lambda+1)}}\mathbf{L}Y_\mu^{(\lambda)}\\ \frac{1}{\sqrt{\lambda(\lambda+1)}}\hat{\nabla}Y_\mu^{(\lambda)}\end{pmatrix} = \begin{pmatrix}\sqrt{\frac{\lambda}{2\lambda+1}} & 0 & -\sqrt{\frac{\lambda+1}{2\lambda+1}}\\ 0 & 1 & 0\\ \sqrt{\frac{\lambda+1}{2\lambda+1}} & 0 & \sqrt{\frac{\lambda}{2\lambda+1}}\end{pmatrix}\begin{pmatrix}\mathbf{Y}_\mu^{(\lambda-1\,1;\lambda)}\\ \mathbf{Y}_\mu^{(\lambda 1;\lambda)}\\ \mathbf{Y}_\mu^{(\lambda+1\,1;\lambda)}\end{pmatrix}, \tag{4.46}$$

where $\mathbf{L} := -i\,\mathbf{r}\times\nabla$, and $\hat{\nabla} := r\nabla - \mathbf{r}\frac{\partial}{\partial r}$. The longitudinal, electric, and magnetic components are represented as the indices L, M, and E. For $\mathbf{Y}_\mu^{(M,\lambda)}(\hat{\mathbf{r}})$ and $\mathbf{Y}_\mu^{(E,\lambda)}(\hat{\mathbf{r}})$,

[6] The (mean) lifetime of nuclei τ is related to $w_{i\to f}$ as $\tau = (w_{i\to f})^{-1}$ and the half life T as $T = (\ln 2)\tau$. The lifetime of nuclei could be observed experimentally.

the component of $\lambda = 0$ is excluded. Since $\nabla \cdot \mathbf{Y}_\mu^{(M,\lambda)}(\hat{\mathbf{r}}) = \nabla \cdot \mathbf{Y}_\mu^{(E,\lambda)}(\hat{\mathbf{r}}) = 0$, and $\nabla \cdot \mathbf{Y}_\mu^{(L,\lambda)}(\hat{\mathbf{r}}) \neq 0$, the longitudinal component $\mathbf{Y}_\mu^{(L,\lambda)}(\hat{\mathbf{r}})$ in Eq. (4.46) has been excluded from the vector potential $\mathbf{A}(\mathbf{r})$. In other words, the gauge condition in Eq. (4.42) is regarded as a projection on the function space which is expanded by $\mathbf{Y}_\mu^{(M,\lambda)}$ and $\mathbf{Y}_\mu^{(E,\lambda)}$ in Eq. (4.46).

The boundary condition of the magnetic components of the EM field gives a n th root of the spherical Bessel function $k_n^{(\lambda)} R$ as

$$j_\lambda(k_n^{(\lambda)} R) = 0\,. \tag{4.47}$$

where radius R is a large value, introduced only to consider the spherical boundary condition. In the case of the electric components of the EM field, we get

$$\frac{\partial}{\partial r} r j_\lambda(k_n^{(\lambda+1)} r)\bigg|_{r=R} = 0\,. \tag{4.48}$$

By using

$$j_\lambda(k_n^{(\lambda)} R) \approx \frac{1}{k_n^{(\lambda)} R} \sin\!\left(k_n^{(\lambda)} R - \frac{\lambda\pi}{2}\right), \tag{4.49}$$

the following equation is derived from Eqs. (4.47) and (4.48):

$$k_n^{(\lambda)} R = \frac{(\lambda + 2n)\pi}{2}\,, \quad n = 0, \pm 1, \pm 2, \cdots\,, \tag{4.50}$$

then

$$g(E_f) = \frac{1}{\hbar c (k_{n+1}^{(\lambda)} - k_n^{(\lambda)})} = \frac{R}{\hbar c \pi}. \tag{4.51}$$

The spherical Bessel function has the orthogonal property as

$$\int_0^R dr\, r^2 j_\lambda(k_m^{(\lambda)} r) j_\lambda(k_n^{(\lambda)} r) = \delta_{mn} \frac{R^3}{2} [j_{\lambda+1}(k_n^{(\lambda)} R)]^2. \tag{4.52}$$

By using Eqs. (4.49) and (4.50), we get

$$[j_{\lambda+1}(k_n^{(\lambda)} R)]^2 \approx \left[\frac{1}{k_n^{(\lambda)} R} \sin\!\left(k_n^{(\lambda)} R - \frac{(\lambda+1)\pi}{2}\right)\right]^2 = \frac{1}{(k_n^{(\lambda)} R)^2}. \tag{4.53}$$

The state of the photon is represented by the indices $(\pi k \lambda \mu)$, π represents the electric and magnetic components of the EM field, k is the wave number of the photon, and $(\lambda\mu)$ are the indices of the angular momentum. The vector potential $\mathbf{A}(\mathbf{r}, t)$ is quantized by the multipole expansion as

$$\hat{\mathbf{A}}(\mathbf{r}, t) = \sum_{\pi \in \{E,M\}} \sum_{k\lambda\mu} \left(a_{\pi k\lambda\mu}^\dagger \mathbf{A}_{\pi k\lambda\mu}(\mathbf{r}) e^{-ikct} + a_{\pi k\lambda\mu} \mathbf{A}_{\pi k\lambda\mu}^*(\mathbf{r}) e^{ikct} \right), \tag{4.54}$$

where

$$\begin{aligned} \mathbf{A}_{Mk\lambda\mu}(\mathbf{r}) &= \mathcal{N} j_\lambda(kr) \mathbf{Y}_\mu^{(M,\lambda)}(\hat{\mathbf{r}}) \\ &= \mathcal{N} \frac{1}{\sqrt{\lambda(\lambda+1)}} \frac{1}{i} (\mathbf{r} \times \nabla) j_\lambda(kr) Y_\mu^{(\lambda)}(\hat{\mathbf{r}}), \\ \mathbf{A}_{Ek\lambda\mu}(\mathbf{r}) &= \frac{i}{k} \nabla \times \mathbf{A}_{Mk\lambda\mu}(\mathbf{r}) \\ &= \mathcal{N} \frac{i}{k} \nabla \times j_\lambda(kr) \mathbf{Y}_\mu^{(M,\lambda)}(\hat{\mathbf{r}}), \end{aligned} \tag{4.55}$$

with the normalization constant $\mathcal{N} = \sqrt{4\pi\hbar ck/R}$. [7] The creation and annihilation operators obey the bosonic commutation relations,

$$[a_{\pi k\lambda\mu}, a^\dagger_{\pi' k'\lambda'\mu'}] = \delta_{\pi\pi'}\delta_{kk'}\delta_{\lambda\lambda'}\delta_{\mu\mu'}, \qquad [a_{\pi k\lambda\mu}, a_{\pi' k'\lambda'\mu'}] = 0, \qquad [a^\dagger_{\pi k\lambda\mu}, a^\dagger_{\pi' k'\lambda'\mu'}] = 0. \tag{4.56}$$

The particle vacuum for the photon $|0\rangle_a$ is defined by

$$a_{\pi k\lambda\mu}\,|0\rangle_a = 0, \quad \text{for all } \ (\pi k\lambda\mu), \tag{4.57}$$

which satisfies ${}_a\langle 0|0\rangle_a = 1$.

In the following, we focus on the electric transition. We represent the initial state of nuclei as $|J_i M_i\rangle$ and the final state of nuclei as $|J_f M_f\rangle$, where indices other than (JM) are omitted. Since the initial state of nuclei $|J_i M_i\rangle$ are degenerate for M_i, the transition probability in Eq. (4.40) is averaged statistically as

$$w_{i\to f} = T_{fi}(E, k\lambda) := \frac{1}{2J_i+1}\sum_{M_i,M_f,\mu} T_{fi}(E, k\lambda\mu). \tag{4.58}$$

By using Eqs. (4.39c), (4.40), (4.51), and (4.55), and the continuity equation $\nabla\cdot\boldsymbol{j}(\mathbf{r}) = ikc\rho(\mathbf{r})$, we obtain the following equation:

$$T_{fi}(E, k\lambda\mu) = \frac{8\pi}{\hbar}\,\frac{(\lambda+1)}{\lambda[(2\lambda+1)!!]^2}\,k^{2\lambda+1}\left|\,\langle J_f M_f|\hat{\mathcal{M}}(E\lambda\mu)|J_i M_i\rangle\right|^2, \tag{4.59}$$

where the electric transition operator $\hat{\mathcal{M}}(E\lambda\mu)$ is represented as [8]

$$\begin{aligned}\mathcal{M}(E\lambda\mu) =& \frac{1}{k^\lambda}\,\frac{(2\lambda+1)!!}{\lambda+1}\int d^3r \\ &\times\left[\rho_{\rm proton}(\mathbf{r})\,\left(\frac{\partial}{\partial r} r j_\lambda(kr)\right) Y^{(\lambda)}_\mu(\hat{\mathbf{r}}) + \frac{ik}{c}(\boldsymbol{j}(\mathbf{r})\cdot\mathbf{r}) j_\lambda(kr) Y^{(\lambda)}_\mu(\hat{\mathbf{r}})\right].\end{aligned} \tag{4.60}$$

The reduced transition probability is defined as

$$\begin{aligned}B(E\lambda; J_i\to J_f) :=& \frac{1}{2J_i+1}\sum_{M_i,M_f,\mu} |\,\langle J_f M_f|\hat{\mathcal{M}}(E\lambda\mu)|J_i M_i\rangle\,|^2 \\ =& \frac{1}{2J_i+1}|\,\langle J_f||\hat{\mathcal{M}}(E\lambda\mu)||J_i\rangle\,|^2,\end{aligned} \tag{4.61}$$

in the unit of $e^2\,\mathrm{fm}^{2\lambda}$ [e is the elementary charge]. By using Eqs. (4.58), (4.59), and (4.61), we get the well-known formula,

$$T_{fi}(E, k\lambda) = \frac{8\pi}{\hbar}\,\frac{(\lambda+1)}{\lambda[(2\lambda+1)!!]^2}\,k^{2\lambda+1}B(E\lambda; J_i\to J_f). \tag{4.62}$$

[7] This normalization constant is determined by the condition that the EM energy is $\hbar ck$.

[8] We have omitted here the correction of the center-of-mass of nuclei for simplicity [31]. The contributions of the neutrons to the EM transition [78] has also been omitted.

The reduced transition probability $B(E\lambda; J_i \to J_f)$ in Eq. (4.62) depends on only the states of nuclei. By using Eq. (4.61) and the symmetry properties of the Clebsch-Gordan coefficients [1, 73], we get

$$\frac{B(E\lambda; J_i \to J_f)}{B(E\lambda; J_f \to J_i)} = \frac{2J_f + 1}{2J_i + 1}. \tag{4.63}$$

In the case of nuclei, the long wave approximation $kR_0 \ll 1$ with the radius of a nucleus R_0 works well. By using

$$j_\lambda(kr) \approx \frac{(kr)^\lambda}{(2\lambda+1)!!}\left(1 - \frac{1}{2}\frac{(kr)^2}{2\lambda+3} + \cdots\right), \tag{4.64}$$

the electric transition operator $\hat{\mathcal{M}}(E\lambda\mu)$ in Eq. (4.60) is approximated as

$$\mathcal{M}(E\lambda\mu) \approx Q_\mu^{(\lambda)} := \int d^3r \rho_{\text{proton}}(\mathbf{r})\, r^\lambda\, Y_\mu^{(\lambda)}(\hat{\mathbf{r}}), \tag{4.65}$$

where $Q_\mu^{(\lambda)}$ is the static electric-multipole operator. Equation (4.65) does not depend on the wave number k. The static electric-multipole operator $Q_\mu^{(\lambda)}$ is also represented as

$$Q_\mu^{(\lambda)} = \sum_{i \in \text{proton}} r_i^\lambda\, Y_\mu^{(\lambda)}(\hat{\mathbf{r}}_i). \tag{4.66}$$

The electric quadrupole moment for the intrinsic state q_{proton} and the spectroscopic quadrupole moment $Q_{\text{spec}}(J)$ are defined by using Eq. (4.65) as

$$q_{\text{proton}} := \sqrt{\frac{16\pi}{5}}\, \langle \Phi | \hat{Q}_0^{(2)} | \Phi \rangle\,, \tag{4.67a}$$

$$Q_{\text{spec}}(J) := \sqrt{\frac{16\pi}{5}}\, \langle JJ | \hat{Q}_0^{(2)} | JJ \rangle\,, \tag{4.67b}$$

in the unit of $e\,\text{fm}^2$. [9]

The reduced transition probability in Eq. (4.61) and the spectroscopic quadrupole moment in Eq. (4.67b) are calculated in the AMP by using Eq. (B.8) for the axially-

[9] The spectroscopic quadrupole moment could be measurable in experiments.

symmetric intrinsic state $|\Phi_0\rangle$ as follows [3, 17]:

$$B(E\lambda; J_i \to J_f)$$
$$= \frac{\left| \sum_{M\mu} \langle J_i \lambda M\mu | (J_i \lambda) J_f 0 \rangle \int_0^{\pi/2} d\beta \sin\beta \, d^{(J_i)}_{M0}(\beta) \, \langle \Phi_0 | \hat{Q}^{(\lambda)}_{\mu} e^{-i\hat{J}_y \beta} | \Phi_0 \rangle \right|^2}{\left(\int_0^{\pi/2} d\beta \sin\beta \, d^{(J_f)}_{00}(\beta) \, \langle \Phi_0 | e^{-i\hat{J}_y \beta} | \Phi_0 \rangle \right) \left(\int_0^{\pi/2} d\beta \sin\beta \, d^{(J_i)}_{00}(\beta) \, \langle \Phi_0 | e^{-i\hat{J}_y \beta} | \Phi_0 \rangle \right)}, \tag{4.68a}$$

$$Q_{\rm spec}(J) = \sqrt{\frac{16\pi}{5}} \, \langle J\lambda J0 | (J\lambda) JJ \rangle \sum_{M\mu} \langle J\lambda M\mu | (J\lambda) J0 \rangle$$
$$\times \frac{\int_0^{\pi/2} d\beta \sin\beta \, d^{(J)}_{M0}(\beta) \, \langle \Phi_0 | \hat{Q}^{(\lambda)}_{\mu} e^{-i\hat{J}_y \beta} | \Phi_0 \rangle}{\int_0^{\pi/2} d\beta \sin\beta \, d^{(J)}_{00}(\beta) \, \langle \Phi_0 | e^{-i\hat{J}_y \beta} | \Phi_0 \rangle}. \tag{4.68b}$$

The reduced transition probability in Eq. (4.68a) is approximated for the well-deformed nuclei [1, 11] as

$$B(E2; J_i \to J_f) \approx \frac{5}{16\pi} \, \langle J_i 200 | (J_i 2) J_f 0 \rangle^2 \, (q_{\rm proton})^2, \tag{4.69}$$

then the Alaga rule [79] is obtained,

$$\frac{B(E2; 4^+ \to 2^+)}{B(E2; 2^+ \to 0^+)} \approx \left(\frac{\langle 4200 | (42) 20 \rangle}{\langle 2200 | (22) 00 \rangle} \right)^2 = \frac{10}{7}. \tag{4.70}$$

In the case of $J_i = 0$ and $J_f = 2$, Eq. (4.69) becomes

$$B(E2; 0^+ \to 2^+) \approx \frac{5}{16\pi} (q_{\rm proton})^2. \tag{4.71}$$

The spectroscopic quadrupole moment in Eq. (4.68b) is similarly approximated as

$$Q_{\rm spec}(J) \approx \langle J2J0 | (J2) JJ \rangle \, \langle J200 | (J2) J0 \rangle \, q_{\rm proton}. \tag{4.72}$$

If $J = \lambda = 2$, Eq. (4.72) becomes

$$Q_{\rm spec}(2^+) \approx \langle 2220 | (22) 22 \rangle \, \langle 2200 | (22) 20 \rangle \, q_{\rm proton} = -\frac{2}{7} \, q_{\rm proton}. \tag{4.73}$$

In this study, the author and H. Nakada have newly implemented the source code of the AMP calculations of the reduced transition probability in Eq. (4.68a) and the spectroscopic quadrupole moment in Eq. (4.68b) by using the GEM for the axial HF and HFB solutions. Since the rotational energy is focused on in this paper, we omit the numerical results of the reduced transition probability and the spectroscopic quadrupole moment by the AMP for the deformed nuclei.

Chapter 5

Nucleonic correlation

In this chapter, we introduced the correlation between nucleons associated with the contributions of the interactions for the rotational energy of nuclei.

5.1 Spatial correlations between nucleons

In this section, nucleonic correlations are introduced, especially the spatial correlations between nucleons associated with the contributions of the interactions to the rotational energy of nuclei.

Since nucleonic interactions have coordinate, spin, and isospin dependence, as explained in Chap. 2, correlations between nucleons also do. As the spatial correlations between nucleons, the pair-distribution function is well known, which is introduced in Appendix G. The value of the pair-distribution function increases by the pair correlations, as explained there. In nuclear physics, the correlation that two neutrons (protons) are spatially close is often called the di-neutron (di-proton) correlation [see, *e.g.*, Ref. [80]].

The expectation value of the two-body delta function will be introduced in Sec. 5.2, which has some connection with the pair-distribution function.

5.2 Two-body delta function

In this section, we introduce the two-body delta function and a connection between the two-body delta function and the pair-distribution function. The two-body delta function $\delta^{(2)}$ is defined as

$$\delta^{(2)} := \sum_{i<j} \delta(\mathbf{r}_{ij}). \tag{5.1}$$

We represent the expectation value of $\hat{\delta}^{(2)}$ in Eq. (5.1) as $\langle\hat{\delta}^{(2)}\rangle$, which is interpreted as the probability of the equal position of two nucleons apart from the normalization. As two nucleons get spatially close to each other, $\langle\hat{\delta}^{(2)}\rangle$ will increase, thus $\langle\hat{\delta}^{(2)}\rangle$ could roughly estimates the degree of the proximity for nucleons. In this paper, we call $\langle\hat{\delta}^{(2)}\rangle$ *degree of proximity*.

We discuss the relation between the degree of proximity $\langle\hat{\delta}^{(2)}\rangle$ and the pair-distribution function $g(\mathbf{r}_1\sigma_1\tau_1, \mathbf{r}_2\sigma_2\tau_2)$ in Eq. (G.3). We have defined the creation (annihilation)

operator for the spinor field as $\psi^\dagger(\mathbf{r}\sigma\tau)$ ($\psi(\mathbf{r}\sigma\tau)$). They satisfy the following fermionic anticommutation relations:

$$\begin{aligned}\{\psi(\mathbf{r}_1\sigma_1\tau_1), \psi^\dagger(\mathbf{r}_2\sigma_2\tau_2)\} &= \delta(\mathbf{r}_1 - \mathbf{r}_2)\delta_{\sigma_1\sigma_2}\delta_{\tau_1\tau_2}, \\ \{\psi(\mathbf{r}_1\sigma_1\tau_1), \psi(\mathbf{r}_2\sigma_2\tau_2)\} &= 0, \\ \{\psi^\dagger(\mathbf{r}_1\sigma_1\tau_1), \psi^\dagger(\mathbf{r}_2\sigma_2\tau_2)\} &= 0.\end{aligned} \tag{5.2}$$

The degree of proximity $\langle\hat{\delta}^{(2)}\rangle$ is approximately regarded as a summation of $g(\mathbf{r}\sigma_1\tau_1, \mathbf{r}\sigma_2\tau_2)$ as follows:

$$\begin{aligned}\langle\hat{\delta}^{(2)}\rangle &= \frac{1}{2}\sum_{\tau_1\cdots\tau_4}\sum_{\sigma_1\cdots\sigma_4}\int d^3r\,\langle\psi^\dagger(\mathbf{r}\sigma_1\tau_1)\psi^\dagger(\mathbf{r}\sigma_2\tau_2)\psi(\mathbf{r}\sigma_4\tau_4)\psi(\mathbf{r}\sigma_3\tau_3)\rangle \\ &\approx \frac{1}{2}\sum_{\tau_1\cdots\tau_4}\sum_{\sigma_1\cdots\sigma_4}\int d^3r\,\delta_{\sigma_1\sigma_3}\delta_{\sigma_2\sigma_4}\delta_{\tau_1\tau_3}\delta_{\tau_2\tau_4}\,\langle\psi^\dagger(\mathbf{r}\sigma_1\tau_1)\psi^\dagger(\mathbf{r}\sigma_2\tau_2)\psi(\mathbf{r}\sigma_4\tau_4)\psi(\mathbf{r}\sigma_3\tau_3)\rangle \\ &= \frac{1}{2}\sum_{\tau_1\tau_2}\sum_{\sigma_1\sigma_2}\int d^3r\,\langle\psi^\dagger(\mathbf{r}\sigma_1\tau_1)\psi^\dagger(\mathbf{r}\sigma_2\tau_2)\psi(\mathbf{r}\sigma_2\tau_2)\psi(\mathbf{r}\sigma_1\tau_1)\rangle \\ &= \frac{1}{2}\sum_{\tau_1\tau_2}\sum_{\sigma_1\sigma_2}\int d^3r\,\langle\hat{\rho}(\mathbf{r}\sigma_1\tau_1)\rangle\,\langle\hat{\rho}(\mathbf{r}\sigma_2\tau_2)\rangle\,g(\mathbf{r}\sigma_1\tau_1, \mathbf{r}\sigma_2\tau_2).\end{aligned} \tag{5.3}$$

The degree of proximity $\langle\hat{\delta}^{(2)}\rangle$ is the summation of the nucleonic correlation at only the same position. On the other hand, the pair-distribution function in Eq. (G.3) considers the nucleonic correlation between the positions $\mathbf{r}_1$ and $\mathbf{r}_2$, ignoring some spin and isospin components.

In this study, the degree of proximity $\langle\hat{\delta}^{(2)}\rangle$ has been calculated by using the AMP in order to understand contributions of the interactions for the rotational energy of nuclei. Since the nucleonic interaction is a short-range force as explained in Chap. 2, $\langle\hat{\delta}^{(2)}\rangle$ for angular-momentum eigenstates could be associated with contributions of the interactions for the rotational energy of nuclei. The numerical results of $\langle\hat{\delta}^{(2)}\rangle$ are shown in Sec. 7.5.

Chapter 6

Implementation of MF and AMP calculation

In this study, we have implemented AMP calculations in Eq. (4.10) for the axial HF, HF+BCS, and HFB solutions using the semi-realistic interaction M3Y-P6 with the GEM [27, 28, 31, 32]. It is the first application of the M3Y-type interactions to the AMP calculations. In this chapter, the method of the numerical calculations is discussed in detail, in concrete, the GEM, the HFB theory, the symmetry of MF, and the AMP calculation, including parallel computings.

6.1 Gaussian expansion method

In this section, the Gaussian expansion method (GEM) [28,81–83] is discussed in detail. The s.p. bases is desired to be applied efficiently for nuclei in the wide range of the nuclear chart for studying nuclei, including unstable nuclei. The harmonic oscillator (H.O.) bases are often used in numerical calculations for studying nuclei, while they cannot efficiently describe the exotic nuclear structure, such as a halo structure of nuclei.

In this study, the GEM has been applied for the MF and the AMP calculations, where the radial part of the s.p. wave function is expanded by the complex-range Gaussian, [1]

$$\varphi_{\nu\ell jm}(\mathbf{r}\sigma) = R_{\nu\ell j}(r)[Y^{(\ell)}(\hat{\mathbf{r}}) \otimes \chi_\sigma]^{(j)}_m, \quad R_{\nu\ell j}(r) := N_{\nu\ell j} r^\ell e^{-\nu r^2}. \tag{6.1}$$

The angular function is the spinor spherical harmonics, where the spherical harmonics $Y^{(\ell)}_{\ell_z}(\hat{\mathbf{r}})$ and the spin wave function $\chi_{\sigma,s_z} := \langle\sigma|\frac{1}{2}\, s_z\rangle$ are coupled. The norm matrix is defined as

$$\langle \nu\, \ell\, j\, m|\nu'\, \ell'\, j'\, m'\rangle =: N^{(\ell j)}_{\nu\nu'}\delta_{\ell\ell'}\delta_{jj'}\delta_{mm'}. \tag{6.2}$$

The norm matrix is hermitian and positive-definite.

The range of the Gaussian function is the complex number, $\nu = \nu_r + i\nu_i$, $\nu_r > 0$. We show the values of the parameters in the GEM as follows:

$$\nu_r = \nu_0 b^{-2n}, \quad \begin{cases} \nu_i = 0, & n = 0, 1, \cdots, 5, \\ \frac{\nu_i}{\nu_r} = \pm\frac{\pi}{2}, & n = 0, 1, 2, \end{cases} \tag{6.3}$$

[1] We have omit the isospin index for simplicity.

with $\nu_0 = (2.40\,\mathrm{fm})^{-1}$ and $b = 1.25$, irrespective of (ℓj). For each (ℓj), 12 bases are employed; six of them have real ν values, and the others do six complex ν values. It is necessary to truncate the orbital angular momentum ℓ in the numerical calculations. We here denote the maximum value of the index ℓ as $\ell_{\max}$. We have used the same $\ell_{\max}$ values both the axial-MF and the AMP calculations, $\ell_{\max} = 7$ for $_{12}$Mg nuclei, $\ell_{\max} = 9$ for $_{40}$Zr nuclei, and $\ell_{\max} = 10$ for $_{60}$Nd or $_{62}$Sm nuclei. The values of $\ell_{\max}$ are discussed with deformation in Refs. [28, 83].

Since by using the Fourier transformation, the radial part of the two-body interactions $f_n^{(\cdot)}(r_{ij})$ in Eq. (2.33) becomes the following separable form:

$$\begin{aligned} \tilde{f}_n^{(\cdot)}(q) &= \int d^3r f_n^{(\cdot)}(r) e^{-i\mathbf{q}\cdot\mathbf{r}}, \\ f_n^{(\cdot)}(r_{ij}) &= \frac{1}{(2\pi)^3} \int d^3q \tilde{f}_n^{(\cdot)}(q) e^{i\mathbf{q}\cdot\mathbf{r}_{ij}} \\ &= \frac{1}{(2\pi)^3} \int d^3q \tilde{f}_n^{(\cdot)}(q) e^{i\mathbf{q}\cdot\mathbf{r}_i} e^{-i\mathbf{q}\cdot\mathbf{r}_j}, \end{aligned} \tag{6.4}$$

the matrix elements for the s.p. bases in Eq. (6.1) can be calculated easily.

The advantages of the GEM in the MF and the AMP calculations are listed [28]:

- Since different ranges of Gaussians are superposed, exponential or oscillatory asymptotic behaviors of the s.p. (or q.p.) wave function can be described efficiently at large r, which depend on the s.p. (or q.p.) energies [81, 82].
- It is relatively easy to compute the matrix elements of various two-body interactions [81], not only the central forces but also the noncentral forces. Interactions can become Eq. (6.4) by another, which helps to ensure the reliability of the code.
- The basis parameters in Eq. (6.3) are independent of nuclides [83]. It is practical to apply a single set of bases to almost the whole range of the nuclear chart, facilitating systematic calculations by storing the two-body matrix elements.
- The Coulomb V_{Coulomb} and the center-of-mass term $H_{\mathrm{c.m.}}$ can be fully included, up to the exchange and the pairing terms [81].
- The advantages of the GEM in the MF calculations are taken over to the AMP calculations. Additionally, the spherical bases enable precise numerical calculations of the AMP relatively easily.

Since the GEM could efficiently describe not only the shell structure but also the deformation of nuclei [81, 83], it is suitable for studying the rotational energy of nuclei. Some details for the AMP calculation with the GEM will be discussed in Sec. 6.4.

6.2 HFB theory for nonorthogonal bases

Since the MF theory is important in nuclear physics, we shall introduce particularly the Hartree-Fock-Bogoliubov (HFB) theory [3, 15, 82], where the shell structure and the

symmetry breaking could be considered simultaneously. Since the nonorthogonal bases have been used in this study [as explained in Sec. 6.1], we present the HFB theory for nonorthogonal bases in this section.

The s.p. base ket is represented by $|k\rangle$, and $\mathsf{N}_{kk'} := \langle k|k'\rangle$ is the norm matrix. [2] For an arbitrary ket $|\psi\rangle = \sum_k v_k |k\rangle$, we get

$$\boldsymbol{v}^\dagger \mathsf{N} \boldsymbol{v} = \langle\psi|\psi\rangle \geq 0, \tag{6.5}$$

where $\boldsymbol{v}^\dagger$ represents the transpose with the complex conjugation of the vector $\boldsymbol{v}$, thus the norm matrix is positive semi-definite. We assume that N is positive definite, then the completeness holds,

$$\sum_{kk'} |k\rangle \left(\mathsf{N}^{-1}\right)_{kk'} \langle k'| = \hat{1}, \tag{6.6}$$

where $\hat{1}$ is the identity operator in the s.p. space. The Fock space is represented by the creation and the annihilation operators with the particle vacuum [3, 84]. We denote the creation (annihilation) operator for the s.p. basis k by $c_k^\dagger$ (c_k). They obey the fermionic anticommutation relations,

$$\{c_k, c_{k'}^\dagger\} = \mathsf{N}_{kk'}, \qquad \{c_k, c_{k'}\} = 0, \qquad \{c_k^\dagger, c_{k'}^\dagger\} = 0. \tag{6.7}$$

The particle vacuum $|0\rangle_c$ is defined by

$$c_k |0\rangle_c = 0, \quad \text{for all} \ \ k, \tag{6.8}$$

which satisfies ${}_c\langle 0|0\rangle_c = 1$. In the following, we consider the Fock space, like $|k\rangle = c_k^\dagger |0\rangle_c$, $|kk'\rangle = c_k^\dagger c_{k'}^\dagger |0\rangle_c$, and so on. The Hamiltonian which consists of the one-body term $\hat{K}$ and the two-body term $\hat{V}$, is represented by the nonorthogonal s.p. bases as follows,

$$\begin{aligned}\hat{H} = & \sum_{k_1 \cdots k_4} \left(\mathsf{N}^{-1}\right)_{k_1 k_2} \langle k_2|\hat{K}|k_4\rangle \left(\mathsf{N}^{-1}\right)_{k_4 k_3} c_{k_1}^\dagger c_{k_3} \\ & + \frac{1}{4} \sum_{k_1 \cdots k_8} \left(\mathsf{N}^{-1}\right)_{k_1 k_2} \left(\mathsf{N}^{-1}\right)_{k_3 k_4} \langle k_2 k_4|\hat{V}|k_6 k_8\rangle_a \left(\mathsf{N}^{-1}\right)_{k_6 k_5} \left(\mathsf{N}^{-1}\right)_{k_8 k_7} c_{k_1}^\dagger c_{k_3}^\dagger c_{k_7} c_{k_5},\end{aligned} \tag{6.9}$$

where the matrix elements of $\hat{V}$ are antisymmetrized.

The generalized Bogoliubov transformation is given as [3]

$$\begin{aligned}\alpha_i^\dagger &:= \sum_{k=1}^{M} \left(c_k^\dagger \mathsf{U}_{ki} + c_k \mathsf{V}_{ki}\right), \\ \alpha_i &:= \sum_{k=1}^{M} \left(c_k \mathsf{U}_{ki}^* + c_k^\dagger \mathsf{V}_{ki}^*\right),\end{aligned} \tag{6.10}$$

[2] The formulation is elaborate and complicated in this section by the nonorthogonal bases with the norm matrix N. The HFB theory for orthogonal bases is obtained by replacing N with the identity matrix. The HFB theory for orthogonal bases is given in Refs. [3, 15].

where M is the number of the bases (even number), the matrices U and V are $M \times M$ square matrices. In the vector and matrix representation, Eq. (6.10) can be expressed as

$$(\boldsymbol{\alpha}^\dagger \quad \boldsymbol{\alpha}) = (\mathbf{c}^\dagger \quad \mathbf{c})\mathsf{W}, \quad \mathsf{W} := \begin{pmatrix} \mathsf{U} & \mathsf{V}^* \\ \mathsf{V} & \mathsf{U}^* \end{pmatrix}, \tag{6.11}$$

where $(\mathbf{c}^\dagger \quad \mathbf{c})$ represents $(c_1^\dagger \cdots c_M^\dagger \, c_1 \cdots c_M)$. Note that the transformation in Eq. (6.11) is a non-unitary transformation, so the matrix W is not unitary. We define a matrix $\mathsf{\Sigma}_x$ as [85]

$$\mathsf{\Sigma}_x := \begin{pmatrix} 0 & 1 \\ 1 & 0 \end{pmatrix}, \tag{6.12}$$

then we get

$$\mathsf{\Sigma}_x \mathsf{W} \mathsf{\Sigma}_x = \mathsf{W}^*. \tag{6.13}$$

In contrast to $c_k^\dagger$ and c_k, $\alpha_i^\dagger$ and α_i obey the usual fermionic canonical anticommutation relations,

$$\{\alpha_i, \alpha_{i'}^\dagger\} = \delta_{ii'}, \qquad \{\alpha_i, \alpha_{i'}\} = 0, \qquad \{\alpha_i^\dagger, \alpha_{i'}^\dagger\} = 0. \tag{6.14}$$

The matrix W satisfies the following equation:

$$\mathsf{W}^\dagger \mathsf{N}' \mathsf{W} = 1, \quad \mathsf{N}' := \begin{pmatrix} \mathsf{N} & 0 \\ 0 & \mathsf{N}^* \end{pmatrix}. \tag{6.15}$$

We get

$$\mathsf{\Sigma}_x \mathsf{N}' \mathsf{\Sigma}_x = \mathsf{N}'^*. \tag{6.16}$$

The HFB vacuum $|\Phi\rangle$ is defined by

$$\alpha_i |\Phi\rangle = 0, \quad \text{for all} \;\; i, \tag{6.17}$$

and satisfies $\langle\Phi|\Phi\rangle = 1$. In concrete, the HFB vacuum $|\Phi\rangle$ is represented as

$$|\Phi\rangle \propto \prod_i \alpha_i \, |0\rangle_c \,, \tag{6.18}$$

where the indices i which satisfies $\mathsf{V}_{ki} = 0$ for all k are excluded from the product. We call the states in the product in Eq. (6.18) *occupied quasi-particle states* and the others *unoccupied quasi-particles states*. The HFB vacuum $|\Phi\rangle$ in Eq. (6.18) is interpreted as the independent particle motion of the occupied quasi-particle states..

It is commented that since N is positive-definite, the Cholesky decomposition $\mathsf{N} = \mathsf{L}\mathsf{L}^\dagger$ exists by using an upper-triangular and a regular $M \times M$ matrix L. Thus, the nonorthogonal s.p. bases can be transformed into orthogonal bases as

$$(\widetilde{\mathbf{c}}^\dagger \quad \widetilde{\mathbf{c}}) = (\mathbf{c}^\dagger \quad \mathbf{c})\mathsf{L}'^{\dagger\,-1}, \quad \mathsf{L}' := \begin{pmatrix} \mathsf{L} & 0 \\ 0 & \mathsf{L}^* \end{pmatrix}. \tag{6.19}$$

By using Eq. (6.15), a matrix $\widetilde{\mathsf{W}}$ which is defined as $\widetilde{\mathsf{W}} := \mathsf{L}'^\dagger \mathsf{W}$ is the unitary matrix.

The Bloch-Messiah theorem [3, 86] is well known in the HFB theory, where the unitary Bogoliubov transformation $\widetilde{\mathsf{W}}$ in Eq. (6.11) is decomposed into three unitary Bogoliubov transformations as

$$\widetilde{\mathsf{W}} = \begin{pmatrix} \mathsf{L}^\dagger\mathsf{D} & \mathsf{0} \\ \mathsf{0} & (\mathsf{L}^\dagger\mathsf{D})^* \end{pmatrix} \begin{pmatrix} \bar{\mathsf{U}} & \bar{\mathsf{V}}^* \\ \bar{\mathsf{V}} & \bar{\mathsf{U}}^* \end{pmatrix} \begin{pmatrix} \mathsf{C} & \mathsf{0} \\ \mathsf{0} & \mathsf{C}^* \end{pmatrix}, \tag{6.20}$$

thus,

$$\mathsf{W} = \begin{pmatrix} \mathsf{D} & \mathsf{0} \\ \mathsf{0} & \mathsf{D}^* \end{pmatrix} \begin{pmatrix} \bar{\mathsf{U}} & \bar{\mathsf{V}}^* \\ \bar{\mathsf{V}} & \bar{\mathsf{U}}^* \end{pmatrix} \begin{pmatrix} \mathsf{C} & \mathsf{0} \\ \mathsf{0} & \mathsf{C}^* \end{pmatrix}. \tag{6.21}$$

The matrices $\bar{\mathsf{U}}$ and $\bar{\mathsf{V}}$ form

$$\bar{\mathsf{U}} = \begin{pmatrix} \mathsf{U}^{(1)} & & & \mathsf{0} \\ & \mathsf{U}^{(2)} & & \\ & & \ddots & \\ \mathsf{0} & & & \mathsf{U}^{(\mathsf{M}/2)} \end{pmatrix}, \quad \bar{\mathsf{V}} = \begin{pmatrix} \mathsf{V}^{(1)} & & & \mathsf{0} \\ & \mathsf{V}^{(2)} & & \\ & & \ddots & \\ \mathsf{0} & & & \mathsf{V}^{(\mathsf{M}/2)} \end{pmatrix}, \tag{6.22}$$

where the 2×2 block matrices $\mathsf{U}^{(\mathsf{i})}$ and $\mathsf{V}^{(\mathsf{i})}$ are defined as

$$\mathsf{U}^{(\mathsf{i})} := \begin{pmatrix} u_i & 0 \\ 0 & u_{\bar{i}} \end{pmatrix}, \quad \mathsf{V}^{(\mathsf{i})} := \begin{pmatrix} 0 & v_i \\ v_{\bar{i}} & 0 \end{pmatrix}. \tag{6.23}$$

Since the fermion has a half-integer spin, the conjugate state of i (denoted as $\bar{i} := -i$) usually exists. [3] The index $\bar{\bar{i}}$ is identified with i, *e.g.*, $u_{\bar{\bar{i}}} = u_i$, $v_{\bar{\bar{i}}} = v_i$, and $a_{\bar{\bar{i}}} = a_i$. We define *canonical basis* $a_i^\dagger$ and a_i as

$$(\boldsymbol{a}^\dagger \quad \boldsymbol{a}) := (\mathbf{c}^\dagger \quad \mathbf{c}) \begin{pmatrix} \mathsf{D} & \mathsf{0} \\ \mathsf{0} & \mathsf{D}^* \end{pmatrix}. \tag{6.24}$$

The canonical basis obeys the fermionic canonical anticommutation relations,

$$\{a_i, a_{i'}^\dagger\} = \delta_{ii'}, \qquad \{a_i, a_{i'}\} = 0, \qquad \{a_i^\dagger, a_{i'}^\dagger\} = 0. \tag{6.25}$$

According to Eqs. (6.7), (6.19), and (6.25), $\mathsf{L}^\dagger\mathsf{D}$ becomes the unitary matrix.

We define the q.p. states by using the matrices $\bar{\mathsf{U}}$ and $\bar{\mathsf{V}}$ as

$$\begin{aligned} \tilde{\alpha}_i^\dagger &:= u_i\, a_i^\dagger + v_{\bar{i}}\, a_{\bar{i}}, \\ \tilde{\alpha}_{\bar{i}}^\dagger &:= u_{\bar{i}}\, a_{\bar{i}}^\dagger + v_i\, a_i. \end{aligned} \tag{6.26}$$

The q.p. states $\tilde{\alpha}_i^\dagger$ and $\tilde{\alpha}_i$ obey the the fermionic canonical anticommutation relations,

$$\{\tilde{\alpha}_i, \tilde{\alpha}_{i'}^\dagger\} = \delta_{ii'}, \qquad \{\tilde{\alpha}_i, \tilde{\alpha}_{i'}\} = 0, \qquad \{\tilde{\alpha}_i^\dagger, \tilde{\alpha}_{i'}^\dagger\} = 0. \tag{6.27}$$

By using Eqs. (6.25) and (6.27), the matrix $\begin{pmatrix} \bar{\mathsf{U}} & \bar{\mathsf{V}}^* \\ \bar{\mathsf{V}} & \bar{\mathsf{U}}^* \end{pmatrix}$ becomes unitary with

$$\begin{aligned} |u_i|^2 + |v_{\bar{i}}|^2 = |u_{\bar{i}}|^2 + |v_i|^2 = 1, \\ u_i\, v_i + u_{\bar{i}}\, v_{\bar{i}} = 0, \\ u_i\, u_{\bar{i}}^* - v_{\bar{i}}\, v_i^* = 1. \end{aligned} \tag{6.28}$$

[3] If $|\bar{i}\rangle$ represents the time-reversed state of $|i\rangle$, $\langle i|\bar{i}\rangle = 0$. Thus, $|\bar{i}\rangle$ is often taken as the time-reversed state of $|i\rangle$ except a phase factor.

[4] The transformation by the matrix C is represented as

$$(\boldsymbol{\alpha}^\dagger \quad \boldsymbol{\alpha}) = (\tilde{\boldsymbol{\alpha}}^\dagger \quad \tilde{\boldsymbol{\alpha}}) \begin{pmatrix} \mathsf{C} & 0 \\ 0 & \mathsf{C}^* \end{pmatrix}. \tag{6.29}$$

By using Eqs. (6.14) and (6.27), the matrix C becomes unitary. The vacuum $|0\rangle_c$ is invariant for the D transformation except for an overall constant value. The vacuum $|0\rangle_c$ is transformed into the vacuum $|\Phi\rangle$ via the matrices $\bar{\mathsf{U}}$ and $\bar{\mathsf{V}}$. The unitary matrix C does not mix the occupied and unoccupied q.p. states and has the following block structure,

$$\mathsf{C} = \begin{pmatrix} \mathsf{C}_{\rm occ} & 0 \\ 0 & \mathsf{C}_{\rm unocc} \end{pmatrix}. \tag{6.30}$$

The HFB vacuum $|\Phi\rangle$ in Eqs. (6.17) and (6.18) is invariant for the C transformation except $\det(\mathsf{C}_{\rm occ})$.

According to the Wick's theorem [3, 84],

$$\begin{aligned} &\langle\Phi|c^\dagger_{k_1}c^\dagger_{k_3}c_{k_7}c_{k_5}|\Phi\rangle \\ &= \langle\Phi|c^\dagger_{k_1}c_{k_5}|\Phi\rangle\ \langle\Phi|c^\dagger_{k_3}c_{k_7}|\Phi\rangle - \langle\Phi|c^\dagger_{k_1}c_{k_7}|\Phi\rangle\ \langle\Phi|c^\dagger_{k_3}c_{k_5}|\Phi\rangle + \langle\Phi|c^\dagger_{k_1}c^\dagger_{k_3}|\Phi\rangle\ \langle\Phi|c_{k_7}c_{k_5}|\Phi\rangle\,, \end{aligned} \tag{6.31}$$

and Eq. (6.9), we get the following equation:

$$\langle\Phi|\hat{H}|\Phi\rangle = \sum_{k_1k_2}\langle k_2|\hat{K}|k_1\rangle\,\rho_{k_1k_2} + \frac{1}{4}\sum_{k_1k_2k_3k_4}\langle k_3k_4|\hat{V}|k_1k_2\rangle_a\left(2\rho_{k_1k_3}\rho_{k_2k_4} + \kappa_{k_1k_2}\kappa^*_{k_3k_4}\right), \tag{6.32}$$

where we have defined the density matrix ρ and the pairing tensor κ,

$$(\mathsf{N}\rho\mathsf{N})_{kk'} := \langle\Phi|c^\dagger_{k'}c_k|\Phi\rangle\,, \tag{6.33a}$$

$$(\mathsf{N}\kappa\mathsf{N}^*)_{kk'} := \langle\Phi|c_{k'}c_k|\Phi\rangle\,. \tag{6.33b}$$

The matrices ρ and κ in Eq. (6.33) can be expressed as [3]

$$\rho = \mathsf{V}^*\mathsf{V}^{\rm T}, \quad \kappa = \mathsf{V}^*\mathsf{U}^{\rm T}. \tag{6.34}$$

Since the HFB vacuum $|\Phi\rangle$ is not the eigenstate of the number operator $\hat{N} := \sum_k \hat{1}_k$ [84], we introduce the Lagrange multiplier μ and consider the constraint condition that the expectation value of $\hat{N}$ for $|\Phi\rangle$ is the particle number n, *i.e.*, $\langle\Phi|\hat{N}|\Phi\rangle = n$. [5] Thus, Hamiltonian is replaced in $\hat{H}' := \hat{H} - \mu(\hat{N} - n)$. We define a $2M \times 2M$ matrix R as

$$\mathsf{R} := \begin{pmatrix} \rho & \kappa \\ -\kappa^* & (\mathsf{N}^{-1} - \rho)^* \end{pmatrix}. \tag{6.35}$$

According to $\mathsf{N}^\dagger = \mathsf{N}$, $\rho^\dagger = \rho$, and $\kappa^{\rm T} = -\kappa$, the matrix R is hermitian. Equation (6.17) corresponds one-to-one with

$$(\mathsf{RN}')^2 = \mathsf{RN}', \tag{6.36}$$

[4] The BCS phase is a well-known phase convention, $u_i = u_{\bar{i}} > 0$ and $v_{\bar{i}} = -v_i < 0$ [3].

[5] We here consider only the case of one identical particle for simplicity. In this study, the constraint condition for multi particles (protons and neutrons) are considered as will be mentioned in Sec. 6.3.

except an uncertainty of the C transformation in Eq. (6.21). [6] Considering Eq. (6.36) as the constraint condition, we introduce the following $2M \times 2M$ hermitian matrix $\mathsf{\Lambda}$ as

$$\mathsf{\Lambda} := \begin{pmatrix} \mathsf{\Lambda}_{11} & \mathsf{\Lambda}_{12} \\ \mathsf{\Lambda}_{21} & \mathsf{\Lambda}_{22} \end{pmatrix}, \tag{6.37}$$

whose elements are the Lagrange multiplier.

We consider the first variation for Eq. (6.32) with above constraint conditions by the independent variables ρ, κ, μ, and $\mathsf{\Lambda}$,

$$\delta \left(\langle \Phi | \hat{H}' | \Phi \rangle - \mathrm{tr} \left\{ \mathsf{\Lambda} \left[(\mathsf{RN}')^2 - \mathsf{RN}' \right] \right\} \right) = 0. \tag{6.38}$$

Considering the independent constraint conditions in Eq. (6.37), we get $\mathsf{\Lambda}_{11} = \mathsf{\Lambda}_{22}{}^*$ and $\mathsf{\Lambda}_{12} = \mathsf{\Lambda}_{21}{}^*$, i.e.,

$$\mathsf{\Sigma}_x \mathsf{\Lambda} \mathsf{\Sigma}_x = \mathsf{\Lambda}^*. \tag{6.39}$$

The variation for the matrices is taken for the independent components in the matrix elements. We get

$$\delta \langle \Phi | \hat{H}' | \Phi \rangle = \mathrm{tr}(\mathsf{H}\, \delta \mathsf{R}) - \left[\mathrm{tr}(\mathsf{N}\rho) - n \right] \delta\lambda, \tag{6.40}$$

where we have defined a $2M \times 2M$ matrix H as

$$\mathsf{H} := \begin{pmatrix} \mathsf{h} & \mathsf{\Delta} \\ -\mathsf{\Delta}^* & -\mathsf{h}^* \end{pmatrix}, \tag{6.41}$$

with the HF Hamiltonian matrix h and the pair potential matrix $\mathsf{\Delta}$,

$$\begin{aligned} \mathsf{h}_{kk'} &:= \frac{\delta}{\delta \rho_{kk'}} \langle \Phi | \hat{H}' | \Phi \rangle = \langle \Phi | \{ [c_k, \hat{H}'], c_{k'}^\dagger \} | \Phi \rangle , \\ \mathsf{\Delta}_{kk'} &:= \frac{\delta}{\delta \kappa_{kk'}^*} \langle \Phi | \hat{H}' | \Phi \rangle = \langle \Phi | \{ [c_k, \hat{H}'], c_{k'} \} | \Phi \rangle , \end{aligned} \tag{6.42}$$

and the $2M \times 2M$ matrix $\delta\mathsf{R}$,

$$\delta \mathsf{R} := \begin{pmatrix} \delta\rho & \delta\kappa \\ -\delta\kappa^* & -\delta\rho^* \end{pmatrix}. \tag{6.43}$$

According to $\mathsf{h}^\dagger = \mathsf{h}$ and $\mathsf{\Delta}^{\mathrm{T}} = -\mathsf{\Delta}$, the matrix H is hermitian. The matrix H is called the HFB Hamiltonian matrix. In concrete, Eq. (6.42) becomes

$$\begin{aligned} \mathsf{h}_{kk'} &= \langle k' | \hat{K} | k \rangle + \sum_{k_1 k_2} \langle k' k_2 | \hat{V} | k k_1 \rangle_a \, \rho_{k_1 k_2}, \\ \mathsf{\Delta}_{kk'} &= \frac{1}{2} \sum_{k_1 k_2} \langle k k' | \hat{V} | k_1 k_2 \rangle_a \, \kappa_{k_1 k_2}. \end{aligned} \tag{6.44}$$

From Eqs. (6.38) and (6.40), the following equation is obtained,

$$\begin{aligned} & \mathrm{tr} \left[(\mathsf{H} - \mathsf{N}'\mathsf{R}\mathsf{N}'\mathsf{\Lambda} - \mathsf{N}'\mathsf{\Lambda}\mathsf{R}\mathsf{N}' + \mathsf{N}'\mathsf{\Lambda}) \, \delta \mathsf{R} \right] \\ & - \mathrm{tr} \left\{ \left[(\mathsf{R}\mathsf{N}')^2 - \mathsf{R}\mathsf{N}' \right] \delta \mathsf{\Lambda} \right\} \\ & - \left\{ \mathrm{tr}(\mathsf{N}\rho) - n \right\} \delta\lambda \\ & = 0. \end{aligned} \tag{6.45}$$

[6] See the proof for orthogonal bases in Ref. [86].

As $\delta\mathsf{R}$, $\delta\mathsf{\Lambda}$, and $\delta\lambda$ are arbitrary, the following equations are derived from Eq. (6.45),

$$\mathsf{H} = \mathsf{N}'\mathsf{R}\mathsf{N}'\mathsf{\Lambda} + \mathsf{N}'\mathsf{\Lambda}\mathsf{R}\mathsf{N}' - \mathsf{N}'\mathsf{\Lambda}, \tag{6.46a}$$

$$(\mathsf{R}\mathsf{N}')^2 = \mathsf{R}\mathsf{N}', \tag{6.46b}$$

$$\mathsf{tr}(\mathsf{N}\rho) = n. \tag{6.46c}$$

Equations (6.46a) and (6.46b) lead

$$[\mathsf{N}'^{-1}\mathsf{H}, \mathsf{R}\mathsf{N}'] = 0, \tag{6.47}$$

i.e., $\mathsf{N}'^{-1}\mathsf{H}$ and $\mathsf{R}\mathsf{N}'$ are diagonalizable simultaneously. By using Eqs (6.15) and (6.34), we get

$$\mathsf{W}^{-1}\mathsf{R}\mathsf{N}'\mathsf{W} = \mathsf{W}^\dagger\mathsf{N}'\mathsf{R}\mathsf{N}'\mathsf{W} = \begin{pmatrix} 0 & 0 \\ 0 & 1 \end{pmatrix}. \tag{6.48}$$

The matrix $\mathsf{R}\mathsf{N}'$ is diagonalizable by the matrix W, where the unitary matrix C in Eq. (6.21) is arbitrary. By using Eq. (6.48), we get

$$\begin{aligned} &\mathsf{W}^\dagger\mathsf{H}\mathsf{W} \\ =&\mathsf{W}^\dagger\mathsf{N}'\mathsf{R}\mathsf{N}'\mathsf{\Lambda}\mathsf{W} + \mathsf{W}^\dagger\mathsf{N}'\mathsf{\Lambda}\mathsf{R}\mathsf{N}'\mathsf{W} - \mathsf{W}^\dagger\mathsf{N}'\mathsf{\Lambda}\mathsf{W} \\ =&\begin{pmatrix} 0 & 0 \\ 0 & 1 \end{pmatrix}\mathsf{W}^\dagger\mathsf{N}'\mathsf{\Lambda}\mathsf{W} + \mathsf{W}^\dagger\mathsf{N}'\mathsf{\Lambda}\mathsf{W}\begin{pmatrix} 0 & 0 \\ 0 & 1 \end{pmatrix} - \mathsf{W}^\dagger\mathsf{N}'\mathsf{\Lambda}\mathsf{W}. \end{aligned} \tag{6.49}$$

By using Eqs (6.15) and (6.34), Eq. (6.49) becomes [7]

$$\mathsf{W}^\dagger\mathsf{H}\mathsf{W} = \begin{pmatrix} -\mathsf{A} & 0 \\ 0 & \mathsf{A}^* \end{pmatrix}. \tag{6.50}$$

From Eq. (6.50), the $M \times M$ matrix A is hermitian and diagonalizable by the unitary matrix C in Eq. (6.21). Therefore, the matrix H is diagonalizable by using the matrix W as

$$\mathsf{W}^\dagger\mathsf{H}\mathsf{W} = \begin{pmatrix} \varepsilon & 0 \\ 0 & -\varepsilon \end{pmatrix}, \quad \text{or} \quad \mathsf{H}\mathsf{W} = \mathsf{N}'\mathsf{W}\begin{pmatrix} \varepsilon & 0 \\ 0 & -\varepsilon \end{pmatrix}, \tag{6.51a}$$

$$\varepsilon := \mathrm{diag}(\varepsilon_1, ..., \varepsilon_M), \tag{6.51b}$$

where $\varepsilon_i\,(i = 1, \cdots, M)$ is a non-negative value. Now, the HFB equation for the nonorthogonal bases is derived. Since the matrices h and $\mathsf{\Delta}$ depend ρ and κ, it is necessary to solve Eq. (6.51) self-consistently. This derivation can treat density-dependent interactions. The definition of density is, for example,

$$\rho(\mathbf{r}) := \sum_\tau \sum_\sigma \langle\Phi|\sum_k \delta(\mathbf{r} - \hat{\mathbf{r}}_k)|\Phi\rangle \tag{6.52a}$$

$$= \sum_\tau \sum_\sigma \sum_{k_1 k_2} \rho_{k_1 k_2}\varphi_{k_1}(\mathbf{r}\sigma\tau)\varphi^*_{k_2}(\mathbf{r}\sigma\tau), \tag{6.52b}$$

[7] Although the concrete expression of the matrix A is not used in the following, we can calculate it straightforwardly: $\mathsf{A} = \mathsf{U}^\dagger\mathsf{N}(\mathsf{\Lambda}_{11}\mathsf{U} + \mathsf{\Lambda}_{12}\mathsf{V}) + \mathsf{V}^\dagger\mathsf{N}^*(\mathsf{\Lambda}_{21}\mathsf{U} + \mathsf{\Lambda}_{22}\mathsf{V})$.

where $\varphi_k(\mathbf{r}\sigma\tau) := \langle \mathbf{r}\sigma\tau|k\rangle$, σ and τ are the spin and the isospin indices.

By using the Wick's theorem, the Hamiltonian is expanded around the MF self-consistently. Especially the Hamiltonian is separated into the MF energy and the other terms as

$$\hat{H} = \langle\Phi|\hat{H}|\Phi\rangle + \hat{H}_{\text{otherwise}}. \tag{6.53}$$

For example, Eq. (6.53) for the deformed MF solutions is roughly interpreted as

$$\begin{aligned} \hat{H} &= \langle\Phi_{\text{intrinsic}}|\hat{H}|\Phi_{\text{intrinsic}}\rangle + \hat{H}_{\text{otherwise}} \\ &\sim H_{\text{intrinsic}} + \hat{H}_{\text{rotation}}. \end{aligned} \tag{6.54}$$

The HFB theory includes the HF and the BCS theory as a particular case. If the pair correlations diminish, $\kappa = \mathsf{0}$, and $\Delta = \mathsf{0}$. Then, the HFB equation in Eq. (6.51) becomes the HF equation, and the HFB vacuum $|\Phi\rangle$ does the HF vacuum. The HF vacuum consists of the Slater-determinant of occupied s.p. states,

$$|\Phi\rangle = \prod_{i=1}^{n} a_i^\dagger \left|0\right\rangle_c, \tag{6.55}$$

then it is the eigenstate of the number operator $\hat{N}$, $\hat{N}\,|\Phi\rangle = n\,|\Phi\rangle$. The values of v_i in Eq. (6.23) are 1 for the occupied states and 0 for the unoccupied states. The idempotency in Eq. (6.36) is reduced as

$$(\rho\mathsf{N})^2 = \rho\mathsf{N}. \tag{6.56}$$

The HF vacuum in Eq. (6.55) corresponds one-to-one with Eq. (6.56) except for the C transformation in Eq. (6.21). The Fermi energy is defined as $\varepsilon_{\text{F}} := \max\{-\varepsilon_{\text{i}}\,|\,i = 1, \cdots, n\}$. In the HF theory, the value of the chemical potential μ is not unique but restricted in $\varepsilon_{\text{F}} \leq \mu \leq 0$.

If $\mathsf{D} = \mathsf{0}$ in Eq. (6.21), the HFB equation in Eq. (6.51) becomes the BCS equation, and the HFB vacuum in Eq. (6.17) does the BCS vacuum.

The HF+BCS theory is the approximation of the HFB theory. Strictly speaking, the HF+BCS theory is not the self-consistent theory. [8] There are several methods of the HF+BCS calculation. One method is that the HF equation is self-consistently solved, then the BCS equation is self-consistently solved on the HF vacuum. Another method is that the above procedure is iterated self-consistently, considering feedback on the density matrix ρ with the pair correlations in the HF calculation. The latter method is better than the former by the variational principle. In this study, the former method has been used in order to investigate pairing effects related to only the matrices $\bar{\mathsf{U}}$ and $\bar{\mathsf{V}}$ in Eq. (6.21) on the contributions of the interactions to the pure rotational energy of nuclei, as will be explained in Sec. 7.4.

6.3 Symmetry of MF

In this section, the symmetry of the MF state for even-even nuclei is discussed. The parity and the time-reversal operators are represented as $\hat{\mathcal{P}}$ and $\hat{\mathcal{T}}$, respectively. For

[8] For example, the neutron gas problem [87] is known for nuclei near the neutron drip line.

the sake of simplicity, we say "$\hat{\mathcal{O}}$ symmetry" when $\hat{\mathcal{O}}\,|\Phi_0\rangle = |\Phi_0\rangle$ is satisfied. In the MF calculations, $\hat{\mathcal{P}}$, $\hat{\mathcal{T}}$, $\hat{\mathcal{R}}$ [see Eq. (4.16)], and axial symmetries are assumed,

$$\hat{\mathcal{P}}\,|\Phi_0\rangle = |\Phi_0\rangle\,, \tag{6.57a}$$

$$\hat{\mathcal{T}}\,|\Phi_0\rangle = |\Phi_0\rangle\,, \tag{6.57b}$$

$$\hat{\mathcal{R}}\,|\Phi_0\rangle = |\Phi_0\rangle\,, \tag{6.57c}$$

$$e^{-i\hat{J}_z\alpha}\,|\Phi_0\rangle = |\Phi_0\rangle\,, \quad \text{for any} \quad \alpha \in \mathbb{R}. \tag{6.57d}$$

According to the $\hat{\mathcal{R}}\hat{\mathcal{T}}$ symmetry, the elements of the matrices U and V in Eq. (6.10) which represent the MF solutions are real numbers. The MF state $|\Phi_0\rangle$ is a direct product of the parts having specific isospin and parity,

$$|\Phi_0\rangle = |\Phi_0(p+)\rangle \otimes |\Phi_0(p-)\rangle \otimes |\Phi_0(n+)\rangle \otimes |\Phi_0(n-)\rangle\,. \tag{6.58}$$

The q.p. state in the axial MF is obtained as [9]

$$\alpha^\dagger_{n\pi mt_z} = \sum_\nu \sum_\ell \sum_j \left(c^\dagger_{\nu\ell jmt_z} \mathsf{U}_{\nu\ell jmt_z, n\pi mt_z} + c_{\nu\ell j-mt_z} \mathsf{V}_{\nu\ell j-mt_z, n\pi mt_z} \right), \tag{6.59}$$

where $\pi = (-)^\ell$, $j = \ell \pm 1/2$, and $j \geq |m|$. By using Eq. (6.59), we get

$$[\hat{J}_z, \alpha^\dagger_{n\pi mt_z}] = m\alpha^\dagger_{n\pi mt_z}, \tag{6.60}$$

where the q.p. state has a clear interpretation. The MF state is occupied by both $\alpha_{n\pi mt_z}$ and $\alpha_{n\pi -mt_z}$ as

$$|\Phi_0\rangle \propto \sum_{t_z} \sum_n \sum_\pi \sum_{m>0} \alpha_{n\pi mt_z} \alpha_{n\pi -mt_z}\,|0\rangle_c\,. \tag{6.61}$$

The spherically-symmetric state is represented as

$$\hat{R}(\Omega)\,|\Phi_0\rangle = |\Phi_0\rangle\,, \quad \text{for any} \quad \Omega, \tag{6.62}$$

where $\hat{R}(\Omega)$ is defined in Eq. (B.1). The deformed intrinsic state $|\Phi_0\rangle$ is defined as

$$^\exists\beta \ \text{ such that } \ e^{-i\hat{J}_y\beta}\,|\Phi_0\rangle \not\propto |\Phi_0\rangle\,. \tag{6.63}$$

If the input state has spherical symmetry, the spherical symmetry is conserved for each step of the iteration, then only the spherical solution is obtained. If the input state is deformed, either the spherical or deformed solution is obtained. The deformed solution is obtained that the energy $\langle\Phi_0|\hat{H}|\Phi_0\rangle$ of the deformed solution becomes lower than that of the spherical solution, which is called spontaneous breaking of the rotational symmetry in the MF approximation. Since the Hamiltonian of nuclei is the rotational scalar, we get

$$\langle\Phi_0|e^{i\hat{J}_y\beta}\hat{H}e^{-i\hat{J}_y\beta}|\Phi_0\rangle = \langle\Phi_0|\hat{H}|\Phi_0\rangle\,, \quad \text{for any} \quad \beta. \tag{6.64}$$

Therefore, the states $e^{-i\hat{J}_y\beta}\,|\Phi_0\rangle$ degenerates infinitely for any $\beta \in [0,\pi]$ and could mix easily. The state $e^{-i\hat{J}_y\beta}\,|\Phi_0\rangle$ corresponds to the NG modes in the MF approximation.

[9] Note that $\mathsf{V}_{\nu\ell j-mt_z, n\pi mt_z}$ means $\mathsf{V}_{(\nu,\ell,j,-m,t_z),(n,\pi,m,t_z)}$, and so on.

Since the effective interaction of nuclei often depends on the density of nuclei based on the G-matrix or the DFT, the effective Hamiltonian could not have the rotational symmetry, then Eq. (6.64) might not hold for the deformed solutions. The treatment of the density-dependent interaction in the AMP may be discussed in Sec. 6.5.

We define the Hamiltonian with the following constraint terms for the number as

$$\hat{H}' := \hat{H} - \mu_p(\hat{N}_p - Z) - \mu_n(\hat{N}_n - N), \tag{6.65}$$

where μ_p (μ_n) is the chemical potential for protons (neutrons). We have minimized $\langle\Phi_0|\hat{H}'|\Phi_0\rangle$ with Eq. (6.65) in the HF+BCS and HFB calculations. If the MF state becomes the HF state, it is the eigenstate of the proton and the neutron number operator, respectively. If the MF state has the pair correlations for the proton or the neutron, it is not the eigenstate of the proton or the neutron number operator. The pair correlations for the intrinsic state $|\Phi_0\rangle$ are defined as

$$^{\exists}\phi_\tau \ \text{ such that } \ e^{-i\hat{N}_\tau\phi_\tau} \not\propto |\Phi_0\rangle\,, \quad \tau = p, n, \tag{6.66}$$

where the global-gauge symmetry is broken in the MF approximation. The correlations between protons and neutrons for the pairing tensor κ in Eq. (6.32) are ignored in the HF+BCS and HFB calculations.

6.4 AMP for nonorthogonal bases

In this section, the numerical method of the AMP is discussed. In this work, we apply the PAV for the AMP to the axial HF, HF+BCS, and HFB solutions with the GEM. We have calculated Eq. (4.10) for $\hat{\mathcal{S}} = \hat{H}$, where $\hat{H}$ is the effective Hamiltonian in Eqs. (2.20), (2.32), and (2.33). The intrinsic state could gradually change for increasing J, often accompanied by breaking the axial and the time-reversal symmetry. While these effects can be handled in the cranking model [3, 9, 13] and in the VAP schemes [3], they are ignored in the present study, and we focus on rotational energy arising from a fixed intrinsic state (or pure rotational energy) as stated in the Chap. 1. The number projection is ignored for the HF+BCS and the HFB solutions. We have also calculated Eq. (4.10) for $\hat{\mathcal{S}} = \hat{\delta}^{(2)}$ [$\hat{\delta}^{(2)}$ is defined in Eq. (5.1)].

The numerical method of Eqs. (4.10) and (4.68) has been discussed in Refs. [3,17]. In the following, we present the method of calculating the functions $\langle\Phi_0|e^{-i\hat{J}_y\beta}|\Phi_0\rangle$ and $\mathcal{S}^{01}(\beta)$ for $\hat{\mathcal{S}} = \hat{H}$ connected to the Sec. 6.2, which is characteristic of the nonorthogonal bases. Equation (4.10) for $\hat{\mathcal{S}} = \hat{\delta}^{(2)}$ can be calculated in the same way. The following method can also be used to the AMP calculations of the reduced transition probability in Eq. (4.68a) and the spectroscopic quadrupole moment in Eq. (4.68b), straightforwardly.

The transformation by the rotational operator $\hat{R}(\Omega)$ in Eq. (B.1) for the s.p. bases is represented as [10]

$$\hat{R}(\Omega)(\mathbf{c}^\dagger \quad \mathbf{c})\hat{R}^\dagger(\Omega) = (\mathbf{c}^\dagger \quad \mathbf{c})\mathsf{D}', \quad \mathsf{D}' := \begin{pmatrix} \mathsf{D} & 0 \\ 0 & \mathsf{D}^* \end{pmatrix}. \tag{6.67}$$

[10] The reader may confuse the matrix D in Eq. (6.67) with that in Eq. (6.20). The matrix D in Eq. (6.67) is used only in this section.

We get

$$\mathsf{\Sigma}_x \mathsf{D}' \mathsf{\Sigma}_x = \mathsf{D}'^*. \tag{6.68}$$

In the case of the spherically symmetric s.p. bases $k = (\nu\ell j m t_z)$, as in the GEM of Sec. 6.1, $c_k^\dagger$ is a spherical tensor operator of rank j [3, 67, 74], i.e.,

$$\hat{R}(\Omega) c^\dagger_{\nu\ell j m t_z} \hat{R}^\dagger(\Omega) = \sum_{m'} c^\dagger_{\nu\ell j m' t_z} \mathcal{D}^{(j)}_{m'm}(\Omega), \tag{6.69}$$

where $\mathcal{D}^{(j)}_{m'm}(\Omega)$ is the Wigner D-function in Eq. (B.2), and then the matrix elements of D in Eq. (6.67) are $\mathsf{D}_{kk'} = \delta_{\nu\nu'}\delta_{\ell\ell'}\delta_{jj'}\delta_{t_z t'_z}\mathcal{D}^{(j)}_{mm'}(\Omega)$. We define a matrix T,

$$\hat{R}(\Omega)(\boldsymbol{\alpha}^\dagger \quad \boldsymbol{\alpha})\hat{R}^\dagger(\Omega) = (\boldsymbol{\alpha}^\dagger \quad \boldsymbol{\alpha})\mathsf{T}, \quad \mathsf{T} := \begin{pmatrix} \mathsf{T}_{11} & \mathsf{T}_{12} \\ \mathsf{T}_{21} & \mathsf{T}_{22} \end{pmatrix}, \tag{6.70}$$

which satisfies the relation

$$\mathsf{T} = \mathsf{W}^{-1}\mathsf{D}'\mathsf{W} = \mathsf{W}^\dagger \mathsf{N}' \mathsf{D}' \mathsf{W}. \tag{6.71}$$

By using Eqs. (6.13), (6.16), (6.68), (6.71), and $(\mathsf{\Sigma}_x)^2 = \mathsf{1}$, the following relation is derived,

$$\mathsf{\Sigma}_x \mathsf{T} \mathsf{\Sigma}_x = \mathsf{T}^*, \tag{6.72}$$

i.e., $\mathsf{T}_{22} = \mathsf{T}_{11}{}^*$ and $\mathsf{T}_{21} = \mathsf{T}_{12}{}^*$.

For simplicity, we express

$$|0\rangle := |\Phi\rangle\,, \tag{6.73a}$$

$$|1\rangle := \hat{R}(\Omega)\,|\Phi\rangle\,, \tag{6.73b}$$

and assume that $\langle 0|1\rangle$ does not vanish. According to the generalized Wick's theorem [3, 14],

$$\begin{aligned} &\frac{\langle 0|c^\dagger_{k_1} c^\dagger_{k_3} c_{k_7} c_{k_5}|1\rangle}{\langle 0|1\rangle} \\ =&\frac{\langle 0|c^\dagger_{k_1} c_{k_5}|1\rangle}{\langle 0|1\rangle}\frac{\langle 0|c^\dagger_{k_3} c_{k_7}|1\rangle}{\langle 0|1\rangle} - \frac{\langle 0|c^\dagger_{k_1} c_{k_7}|1\rangle}{\langle 0|1\rangle}\frac{\langle 0|c^\dagger_{k_3} c_{k_5}|1\rangle}{\langle 0|1\rangle} + \frac{\langle 0|c^\dagger_{k_1} c^\dagger_{k_3}|1\rangle}{\langle 0|1\rangle}\frac{\langle 0|c_{k_7} c_{k_5}|1\rangle}{\langle 0|1\rangle}, \end{aligned} \tag{6.74}$$

and Eq. (6.9), we get the equation:

$$\frac{\langle 0|\hat{H}|1\rangle}{\langle 0|1\rangle} = \sum_{k_1 k_2} \langle k_2|\hat{K}|k_1\rangle\, \rho^{01}_{k_1 k_2} + \frac{1}{4}\sum_{k_1 k_2 k_3 k_4} \langle k_3 k_4|\hat{V}|k_1 k_2\rangle_a \left(2\rho^{01}_{k_1 k_3}\rho^{01}_{k_2 k_4} + \kappa^{01}_{k_1 k_2}\kappa^{10*}_{k_3 k_4}\right), \tag{6.75}$$

where we have defined "*generalized density matrix*" ρ^{01}, and "*generalized pairing tensors*" κ^{01} and κ^{10},

$$(\mathsf{N}\rho^{01}\mathsf{N})_{kk'} := \frac{\langle 0|c^\dagger_{k'} c_k|1\rangle}{\langle 0|1\rangle}, \tag{6.76a}$$

$$(\mathsf{N}\kappa^{01}\mathsf{N}^*)_{kk'} := \frac{\langle 0|c_{k'} c_k|1\rangle}{\langle 0|1\rangle}, \tag{6.76b}$$

$$(\mathsf{N}\kappa^{10}\mathsf{N}^*)_{kk'} := \frac{\langle 1|c_{k'} c_k|0\rangle}{\langle 1|0\rangle}. \tag{6.76c}$$

By using the following contraction [14],

$$\begin{aligned}
&\frac{\langle 0|\alpha_i\alpha_{i'}^\dagger|1\rangle}{\langle 0|1\rangle} = \delta_{ii'}, \quad \frac{\langle 0|\alpha_i\alpha_{i'}|1\rangle}{\langle 0|1\rangle} = \mathsf{X}_{i'i}, \\
&\frac{\langle 0|\alpha_i^\dagger\alpha_{i'}|1\rangle}{\langle 0|1\rangle} = 0, \quad \frac{\langle 0|\alpha_i^\dagger\alpha_{i'}^\dagger|1\rangle}{\langle 0|1\rangle} = 0, \\
&\mathsf{X} := \mathsf{T}_{12}{\mathsf{T}_{22}}^{-1} = -\mathsf{X}^{\mathrm{T}},
\end{aligned} \tag{6.77}$$

the matrices ρ^{01}, κ^{01}, and κ^{10} in Eq. (6.76) can be expressed as [3, 14]

$$\begin{aligned}
\rho^{01} &= \widetilde{\mathsf{V}}^*\mathsf{V}^{\mathrm{T}}, \\
\kappa^{01} &= \widetilde{\mathsf{V}}^*\mathsf{U}^{\mathrm{T}}, \\
\kappa^{10} &= \mathsf{V}^*\widetilde{\mathsf{U}}^{\mathrm{T}}
\end{aligned} \tag{6.78}$$

with

$$\begin{aligned}
\widetilde{\mathsf{V}} &:= \mathsf{V} + \mathsf{U}^*\mathsf{X}^*, \\
\widetilde{\mathsf{U}} &:= \mathsf{U} + \mathsf{V}^*\mathsf{X}^*.
\end{aligned} \tag{6.79}$$

The overlap function $\langle 0|1\rangle$ can be calculated by the Onishi formula [3, 12, 14],

$$\langle 0|1\rangle = \langle\Phi|\hat{R}(\Omega)|\Phi\rangle = \sqrt{\det\mathsf{T}_{22}(\Omega)}. \tag{6.80}$$

We here summarize a procedure of the AMP calculation in the PAV scheme. We calculate

1. the matrices U and V by MF calculations,
2. the matrix T via Eq. (6.71),
3. the overlap function $\langle 0|1\rangle$ in Eq. (6.80),
4. the matrices $\widetilde{\mathsf{U}}$ and $\widetilde{\mathsf{V}}$ in Eq. (6.79),
5. the matrices ρ^{01}, κ^{01}, and κ^{10} in Eq. (6.78),
6. $\langle 0|\hat{H}|1\rangle$ / $\langle 0|1\rangle$ via Eq. (6.75), and
7. the integral in Eq. (4.10).

The author and H. Nakada have newly implemented the AMP calculations following the above procedure by using the GEM with the M3Y-type interaction for the axial HF, HF+BCS, and HFB solutions.

6.5 Some problems in AMP calculation

In this section, some problems in the AMP calculation are discussed. The overlap function $\langle\Phi_0|e^{-i\hat{J}_y\beta}|\Phi_0\rangle$ has been calculated by the Onishi formula [3, 12, 14] [see Eq. (6.80)],

$$\langle\Phi_0|e^{-i\hat{J}_y\beta}|\Phi_0\rangle = \sqrt{\det \mathsf{T}_{22}(\beta)}. \tag{6.81}$$

According to the $\hat{\mathcal{T}}$ symmetry, the overlap function is a real number. The sign problem of the Onishi formula is well known, and some solutions have been proposed [88, 89]. In the present cases, the sign problem does not occur owing to non-negativity of the overlap function, as proven for the HF states [39] in Appendix H.

There is also a problem in the density-dependent coefficients in $v_{ij}^{(\mathrm{C}\rho)}$ in the AMP calculations [18, 19, 37]. The density-dependent term in Eq. (2.33) is not a rotational scalar when the density does not have spherical symmetry. In the present calculations, the standard treatment in Ref. [17] has been adopted, replacing the density $\rho(\mathbf{r})$ in Eq. (2.33) with "*generalized density*" $\bar{\rho}(\mathbf{r};\beta)$ which is defined as

$$\bar{\rho}(\mathbf{r};\beta) := \sum_{\tau}\sum_{\sigma}\rho^{01}(\mathbf{r}\sigma\tau;\beta), \tag{6.82a}$$

$$\rho^{01}(\mathbf{r}\sigma\tau;\beta) := \sum_{k_1k_2}\rho^{01}_{k_1k_2}(\beta)\varphi_{k_1}(\mathbf{r}\sigma\tau)\varphi^*_{k_2}(\mathbf{r}\sigma\tau), \tag{6.82b}$$

where $\rho^{01}_{k_1k_2}(\beta)$ is the generalized density matrix in Eq. (6.76a), and $\varphi_k(\mathbf{r}\sigma\tau) := \langle\mathbf{r}\sigma\tau|k\rangle$, σ and τ are the spin and the isospin indices. According to the $\hat{\mathcal{T}}$ symmetry, the generalized density in Eq. (6.82a) becomes a real number. However, there is a case in which $\bar{\rho}(\mathbf{r};\beta)$ becomes negative and its fractional power $\bar{\rho}^{\alpha}(\mathbf{r};\beta)$ may become multivalued. In the M3Y-P6 interaction, the fractional powers α are $\alpha^{(\mathrm{SE})} = 1$ and $\alpha^{(\mathrm{TE})} = 1/3$ [27]. The phase of $\bar{\rho}^{\alpha}(\mathbf{r};\beta)$ has been chosen negative when $\bar{\rho}(\mathbf{r};\beta)$ is negative. Equation (4.13) does not hold for $v_{ij}^{(\mathrm{C}\rho)}[\bar{\rho}(\mathbf{r}_{ij};\beta)]$ as

$$\begin{aligned}
&\frac{d^2}{d\beta^2}\frac{\langle\hat{V}^{(\mathrm{C}\rho)}[\bar{\rho}(\beta)]e^{-\hat{J}_y\beta}\rangle}{\langle e^{-\hat{J}_y\beta}\rangle}\bigg|_{\beta=0} \\
&= -C[\hat{V}^{(\mathrm{C}\rho)}[\rho],\hat{J}_y^2] + 2\left\langle\left(\frac{d}{d\beta}\hat{V}^{(\mathrm{C}\rho)}[\bar{\rho}(\beta)]\right)(-i\hat{J}_y)\right\rangle\bigg|_{\beta=0} + \left\langle\frac{d^2}{d\beta^2}\hat{V}^{(\mathrm{C}\rho)}[\bar{\rho}(\beta)]\right\rangle\bigg|_{\beta=0}.
\end{aligned} \tag{6.83}$$

For a rotational scalar $\hat{\mathcal{S}}$, the following equation should hold:

$$\langle\Phi_0|\hat{\mathcal{S}}|\Phi_0\rangle = \sum_J\langle\Phi_0|\hat{\mathcal{S}}\hat{P}^J_{00}|\Phi_0\rangle = \sum_J(2J+1)\int_0^{\pi/2}d\beta\sin\beta\, d^{(J)}_{00}(\beta)\,\langle\Phi_0|\hat{\mathcal{S}}\,e^{-i\hat{J}_y\beta}|\Phi_0\rangle\,. \tag{6.84}$$

There is no mathematical guarantee that Eq. (6.84) is fulfilled for $\hat{V}^{(\mathrm{C}\rho)}$ when the LHS is evaluated by the MF state, and the RHS is calculated with $\bar{\rho}(\mathbf{r};\beta)$. Nonetheless, in the present calculations, Eq. (6.84) is satisfied for $\hat{V}^{(\mathrm{C}\rho)}$ comparably well to those for the other terms of the Hamiltonian in Eqs. (2.20) and (2.32).

6.6 High-performance computing for AMP calculation

Since the numerical calculation of AMP in Eq. (4.10) takes a lot of time, especially for the finite-range interactions in Eq. (2.33) with the full space, it is necessary to implement high-performance computing, including parallel computing. In this section, high-performance computing for the AMP in Eq. (4.10) are introduced.

The Gauss-Legendre quadrature enables to calculate the definite integral of a function approximately as

$$\int_{-1}^{1} dx f(x) \approx \sum_{i=1}^{n} w_i f(x_i), \tag{6.85}$$

where x_i corresponds with the root of the Legendre polynomials, and the weight w_i depends on x_i and n. We have separated the interval $[0, \pi/2]$ in the integral in Eq. (4.10) into three regions, where the Gauss-Legendre quadrature is applied for each region. We have taken 16 points in the three regions, respectively.

Some calculations of the matrices have been done by using the computational routines in the LAPACK (Linear Algebra PACKage). The LU decomposition of the matrix $\mathsf{T}_{22}(\beta)$ has been done by using DGETRF. Then, the inverse matrix of $\mathsf{T}_{22}(\beta)$ is calculated by using DGETRI. The LU decomposition of the matrix $\mathsf{T}_{22}(\beta)$ enables to calculate $\det \mathsf{T}_{22}(\beta)$ in the real number.

Since the density-dependent interaction in Eq. (2.33) is a local interaction, Eq. (6.75) can be calculated efficiently by using the coordinate space [63]. The matrix elements of the finite-range interactions in Eq. (6.75) for the spherically symmetric s.p. bases in Eq. (6.1) have been calculated once by applying the Wigner-Eckart theorem [1, 73, 81] for a spherical tensor $\hat{T}^{(\lambda)}_{\mu}$, [11]

$$\langle \alpha_2 j_2 m_2 | \hat{T}^{(\lambda)}_{\mu} | \alpha_1 j_1 m_1 \rangle = \langle j_1 \lambda m_1 \mu | (j_1 \lambda) j_2 m_2 \rangle \frac{\langle \alpha_2 j_2 || \hat{T}^{(\lambda)} || \alpha_1 j_1 \rangle}{\sqrt{2j_2 + 1}}, \tag{6.86}$$

where the index α represents other than j and m, and stocked to reuse it. The cash hit is important for the multidimensional arrays in the multiloop there. The hybrid parallel computing by the MPI+OpenMP has been applied. In concrete, $\mathcal{S}^{01}(\beta)$ and $\langle \Phi_0 | e^{-i\hat{J}_y \beta} | \Phi_0 \rangle$ are calculated for each discretized β point by using the MPI (Message Passing Interface) on the distributed-memory-type computing. This parallelization in the AMP calculation is efficient. In Eq. (6.75), the summations for the indices $\nu_1 \cdots \nu_4$ in the spherically symmetric s.p. bases $k = (\nu \ell j m t_z)$ have been calculated by using the OpenMP (Open MultiProcessing) on the shared-memory-type computing.

[11] In the source code of the MF and the AMP, the coefficient $1/\sqrt{2j_2 + 1}$ in Eq. (6.86) is included in the definition of the double-bar matrix elements for simplicity.

Chapter 7

Numerical results

In the present work, the AMP calculations in Eq. (4.10) have been applied to deformed $_{12}$Mg [28, 31], $_{40}$Zr [32], $_{60}$Nd, and $_{62}$Sm isotopes, including stable and unstable nuclei. Important evidence for the deformation is their ratios of excitation energies $E_{\rm x}(4^+)/E_{\rm x}(2^+)$ close to 10/3 [2, 90–92]. $^{24}_{12}$Mg is known as a light stable well-deformed nucleus. $^{34-38}_{12}$Mg are well-deformed unstable nuclei [92]. $^{40}_{12}$Mg is near the neutron drip line [93], and a deformed halo structure of the intrinsic state has been suggested [94]. $^{80}_{40}$Zr is a deformed unstable nucleus near the proton drip line [95]. $^{100-110}_{40}$Zr are neutron-rich well-deformed nuclei [2, 90, 91]. $^{150-154}_{60}$Nd and $^{152-156}_{62}$Sm are well known as deformed nuclei [1, 2, 96].

In this chapter, numerical results of the rotational energy for the fixed intrinsic state (or the pure rotational energy) are shown. The individual terms of the Hamiltonian are separated, then their components of the pure rotational energy are investigated systematically, which depend on the mass number, the deformation, and the pair correlations. In Sec. 7.1, numerical results of the pure rotational energy for the deformed HF solutions are shown, which depend on the mass number and the deformation. In Sec. 7.2, influence of higher-c_{2n} terms and higher-s_{2n} terms in Eq. (4.35) for the deformed HF solutions are investigated numerically based on the revised theory of the AMP with cumulant expansion in Sec. 4.4. The overlap function $\langle\Phi_0|e^{-i\hat{J}_y\beta}|\Phi_0\rangle$ and the function $\mathcal{S}^{01}(\beta)$ for the deformed HF solutions are shown in Sec. 7.3. In Sec. 7.4, numerical results of the pure rotational energy for the HF+BCS and the HFB solutions are shown, where the pairing effects on the pure rotational energy are discussed. In Sec. 7.5, the contributions of the interactions to the pure rotational energy are further investigated with numerical results of the degree of proximity $\langle\hat{\delta}^{(2)}\rangle$ which is defined in Sec. 5.2. In Sec. 7.6, excitation energies $E_{\rm x}(2^+)$ calculated by the AMP in Eq. (4.10) are compared with the rigid-rotor value and experimental values.

7.1 Contribution of individual terms of effective Hamiltonian to rotational energy for fixed HF solutions

In this section, we present composition of rotational energy for the fixed HF solutions. The expectation values of the individual terms of the effective Hamiltonian at angular-

momentum eigenstates are calculated. The following quantity is defined via Eq. (4.10),

$$\mathcal{S}_{\rm x}(J^+) := \langle J^+|\hat{\mathcal{S}}|J^+\rangle - \langle 0^+|\hat{\mathcal{S}}|0^+\rangle\,. \tag{7.1}$$

For $\hat{\mathcal{S}} = \hat{H}$, where $\hat{H}$ is the Hamiltonian, $\mathcal{S}_{\rm x}(J^+)$ corresponds with the excitation energy (i.e., the rotational energy),

$$E_{\rm x}(J^+) = \langle J^+|\hat{H}|J^+\rangle - \langle 0^+|\hat{H}|0^+\rangle\,. \tag{7.2}$$

By taking $\hat{\mathcal{S}}$ to be individual terms of $\hat{H}$, the values $\mathcal{S}_{\rm x}(J^+)$ give their contributions to the rotational energy. In the following, $\hat{\mathcal{S}}$ is an element of the following set,

$$\hat{\mathcal{S}} \in \{\hat{H}, \hat{K}, \hat{V}^{\rm (C)}, \hat{V}^{\rm (LS)}, \hat{V}^{\rm (TN)}, \hat{V}^{\rm (C\rho)}, \hat{V}^{\rm (OPEP)}\}, \tag{7.3}$$

where each ingredient has been defined in Sec. 2.6.

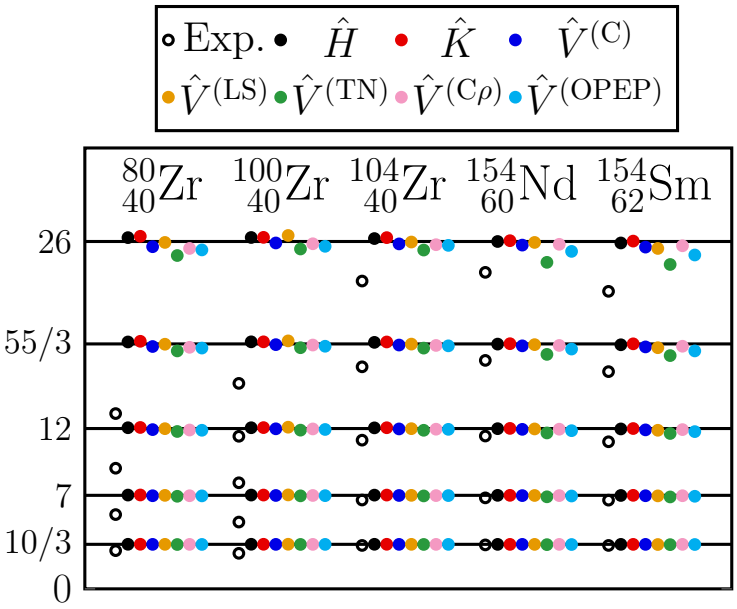

Figure 7.1: The ratios $E_{\rm x}(J^+)/E_{\rm x}(2^+)$ and $\mathcal{S}_{\rm x}(J^+)/\mathcal{S}_{\rm x}(2^+)$ for the deformed $^{80,100,104}_{40}$Zr, $^{154}_{60}$Nd, and $^{154}_{62}$Sm nuclei at their lowest minima. The open circles are the ratios $E_{\rm x}(J^+)/E_{\rm x}(2^+)$ of experiments [2], and the circles filled in black are those obtained by the present work. The ratios $\mathcal{S}_{\rm x}(J^+)/\mathcal{S}_{\rm x}(2^+)$ are also shown for $\hat{\mathcal{S}} = \hat{K}$ (red circles), $\hat{V}^{\rm (C)}$ (blue circles), $\hat{V}^{\rm (LS)}$ (yellow circles), $\hat{V}^{\rm (TN)}$ (green circles), $\hat{V}^{\rm (C\rho)}$ (pink circles), and $\hat{V}^{\rm (OPEP)}$ (sky-blue circles). The rigid-rotor value of $J(J+1)/6$ is presented by the horizontal lines.

The ratios of the individual terms in the effective Hamiltonian $\mathcal{S}_{\rm x}(J^+)/\mathcal{S}_{\rm x}(2^+)$ have been calculated as well as the ratio of the total excitation energy $E_{\rm x}(J^+)/E_{\rm x}(2^+)$. The results for the deformed $_{40}$Zr, $^{154}_{60}$Nd, and $^{154}_{62}$Sm nuclei at their lowest minima are shown in Fig. 7.1. The ratios $E_{\rm x}(4^+)/E_{\rm x}(2^+)$ obtained by the present work are close to those of the experiments and 10/3. The values of $\mathcal{S}_{\rm x}(J^+)$ are negative for $\hat{V}^{\rm (TN)}$ and $\hat{V}^{\rm (C\rho)}$ as will be shown in Fig. 7.3. As well as $E_{\rm x}(J^+)/E_{\rm x}(2^+)$, $\mathcal{S}_{\rm x}(J^+)/\mathcal{S}_{\rm x}(2^+)$ well obeys the $J(J+1)$ rule, up to high angular-momentum $J \approx 12$. The experimental

values gradually get smaller than the $J(J+1)$ line in many nuclei at high J. Additional quantum correlations such as gradual change of the intrinsic state should be considered in order to reproduce experimental values more accurately.

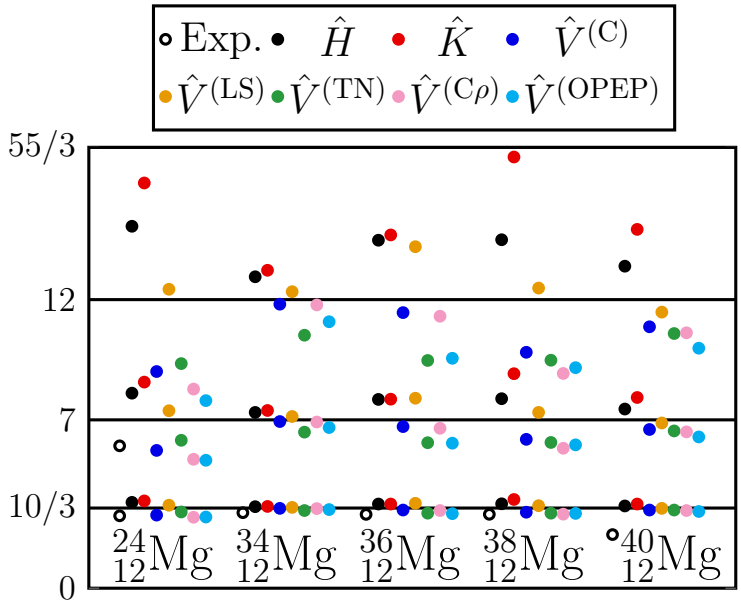

Figure 7.2: The ratios $E_{\mathrm{x}}(J^+)/E_{\mathrm{x}}(2^+)$ and $\mathcal{S}_{\mathrm{x}}(J^+)/\mathcal{S}_{\mathrm{x}}(2^+)$ for the deformed $_{12}$Mg isotopes at their lowest minima. See Fig. 7.1 for conventions. The experimental values of $E_{\mathrm{x}}(J^+)/E_{\mathrm{x}}(2^+)$ are taken from Refs. [2,92,97]. For $^{40}_{12}$Mg, the spin and parity of the observed excited states have not been confirmed yet.

In Fig. 7.2, the ratios $E_{\mathrm{x}}(J^+)/E_{\mathrm{x}}(2^+)$ and $\mathcal{S}_{\mathrm{x}}(J^+)/\mathcal{S}_{\mathrm{x}}(2^+)$ for the deformed $_{12}$Mg isotopes at their lowest minima are shown. Note that for $^{40}_{12}$Mg, the spin and parity of the excited states have not yet been confirmed experimentally. The ratios $E_{\mathrm{x}}(4^+)/E_{\mathrm{x}}(2^+)$ obtained by the present work are close to those of the experiments and 10/3 except for $^{40}_{12}$Mg. The ratios $\mathcal{S}_{\mathrm{x}}(4^+)/\mathcal{S}_{\mathrm{x}}(2^+)$ are also close to 10/3, as well. As J increases, the ratios deviate from the $J(J+1)$ lines.

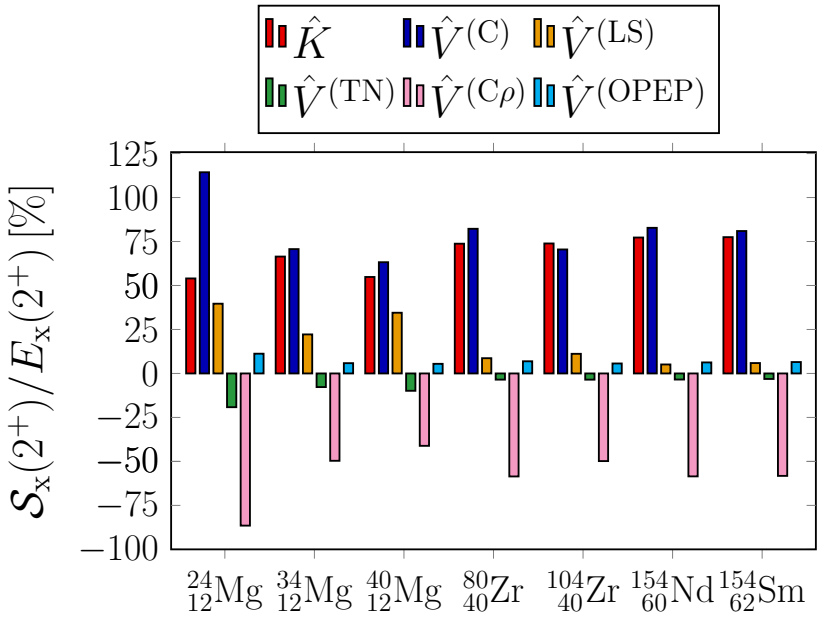

Figure 7.3: The ratios $\mathcal{S}_{\mathrm{x}}(2^+)/E_{\mathrm{x}}(2^+)$ for the deformed nuclei at their lowest minima.

Because the ratios $\mathcal{S}_{\mathrm{x}}(4^+)/\mathcal{S}_{\mathrm{x}}(2^+)$ are close to 10/3 irrespective of $\hat{\mathcal{S}}$ and nuclides in Figs. 7.1 and 7.2, we focus on compositions of the first excitation energies $E_{\mathrm{x}}(2^+)$. Figure 7.3 shows the ratios $\mathcal{S}_{\mathrm{x}}(2^+)/E_{\mathrm{x}}(2^+)$ at their lowest minima, all of which have prolate shapes. Except for the $_{12}$Mg region, these ratios are insensitive to nuclides. The contributions of $\hat{K}$, $\hat{V}^{(\mathrm{C})}$, and $\hat{V}^{(\mathrm{C}\rho)}$ are about 75%, 75%, and −50%, respectively. The large positive contribution of $\hat{K}$ is harmonious with the rotational energy in classical mechanics. Both $\hat{V}^{(\mathrm{C})}$ and $\hat{V}^{(\mathrm{C}\rho)}$ give sizable contributions, although they tend to cancel to a certain extent. The contributions of $\hat{V}^{(\mathrm{LS})}$ and $\hat{V}^{(\mathrm{TN})}$ are small. These noncentral forces mainly contribute near the surface of nuclei. Therefore, these forces become relatively small compared to the central forces when the mass number increases. In the $_{12}$Mg region, the ratios significantly depend on nuclei. The LS force widens the rotational band, and the tensor force narrows it, whose ratios are large compared to those of $^{80,104}_{40}$Zr, $^{154}_{60}$Nd, and $^{154}_{62}$Sm nuclei. Regardless of nuclides, $\hat{V}^{(\mathrm{C})}$ and $\hat{V}^{(\mathrm{LS})}$ act attractively, and $\hat{V}^{(\mathrm{TN})}$ and $\hat{V}^{(\mathrm{C}\rho)}$ do repulsively on the binding energies. The contributions of the former are positive, and those of the latter are negative to the rotational energies. In other words, the attractive forces decrease the moment of inertia of nuclei, and the repulsive forces increase it. The contributions of $\hat{V}^{(\mathrm{OPEP})}$ are about 10 % at most. The contributions of $\hat{V}_{\mathrm{Coulomb}}$ and $\hat{H}_{\mathrm{c.m.}}$ to the excitation energies are no more than a few percent. The latter results indicate that the center-of-mass motion and the rotational motion, both of which are NG modes in the MF approximation, hardly couple each other.

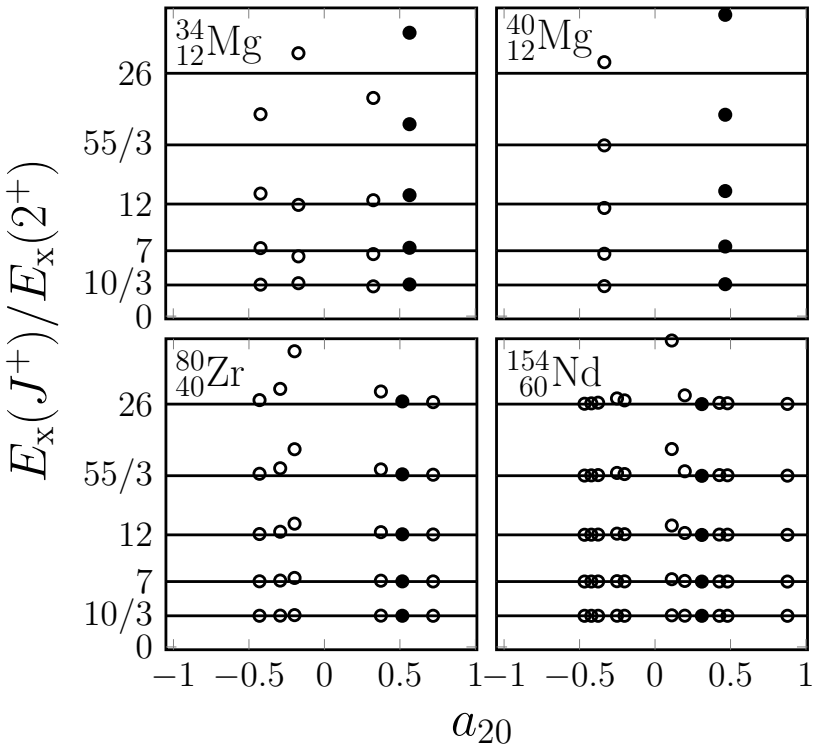

Figure 7.4: The a_{20} (quadrupole deformation parameter) dependence of $E_{\rm x}(J^+)/E_{\rm x}(2^+)$ for the $^{34}_{12}$Mg, $^{40}_{12}$Mg, $^{80}_{40}$Zr, and $^{154}_{60}$Nd nuclei. Their lowest minima are represented by the filled circles. The $J(J+1)/6$ values are presented by the horizontal lines.

We define the quadrupole deformation parameter a_{20} as follows [1, 31],

$$\begin{aligned} a_{20} &:= \frac{q_0}{1.09A^{5/3}}, \\ q_0 &:= \sqrt{\frac{16\pi}{5}}\,\langle\Phi_0|\sum_i r_i'^2\, Y_0^{(2)}(\hat{\mathbf{r}}_i')|\Phi_0\rangle\,, \end{aligned} \tag{7.4}$$

where $\mathbf{r}_i' := \mathbf{r}_i - \mathbf{R}$, $r_i' := |\mathbf{r}_i'|$, $\hat{\mathbf{r}}_i' := \mathbf{r}_i'/r_i'$, $\mathbf{R} := (1/A)\sum_i \mathbf{r}_i$, and q_0 is the mass quadrupole moment of the MF state in units of fm^2 [see also Eq. (A.18)]. Figure 7.4 shows the a_{20} dependence of $E_{\rm x}(J^+)/E_{\rm x}(2^+)$ for axial-HF solutions of the $^{34}_{12}$Mg, $^{40}_{12}$Mg, $^{80}_{40}$Zr, and $^{154}_{60}$Nd nuclei, including their local minima. For low J, the ratios $E_{\rm x}(J^+)/E_{\rm x}(2^+)$ are close to those given by the $J(J+1)$ rule, which indicates that the approximation in Eq. (4.36) is good. For the $^{80}_{40}$Zr and $^{154}_{60}$Nd nuclei, the ratios become closer to the $J(J+1)$ line up to high J as $|a_{20}|$ increases. For the $^{34,40}_{12}$Mg nuclei or the minima having small $|a_{20}|$ values, the ratios get deviating from the $J(J+1)$ line as J increases, though the intrinsic states are fixed. This deviation indicates that the higher-c_{2n} terms are not negligible in Eq. (4.35).

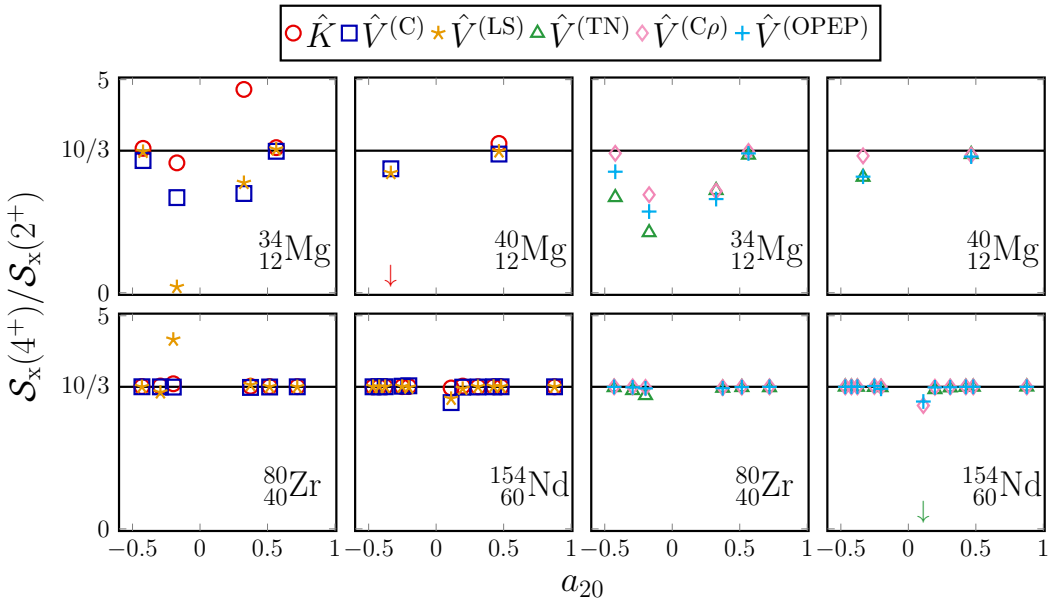

Figure 7.5: The a_{20} dependence of $\mathcal{S}_{\mathrm{x}}(4^+)/\mathcal{S}_{\mathrm{x}}(2^+)$ for $\hat{\mathcal{S}} = \hat{K}$ (red circle), $\hat{V}^{(\mathrm{C})}$ (blue squares), $\hat{V}^{(\mathrm{LS})}$ (yellow stars), $\hat{V}^{(\mathrm{TN})}$ (green triangles), $\hat{V}^{(\mathrm{C}\rho)}$ (pink diamonds), and $\hat{V}^{(\mathrm{OPEP})}$ (sky-blue pluses).

In Fig. 7.5, the a_{20} dependence of $\mathcal{S}_{\mathrm{x}}(4^+)/\mathcal{S}_{\mathrm{x}}(2^+)$ is shown. For $^{80}_{40}$Zr and $^{154}_{60}$Nd, the ratios are close to 10/3, which is almost independent of a_{20} and $\hat{\mathcal{S}}$ with only a few exceptions. For $a_{20} = 0.56$ of $^{34}_{12}$Mg and $a_{20} = 0.47$ of $^{40}_{12}$Mg, the ratios are also close to 10/3, which is independent of $\hat{\mathcal{S}}$. However, at the other minima of $^{34,40}_{12}$Mg, the results strongly depend on a_{20} and $\hat{\mathcal{S}}$.

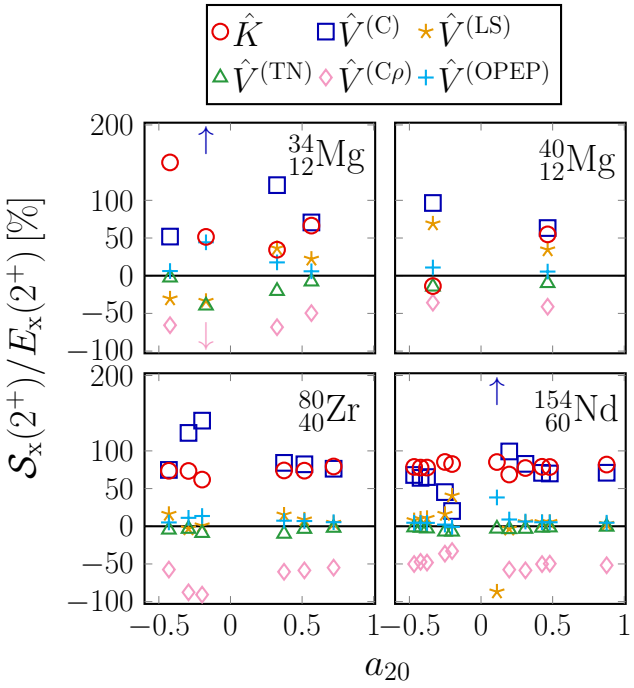

Figure 7.6: The a_{20} dependence of $\mathcal{S}_{\mathrm{x}}(2^+)/E_{\mathrm{x}}(2^+)$.

In Fig. 7.6, the a_{20} dependence of the ratio $\mathcal{S}_{\rm x}(2^+)/E_{\rm x}(2^+)$ is shown. For ${}^{80}_{40}$Zr and ${}^{154}_{60}$Nd, the ratios become almost constant for a_{20}. In particular, the ratios of $\hat{K}$ are almost independent of the deformation parameter. The contributions of $\hat{V}^{(\rm C)}$ and $\hat{V}^{(\rm LS)}$ become positive, and those of $\hat{V}^{(\rm C\rho)}$ and $\hat{V}^{(\rm TN)}$ do negative apart from a few exceptions. The ratios of these interactions fluctuate in the regions where $|a_{20}|$ is not large. For ${}^{34,40}_{12}$Mg nuclei, the ratios strongly depend on the individual MF states. For ${}^{40}_{12}$Mg, we find an extraordinary result that the ratio of $\hat{K}$ is negative at $a_{20} = -0.34$. At this MF state, $J = 2$ gives the lowest value of $\mathcal{S}(J^+)$ for $\hat{\mathcal{S}} = \hat{K}$.

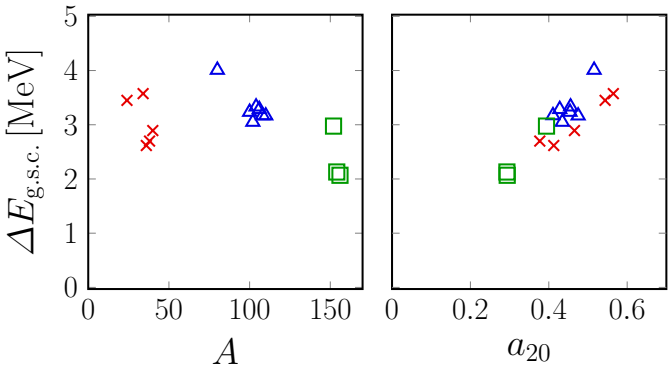

Figure 7.7: The ground-state correlations $\Delta E_{\rm g.s.c.}$ obtained by the AMP calculations for the deformed ${}^{24,34-40}_{12}$Mg (red crosses), ${}^{80,100-110}_{40}$Zr (blue triangles), and ${}^{152-156}_{62}$Sm (green squares) isotopes at their lowest minima. The horizontal axes are the mass number A and the quadrupole deformation parameter a_{20}.

We define the ground-state correlation as follows [see Eq. (4.32)],

$$\Delta E_{\rm g.s.c.} := \langle \Phi_0 | \hat{H} | \Phi_0 \rangle - \langle 0^+ | \hat{H} | 0^+ \rangle \, . \tag{7.5}$$

The values of $\Delta E_{\rm g.s.c.}$ obtained by the AMP calculations for the deformed ${}_{12}$Mg, ${}_{40}$Zr, and ${}_{62}$Sm isotopes at their lowest minima are shown in Fig. 7.7. While $\Delta E_{\rm g.s.c.}$ is not sensitive to the mass number, it correlates well to a_{20} with the correlation coefficient 0.89. Thus, $\Delta E_{\rm g.s.c.}$ increases as deformation of nuclei does, as expected.

7.2 Influence of higher-c_{2n} terms and higher-s_{2n} terms

In this section, we investigate influence of higher-c_{2n} terms and higher-s_{2n} terms in Eq. (4.35) for the fixed HF solutions of ${}^{34}_{12}$Mg, ${}^{40}_{12}$Mg, ${}^{80}_{40}$Zr, and ${}^{154}_{60}$Nd nuclei, including their local minima.

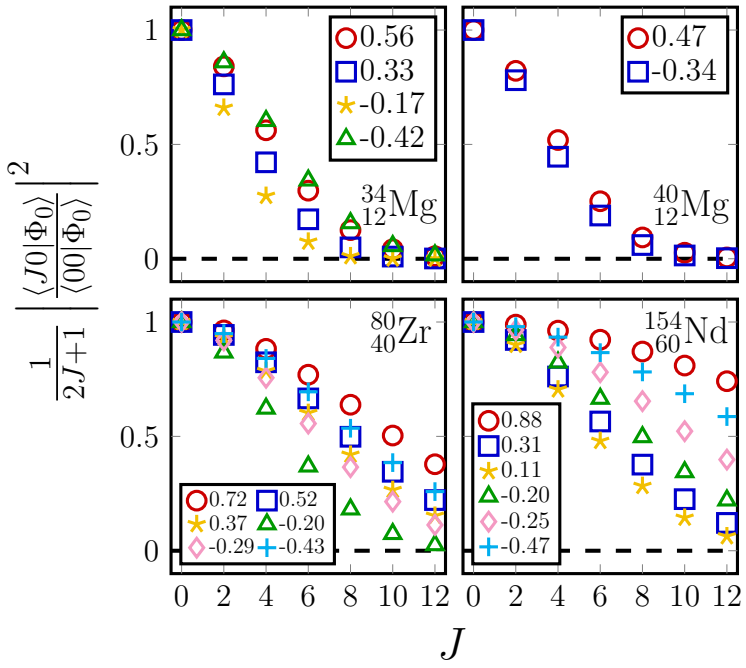

Figure 7.8: The a_{20} dependence of $\frac{1}{2J+1}\left|\frac{\langle J0|\Phi_0\rangle}{\langle 00|\Phi_0\rangle}\right|^2$ in Eq. (4.33) for the $^{34}_{12}$Mg, $^{40}_{12}$Mg, $^{80}_{40}$Zr, and $^{154}_{60}$Nd nuclei. The colored symbols represent the various values of a_{20} as presented in the insets.

We numerically examine the condition of $|\sum_{n=1}^{\infty} c_{2n}\Lambda_{2n}| < 1$ via Eq. (4.33). The a_{20} dependence of $\frac{1}{2J+1}\left|\frac{\langle J0|\Phi_0\rangle}{\langle 00|\Phi_0\rangle}\right|^2$ is shown in Fig. 7.8. As the angular momentum J increases, these values diminish. For the well-deformed minima of $^{80}_{40}$Zr and $^{154}_{60}$Nd, they decrease more slowly than the $^{34,40}_{12}$Mg nuclei or the weakly-deformed minima. The inequality $|\sum_{n=1}^{\infty} c_{2n}\Lambda_{2n}| < 1$ is satisfied for all cases investigated here unless $\langle J0|\Phi_0\rangle = 0$.

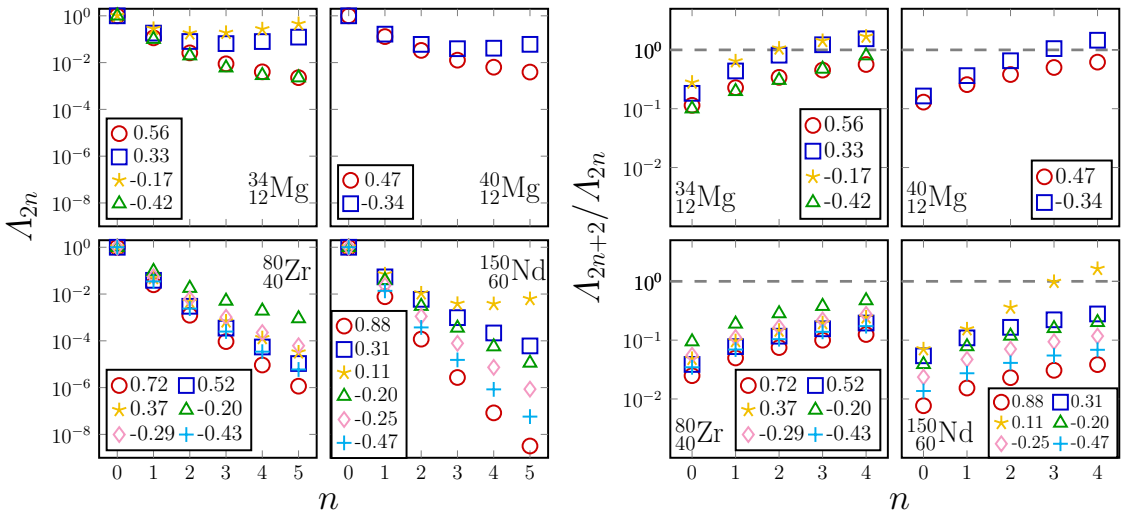

Figure 7.9: The Λ_{2n} and $\Lambda_{2n+2}/\Lambda_{2n}$ values at the various a_{20} values shown in the insets.

It is important for the $J(J+1)$ rule in Eq. (4.36) that the higher-c_{2n} terms are small compared to the c_2 term in Eq. (4.35). To examine influence of the higher-c_{2n} terms and the higher-s_{2n} terms in Eq. (4.35), the Λ_{2n} and $\Lambda_{2n+2}/\Lambda_{2n}$ values are shown in Fig. 7.9. For the well-deformed minima of ${}^{80}_{40}$Zr and ${}^{154}_{60}$Nd, the values of Λ_{2n} are small compared to the ${}^{34,40}_{12}$Mg nuclei or the weakly-deformed minima. As $|a_{20}|$ and the mass number increases, $\Lambda_{2n+2}/\Lambda_{2n}$ decreases for fixed n. Small $\Lambda_{2n+2}/\Lambda_{2n}$ values help both the $J(J+1)$ rule and the approximation of Eq. (4.38), although c_{2n} and s_{2n} also play roles.

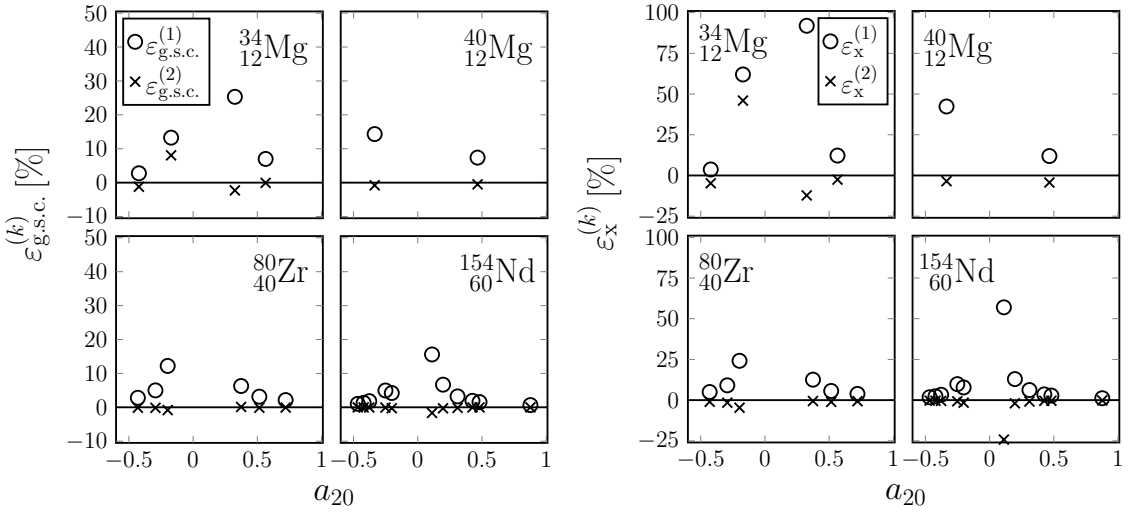

Figure 7.10: The a_{20} dependence of $\varepsilon^{(k)}_{\rm g.s.c.}$ and $\varepsilon^{(k)}_{\rm x}$ for $k=1,2$ in Eq. (7.6).

We next investigate the validity of the approximation in Eq. (4.38). The values of s_2 and s_4 are calculated by using Eq. (4.28a) via numerical differentiation for $\hat{\mathcal{S}}=\hat{H}$. In Fig. 7.10, the a_{20} dependence of the following quantities is shown [see also Eqs. (4.32), (4.37), and (7.5)],

$$\varepsilon^{(k)}_{\rm g.s.c.} := \frac{-\sum_{n=1}^{k} s_{2n}\Lambda_{2n} - \Delta E_{\rm g.s.c.}}{\Delta E_{\rm g.s.c.}}, \tag{7.6a}$$

$$\varepsilon^{(k)}_{\rm x} := \frac{3\sum_{n=1}^{k} s_{2n}\left[-\frac{1}{2}(\Lambda_{2n+2}-\Lambda_{2n}\Lambda_2)\right] - E_{\rm x}(2^+)}{E_{\rm x}(2^+)}, \tag{7.6b}$$

for $k=1,2$. At well-deformed minima of ${}^{80}_{40}$Zr and ${}^{154}_{60}$Nd nuclei, both $\varepsilon^{(1)}_{\rm g.s.c.}$ and $\varepsilon^{(1)}_{\rm x}$ are less than a few percents. However, they are large for ${}^{34,40}_{12}$Mg nuclei or weakly-deformed minima. Regardless of nuclides, $|\varepsilon^{(2)}_{\rm g.s.c.}|$ is smaller than $|\varepsilon^{(1)}_{\rm g.s.c.}|$. Except for $a_{20}=-0.42$ of ${}^{34}_{12}$Mg, $|\varepsilon^{(2)}_{\rm x}|$ is also smaller than $|\varepsilon^{(1)}_{\rm x}|$. The contributions of the s_4 terms to $\Delta E_{\rm g.s.c.}$ and $E_{\rm x}(2^+)$, thereby to the moment of inertia, turn out to be significant for ${}^{34,40}_{12}$Mg nuclei or weakly-deformed minima.

7.3 Angle dependence of overlap function

In this section, the dependence of the overlap functions $\langle\Phi_0|e^{-i\hat{J}_y\beta}|\Phi_0\rangle$ and the functions $\mathcal{S}^{01}(\beta)$ in Eq. (4.12) on the angle β are discussed for further understanding of the numerical results in Secs 7.1 and 7.2, such as the $J(J+1)$ rule and the ratio $\mathcal{S}_{\rm x}(2^+)/E_{\rm x}(2^+)$.

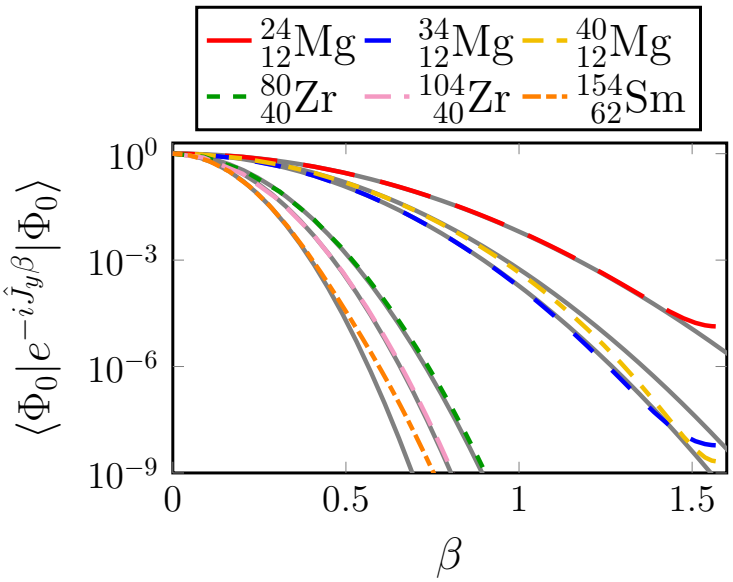

Figure 7.11: The overlap functions $\langle\Phi_0|e^{-i\hat{J}_y\beta}|\Phi_0\rangle$ for the deformed nuclei at their lowest minima. Gray lines are obtained by the Gaussian approximation in Eq. (F.1).

In Fig. 7.11, the overlap functions $\langle\Phi_0|e^{-i\hat{J}_y\beta}|\Phi_0\rangle$ are shown for the deformed nuclei at their lowest minima. The overlap functions for the $^{80}_{40}$Zr and $^{154}_{62}$Sm nuclei have sharper peaks than those for the $^{34,40}_{12}$Mg nuclei. The fluctuation $\sigma[\hat{J}_y]$ is connected to the coefficient of the second derivative of $\langle\Phi_0|e^{-i\hat{J}_y\beta}|\Phi_0\rangle$ at $\beta=0$ via Eq. (4.14). The values of $(\sigma[\hat{J}_y])^2$ for $^{24}_{12}$Mg, $^{34}_{12}$Mg, $^{80}_{40}$Zr, $^{104}_{40}$Zr, and $^{154}_{62}$Sm, which are calculated from $\langle\Phi_0|\hat{\boldsymbol{J}}^2|\Phi_0\rangle$ [see Eq. (4.15b)], are 10.1, 17.2, 51.9, 64.2, and 86.6, respectively. The Gaussian approximation in Eq. (F.1) holds well except at $\beta\approx\pi/2$, although the overlap functions for $_{12}$Mg nuclei have broad peak. Recall that $(\sigma[\hat{J}_y])^{-1}$ is the width of the Gaussian in this approximation.

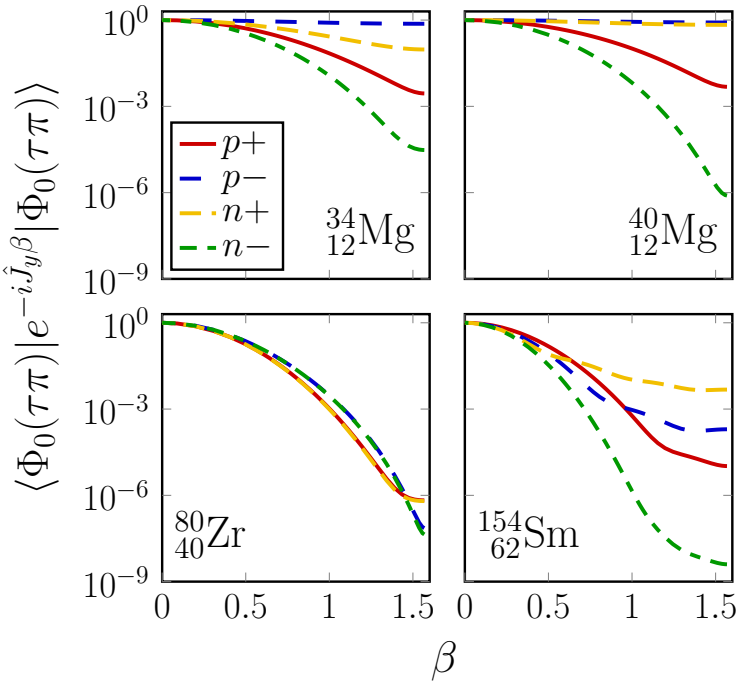

Figure 7.12: $\langle\Phi_0(\tau\pi)|e^{-i\hat{J}_y\beta}|\Phi_0(\tau\pi)\rangle$ ($\tau = p, n, \pi = +, -$) for the deformed $^{34}_{12}$Mg, $^{40}_{12}$Mg, $^{80}_{40}$Zr, and $^{154}_{62}$Sm nuclei at their lowest minima.

In the present AMP calculations, the overlap function $\langle\Phi_0|e^{-i\hat{J}_y\beta}|\Phi_0\rangle$ can be factorized via isospin and parity as Eq. (6.58) because the rotational operator $e^{-i\hat{J}_y\beta}$ does not mix isospin and parity. Figure 7.12 shows the components of the overlap functions $\langle\Phi_0(\tau\pi)|e^{-i\hat{J}_y\beta}|\Phi_0(\tau\pi)\rangle$ ($\tau = p, n$ and $\pi = +, -$), for the deformed $^{34}_{12}$Mg, $^{40}_{12}$Mg, $^{80}_{40}$Zr, and $^{154}_{62}$Sm nuclei at their lowest minima. For the $_{12}$Mg nuclei, some components have almost spherical structure and hardly depend on the β angle. For the $^{40}_{12}$Mg nucleus, the $(n-)$ component is well-deformed, which may be related to the deformed halo with peanut shape [83]. For the $^{80}_{40}$Zr nucleus, all $\tau\pi$ components are similarly deformed. For the $^{154}_{62}$Sm nucleus, the $(n-)$ component is strongly deformed, though the others are not so strongly deformed.

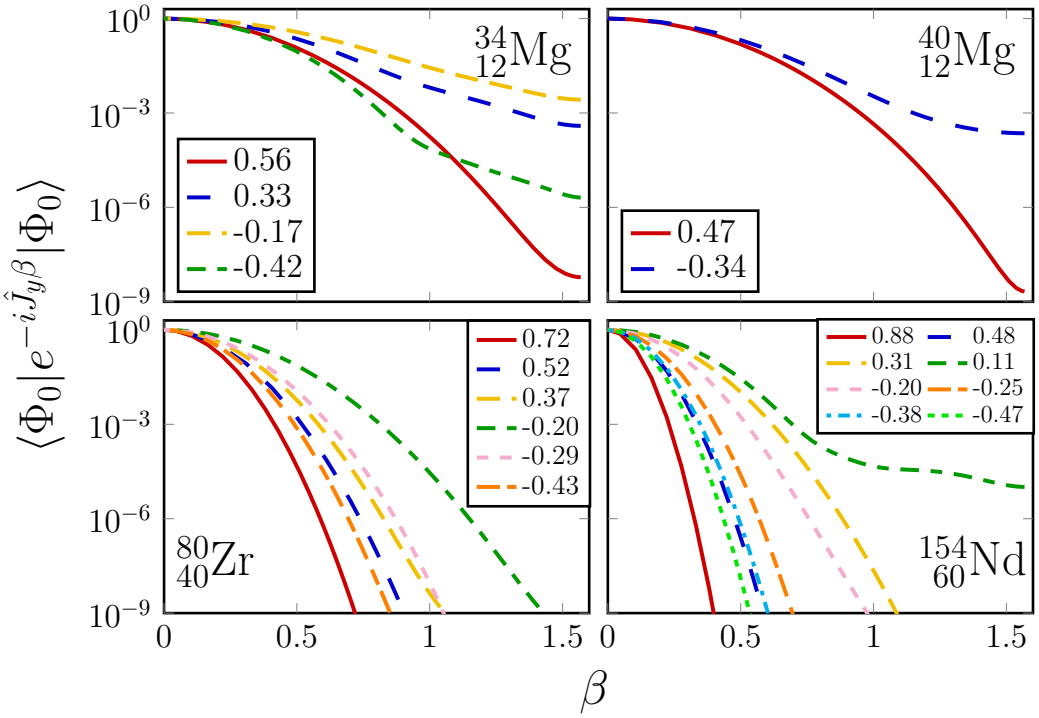

Figure 7.13: The overlap functions $\langle\Phi_0|e^{-i\hat{J}_y\beta}|\Phi_0\rangle$ for the $^{34}_{12}$Mg, $^{40}_{12}$Mg, $^{80}_{40}$Zr, and $^{154}_{60}$Nd nuclei, including their local minima. The individual lines correspond to the various a_{20} values shown in the insets.

Figure 7.13 shows $\langle\Phi_0|e^{-i\hat{J}_y\beta}|\Phi_0\rangle$ for minima of the $^{34}_{12}$Mg, $^{40}_{12}$Mg, $^{80}_{40}$Zr, and $^{154}_{60}$Nd nuclei, including their local minima with various a_{20} values. The overlap functions have sharper peaks near $\beta = 0$ as $|a_{20}|$ increases, irrespective of nuclides . A similar result is obtained in Ref. [18]. The sharpness of the peak near $\beta = 0$ of $\langle\Phi_0|e^{-i\hat{J}_y\beta}|\Phi_0\rangle$ corresponds with the fluctuation $\sigma[\hat{J}_y]$. The large fluctuation takes place when $|a_{20}|$ is large for the heavy nuclei [3], which leads to a sharp peak near $\beta = 0$. The overlap function depends on the mass number as well as on a_{20}. The Gaussian approximation sometimes fails for the $_{12}$Mg nuclei or the weakly-deformed minima. As Λ_{2n} in Eq. (4.30) is determined only by $\langle\Phi_0|e^{-i\hat{J}_y\beta}|\Phi_0\rangle$, it is fair to say that the results in Fig. 7.9 originates from those in Fig. 7.13.

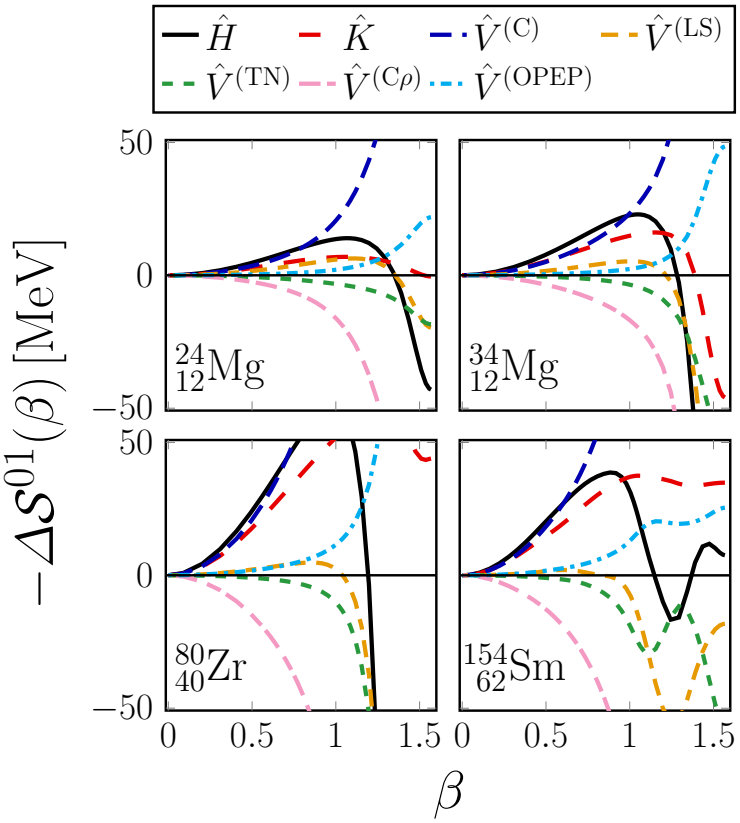

Figure 7.14: The behavior of $-\Delta\mathcal{S}^{01}(\beta)$ for the individual terms of the Hamiltonian for the deformed $^{24}_{12}$Mg, $^{34}_{12}$Mg, $^{80}_{40}$Zr, and $^{154}_{62}$Sm nuclei at their lowest minima.

We show $-\Delta\mathcal{S}^{01}(\beta)$ which is defined by

$$\Delta\mathcal{S}^{01}(\beta) := \mathcal{S}^{01}(\beta) - \mathcal{S}^{01}(\beta = 0), \tag{7.7}$$

for the deformed $^{24}_{12}$Mg, $^{34}_{12}$Mg, $^{80}_{40}$Zr, and $^{154}_{62}$Sm nuclei at their lowest minima in Fig. 7.14. These results are related to those in Fig. 7.3. As in Eq. (4.13), we have

$$-\frac{d^2}{d\beta^2}\Delta\mathcal{S}^{01}(\beta)\Big|_{\beta=0} = C[\hat{\mathcal{S}}, \hat{J}_y^2], \tag{7.8}$$

except the derivative terms for $\hat{V}^{(\mathrm{C}\rho)}$ in (6.83). The values of $C[\hat{\mathcal{S}}, \hat{J}_y^2]$ for $\hat{\mathcal{S}} = \hat{K}$, $\hat{V}^{(\mathrm{C})}$, and $\hat{V}^{(\mathrm{LS})}$ are positive, and those for $\hat{V}^{(\mathrm{TN})}$ and $\hat{V}^{(\mathrm{C}\rho)}$ are negative. As the mass number increases, the values of $|C[\hat{\mathcal{S}}, \hat{J}_y^2]|$ significantly increase except for $\hat{\mathcal{S}} = \hat{V}^{(\mathrm{LS})}$, $\hat{V}^{(\mathrm{TN})}$, and $\hat{V}^{(\mathrm{OPEP})}$. Although they are not shown, $-\Delta\mathcal{S}^{01}(\beta) \approx 0$ and $C[\hat{\mathcal{S}}, \hat{J}_y^2] \approx 0$ for $\hat{V}_{\mathrm{Coulomb}}$ and $\hat{H}_{\mathrm{c.m.}}$, independent of nuclides. The values of $-\Delta\mathcal{S}^{01}(\beta)$ far from $\beta \approx 0$ strongly depend on nuclides, which are influenced by the higher-order terms of the cumulant expansion in Eq. (4.28).

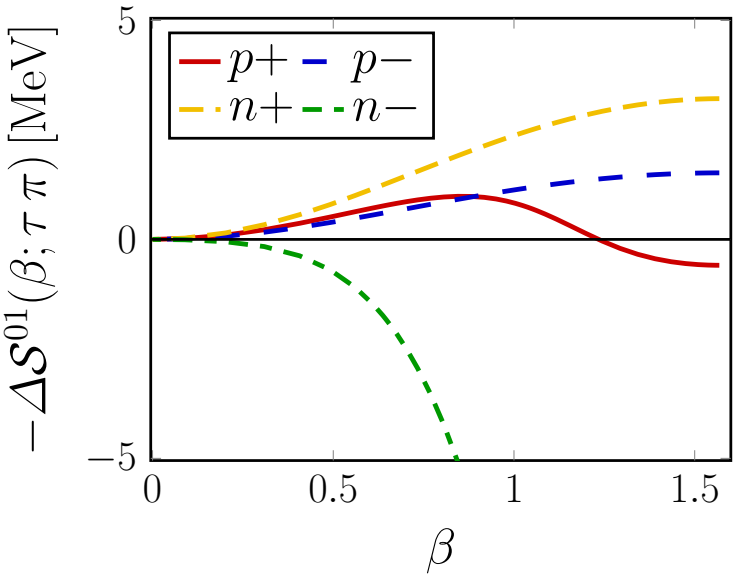

Figure 7.15: The function $-\Delta\mathcal{S}^{01}(\beta;\tau\,\pi)$ in Eq. (7.9) for $\hat{\mathcal{S}} = \hat{K}$ at the oblate minimum of ${}^{40}_{12}$Mg.

In the present work, the values of $C[\hat{\mathcal{S}}, \hat{J}_y^2]$ for $\hat{\mathcal{S}} = \hat{K}$ are almost always positive. However, there exists an exception; the local oblate minimum of ${}^{40}_{12}$Mg. We decompose $-\Delta\mathcal{S}^{01}(\beta)$ for $\hat{K}$ as

$$\mathcal{S}^{01}(\beta;\tau\,\pi) := \frac{\langle\Phi_0(\tau\pi)|\hat{\mathcal{S}}\, e^{-i\hat{J}_y\beta}|\Phi_0(\tau\pi)\rangle}{\langle\Phi_0|e^{-i\hat{J}_y\beta}|\Phi_0\rangle}, \tag{7.9a}$$

$$\Delta\mathcal{S}^{01}(\beta;\tau\,\pi) := \mathcal{S}^{01}(\beta;\tau\,\pi) - \mathcal{S}^{01}(\beta=0;\tau\,\pi), \tag{7.9b}$$

for $\tau = p, n$ and $\pi = +, -$, and show $-\Delta\mathcal{S}^{01}(\beta;\tau\,\pi)$ in Fig. 7.15 for the oblate minimum of ${}^{40}_{12}$Mg. The curvature of $-\Delta\mathcal{S}^{01}(\beta; n-)$ at $\beta \approx 0$ is negative and significant although those for the others are positive and small. This anomalous result is related to the negative contribution of $\hat{K}$ exhibited in Fig. 7.6.

7.4 Pairing effects on rotational energy for fixed MF solutions

In this section, the pairing effects on the pure rotational energy are discussed. First, numerical results of the pure rotational energy for the HF+BCS+AMP calculations are shown, where the pair correlations are considered systematically on the deformed HF solutions. Then, numerical results of the HFB+AMP calculations are shown.

In Eqs. (6.32) and (6.75), we call the interaction energies containing the pairing tensor κ or the generalized pairing tensors κ^{01} and κ^{10} *pairing term*, and the other terms *HF term*, respectively. The pairing term in Eq. (6.32) is often called the pair energy.

For a better understanding of the pairing effects on the pure rotational energy, we devised a method that systematically considers the pair correlations by introducing a

parameter in the HF+BCS energy. First, the axial-HF equation has been solved self-consistently, then the BCS equation has been solved on the deformed HF state. The axial-HF solution corresponds with the matrix D in (6.21), and the pair correlations do with the matrices $\bar{\mathsf{U}}$ and $\bar{\mathsf{V}}$ in (6.21). We introduce a parameter g multiplying the pair energy in Eq. (6.32) as

$$\begin{aligned}&\langle\Phi(g)|\hat{H}|\Phi(g)\rangle \\ &= \sum_{k_1k_2} \langle k_2|\hat{K}|k_1\rangle\, \rho_{k_1k_2} + \frac{1}{4}\sum_{k_1k_2k_3k_4} \langle k_3k_4|\hat{V}|k_1k_2\rangle_a \left(2\rho_{k_1k_3}\rho_{k_2k_4} + g\kappa_{k_1k_2}\kappa^*_{k_3k_4}\right).\end{aligned} \tag{7.10}$$

The state $|\Phi(g=0)\rangle$ corresponds with the HF states, and the state $|\Phi(g=1)\rangle$ does with the "natural" HF+BCS states. The matrices $\bar{\mathsf{U}}$ and $\bar{\mathsf{V}}$ in (6.21) depend on the parameter g. We have solved self-consistently the BCS equation using Eq. (7.10) on the deformed HF solutions at their lowest minima. The rotational energies for the HF+BCS solutions have been calculated by using the AMP, where the pairing terms in Eq. (6.75) are multiplied by corresponding g values.

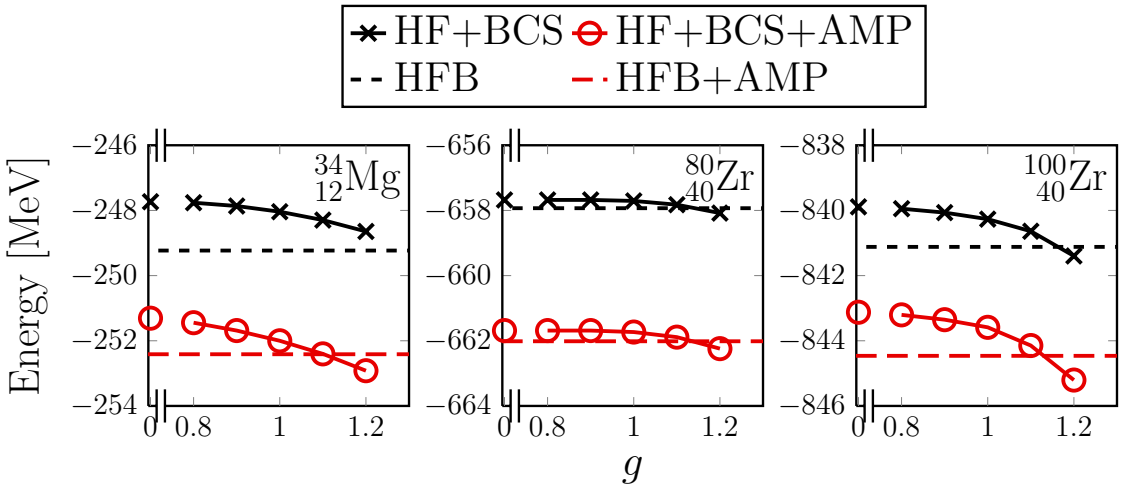

Figure 7.16: The g dependence of the MF and the projected energies for the deformed HF+BCS solutions of $^{34}_{12}$Mg and $^{80,100}_{40}$Zr. The black crosses represent the MF energy for the HF+BCS solutions, and the red circles do the values of $E(0^+)$ obtained by the HF+BCS+AMP calculations. The black dashed lines represent the HFB energy at their lowest minima, and the red dashed lines do the values of $E(0^+)$ obtained by the HFB+AMP calculations.

In Fig. 7.16, the g dependence of the MF and the projected energies are shown for the deformed HF+BCS solutions of $^{34}_{12}$Mg and $^{80,100}_{40}$Zr. The MF and projected energies for the HFB minima are also shown. The values of the projected energies are $\langle 0^+|H'|0^+\rangle$, including the chemical-potential terms in Eq. (6.65). We call the g value where the pair correlations arise *critical point*. As g increases, both the MF and the projected energies decrease from the HF energies from the critical points. Irrespective of the MF or the projected energies, the energies for the HFB solutions are close to those for the HF+BCS ones in the region between $g = 1.1$ and 1.2.

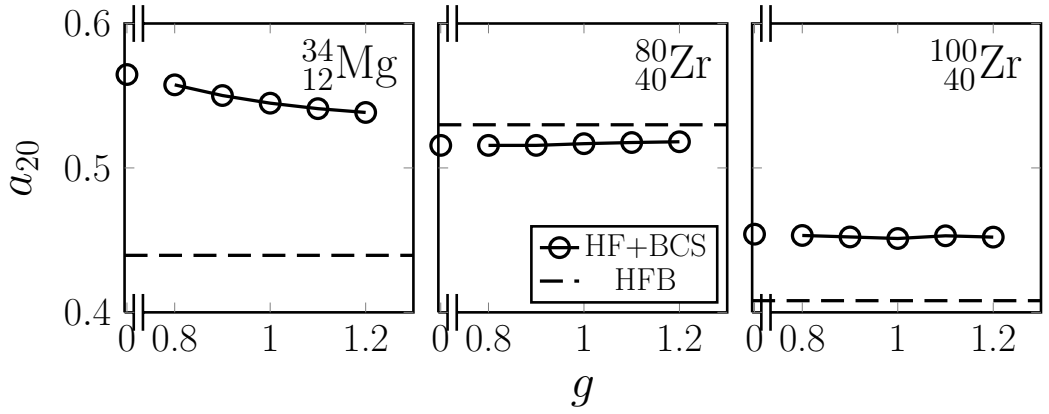

Figure 7.17: The g dependence of a_{20} in Eq. (7.4). The dashed lines represent the values of a_{20} for the HFB minima.

The g dependence of the deformation parameter a_{20} is shown for the deformed $^{34}_{12}$Mg and $^{80,100}_{40}$Zr nuclei in Fig. 7.17. The values of a_{20} for the HFB minima are also shown. The values of a_{20} is insensitive to g for the $^{80,100}_{40}$Zr nuclei. On the other hand, the values of a_{20} decrease for the $^{34}_{12}$Mg nucleus. The values of a_{20} for the HF+BCS solutions are close to that of the HFB solution for the $^{80}_{40}$Zr nucleus, while there are differences between them for the $^{34}_{12}$Mg and $^{100}_{40}$Zr nuclei. The reason for the difference is that the matrix D in Eq. (6.21) of the HFB solution is different from that of the HF+BCS solution.

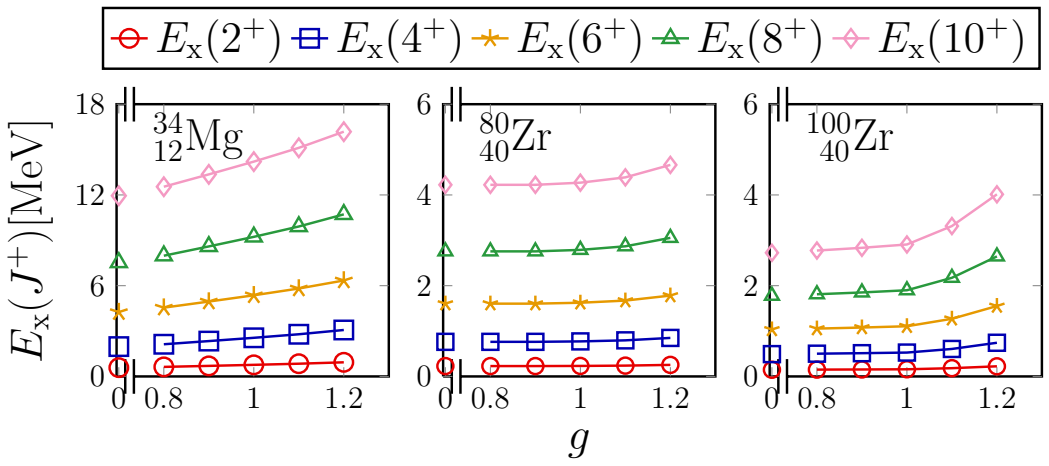

Figure 7.18: The g dependence of $E_{\rm x}(J^+)$.

Figure 7.18 shows the g dependence of the excitation energies $E_{\rm x}(J^+)$ for the deformed $^{34}_{12}$Mg and $^{80,100}_{40}$Zr nuclei. As g increases, the excitation energies do from the critical points.

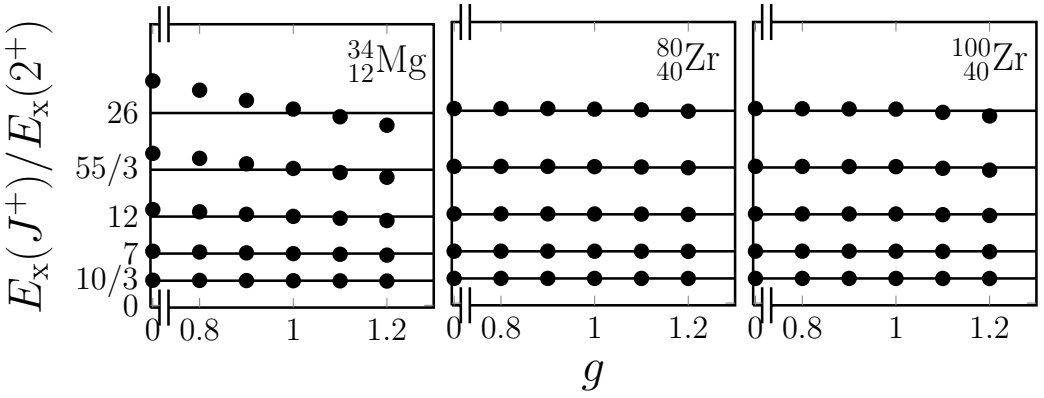

Figure 7.19: The g dependence of the ratios $E_x(J^+)/E_x(2^+)$.

The g dependence of the ratios $E_x(J^+)/E_x(2^+)$ is shown for the deformed $^{34}_{12}$Mg and $^{80,100}_{40}$Zr nuclei in Fig. 7.19. The ratios $E_x(J^+)/E_x(2^+)$ are insensitive to g and close to the $J(J+1)$ lines up to $J = 12$ for the $^{80,100}_{40}$Zr nuclei. As g increases, the ratios $E_x(J^+)/E_x(2^+)$ decrease for $J \geq 8$ for the $^{34}_{12}$Mg nucleus though the excitation energies $E_x(J^+)$ increase in Fig. 7.18.

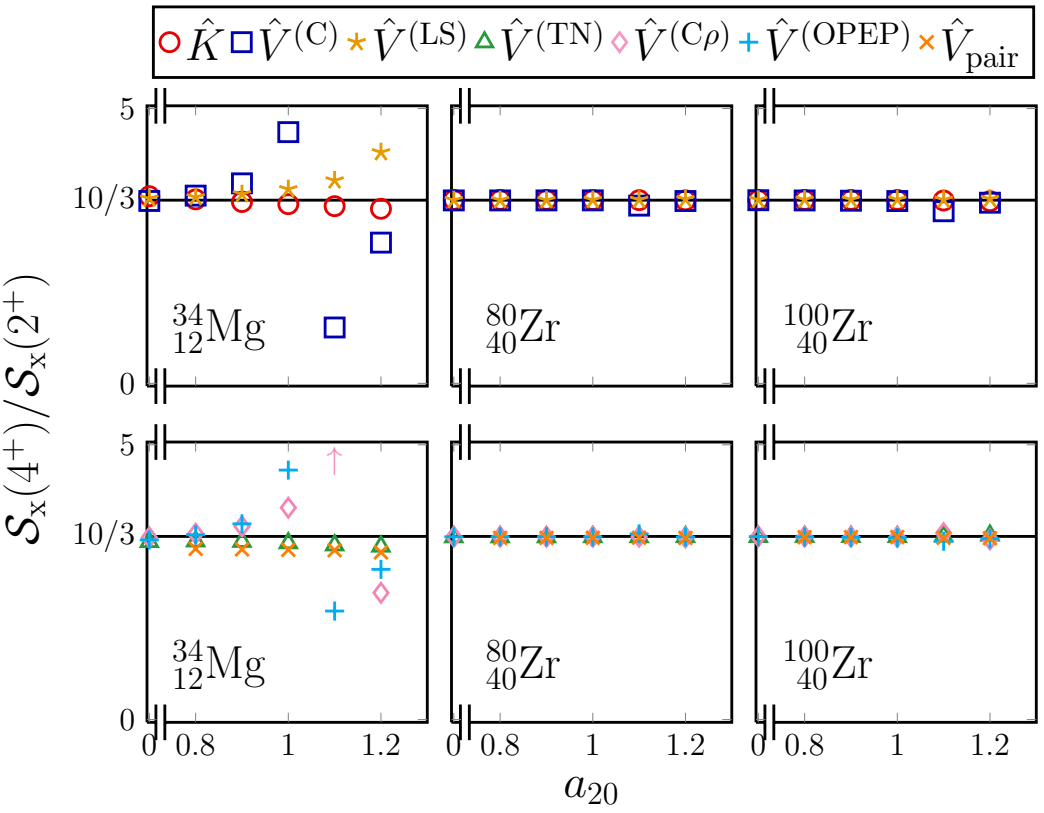

Figure 7.20: The g dependence of the ratios $\mathcal{S}_x(4^+)/\mathcal{S}_x(2^+)$. See Fig. 7.1 for conventions, where only the HF terms are considered. For $\hat{\mathcal{S}} = \hat{V}^{(C)}$, $\hat{V}^{(LS)}$, $\hat{V}^{(TN)}$, $\hat{V}^{(C\rho)}$, and $\hat{V}^{(OPEP)}$, the pairing terms are excluded. The g dependence of the ratios $\mathcal{S}_x(4^+)/\mathcal{S}_x(2^+)$ for the pairing terms (denoted as $\hat{V}_{pair}$) are represented by orange crosses.

In Fig. 7.20, the g dependence of the ratios of the individual terms in the effective Hamiltonian $\mathcal{S}_{\rm x}(4^+)/\mathcal{S}_{\rm x}(2^+)$ are shown for the deformed ${}^{34}_{12}$Mg and ${}^{80,100}_{40}$Zr nuclei. The chemical-potential terms in Eq. (6.65) are not considered in the calculations of $\mathcal{S}_{\rm x}(J^+)$ for the individual terms of the effective Hamiltonian. For the ${}^{80,100}_{40}$Zr nuclei, the ratios $\mathcal{S}_{\rm x}(4^+)/\mathcal{S}_{\rm x}(2^+)$ are close to 10/3, which is almost independent of g and $\hat{\mathcal{S}}$. For the ${}^{34}_{12}$Mg nucleus, the ratios $\mathcal{S}_{\rm x}(4^+)/\mathcal{S}_{\rm x}(2^+)$ for $\hat{\mathcal{S}} = \hat{K}$, $\hat{V}^{(\rm TN)}$, and $\hat{V}_{\rm pair}$ are also almost independent of g, while those for $\hat{V}^{(\rm C)}$, $\hat{V}^{(\rm LS)}$, $\hat{V}^{(\rm C\rho)}$, and $\hat{V}^{(\rm OPEP)}$ deviate from 10/3 with increasing g.

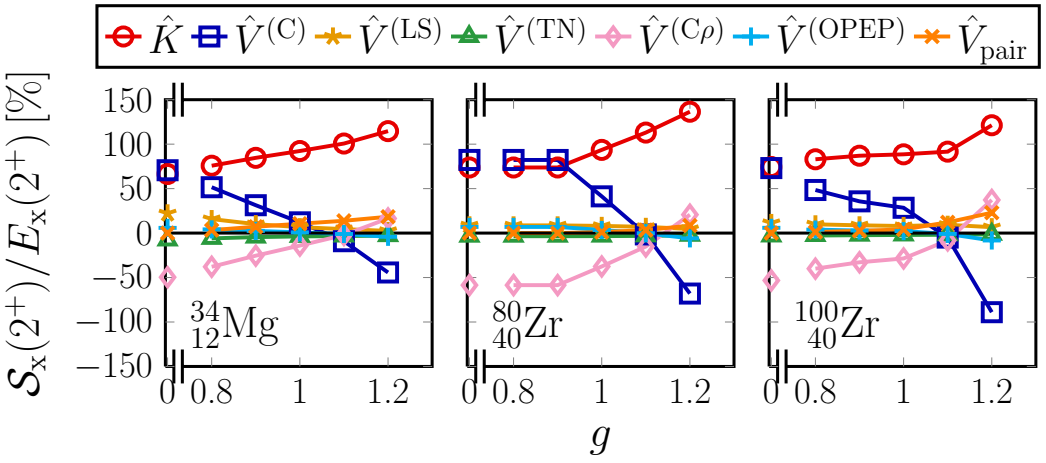

Figure 7.21: The g dependence of the ratios $\mathcal{S}_{\rm x}(2^+)/E_{\rm x}(2^+)$.

In Fig. 7.21, the g dependence of the ratios $\mathcal{S}_{\rm x}(2^+)/E_{\rm x}(2^+)$ is shown for the deformed ${}^{34}_{12}$Mg and ${}^{80,100}_{40}$Zr nuclei. The values of the projected energies are $\langle 0^+|H|0^+\rangle$, not including the chemical-potential terms in Eq. (6.65). For $\hat{\mathcal{S}} = \hat{V}^{(\rm C)}$, $\hat{V}^{(\rm LS)}$, $\hat{V}^{(\rm TN)}$, $\hat{V}^{(\rm C\rho)}$, and $\hat{V}^{(\rm OPEP)}$, the pairing terms are excluded. As g increases, the ratios $\mathcal{S}_{\rm x}(2^+)/E_{\rm x}(2^+)$ change sensitively from the critical points for $\hat{\mathcal{S}} = \hat{K}$, $\hat{V}^{(\rm C)}$, and $\hat{V}^{(\rm C\rho)}$. As g increases, the contribution of $\hat{K}$ does significantly. As g increases, the values of $\mathcal{S}_{\rm x}(2^+)/E_{\rm x}(2^+)$ for $\hat{V}^{(\rm C)}$ decrease, and those of $\hat{V}^{(\rm C\rho)}$ increase. Their signs change near $g = 1.1$. The pair correlations could change the components of the rotational energy qualitatively. As g increases, the contribution of $\hat{V}_{\rm pair}$ to the rotational energy does. The components of $\hat{V}_{\rm pair}$ are almost dominated by the central force in Eq. (2.33).

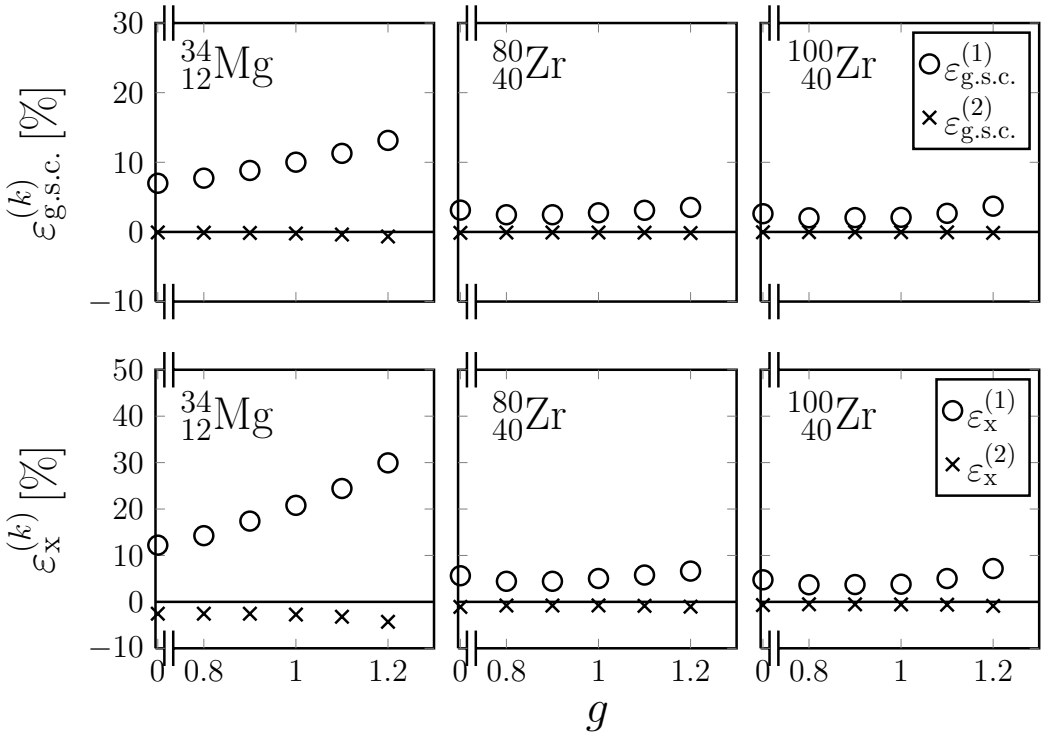

Figure 7.22: The g dependence of $\varepsilon^{(k)}_{\rm g.s.c.}$ and $\varepsilon^{(k)}_{\rm x}$ for $k = 1, 2$ in Eq. (7.6).

The g dependence of $\varepsilon^{(k)}_{\rm g.s.c.}$ and $\varepsilon^{(k)}_{\rm x}$ for $k = 1, 2$ in Eq. (7.6) is shown for the deformed $^{34}_{12}$Mg and $^{80,100}_{40}$Zr nuclei in Fig. 7.22. The values of $\varepsilon^{(k)}_{\rm g.s.c.}$ and $\varepsilon^{(k)}_{\rm x}$ for $k = 1, 2$ are not sensitive to g and close to zero for the $^{80,100}_{40}$Zr nuclei. Therefore, the contributions of the higher-s_{2n} terms to the ground-state correlations $\Delta E_{\rm g.s.c.}$ in Eq. (4.32) and the first excitation energies $E_{\rm x}(2^+)$ (or the moment of inertia in Eq. (4.37)) are small, and approximation by Peierls and Yoccoz in Eq. (4.38) is good. Especially, $C[\hat{\mathcal{S}}, \hat{J}^2_y]$ in Eq. (4.38b) is mainly responsible for the results in Fig. 7.21. On the other hand, as g increases, $\varepsilon^{(1)}_{\rm g.s.c.}$ and $\varepsilon^{(1)}_{\rm x}$ do for the $^{34}_{12}$Mg nucleus. The values of both $\varepsilon^{(2)}_{\rm g.s.c.}$ and $\varepsilon^{(2)}_{\rm x}$ are close to zero for the $^{34}_{12}$Mg nucleus. Therefore, as g increases, the contributions of the s_4 terms to $\Delta E_{\rm g.s.c.}$ in Eq. (4.32) and $E_{\rm x}(2^+)$ in Eq. (4.37) do for the $^{34}_{12}$Mg nucleus. It seems that the results of $\varepsilon^{(1)}_{\rm g.s.c.}$ and $\varepsilon^{(1)}_{\rm x}$ in Fig. 7.22 correspond to the results in Fig. 7.17. According to the pair correlations, the higher-order s_{2n} terms in the cumulant expansion to the ground-state correlations and the moment of inertia could play an important rule in the light nuclei.

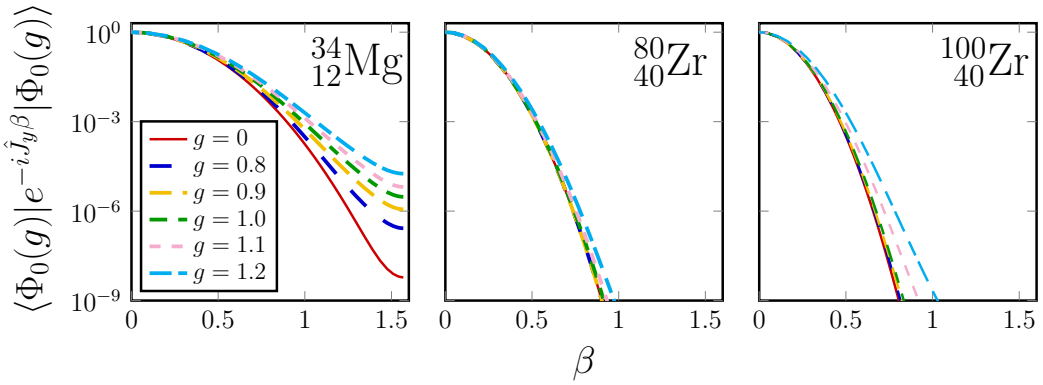

Figure 7.23: The overlap functions $\langle\Phi_0(g)|e^{-i\hat{J}_y\beta}|\Phi_0(g)\rangle$. The individual lines correspond to the g values shown in the insets.

Figure 7.23 shows the overlap functions $\langle\Phi_0(g)|e^{-i\hat{J}_y\beta}|\Phi_0(g)\rangle$ for the deformed $^{34}_{12}$Mg and $^{80,100}_{40}$Zr nuclei with the parameter g. For the $^{80,100}_{40}$Zr nuclei, the overlap functions $\langle\Phi_0(g)|e^{-i\hat{J}_y\beta}|\Phi_0(g)\rangle$ are insensitive to g. As g increases, the overlap functions have broader peaks for the $^{34}_{12}$Mg nucleus. It seems that the results in Fig. 7.23 correspond to those in Fig. 7.17.

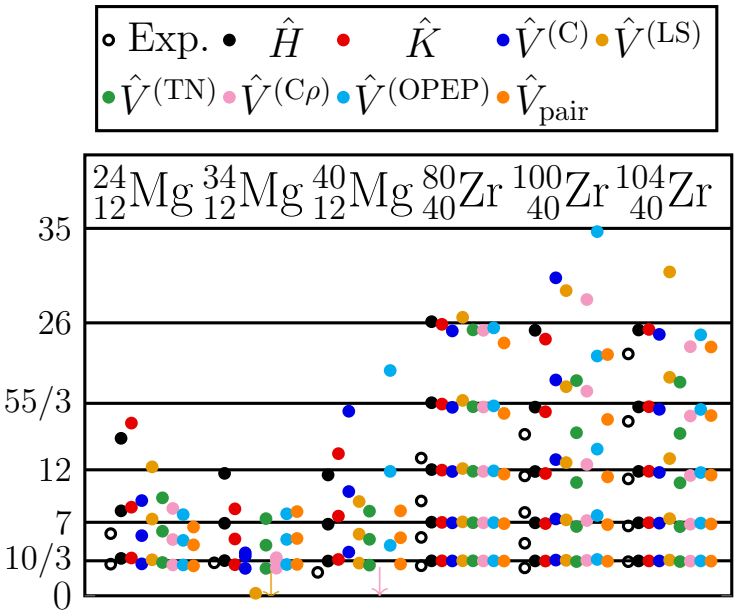

Figure 7.24: The ratios $\mathcal{S}_x(J^+)/\mathcal{S}_x(2^+)$ for the deformed $^{24,34,40}_{12}$Mg and $^{80,100,104}_{40}$Zr nuclei at their lowest minima in the HFB solutions. See conventions for Figs. 7.1 and 7.20.

We have calculated self-consistently the axial-HFB solutions for the deformed nuclei. The pure rotational energy for the deformed HFB solutions has also been calculated by using the AMP. Figure 7.24 shows that the ratios $\mathcal{S}_x(J^+)/\mathcal{S}_x(2^+)$ for the deformed $^{24,34,40}_{12}$Mg and $^{80,100,104}_{40}$Zr nuclei at their lowest minima in the HFB solutions, all of which have prolate shapes. The ratios $E_x(4^+)/E_x(2^+)$ obtained by present work are

close to those of the experiments and 10/3 except ${}^{40}_{12}$Mg. Except for the Mg nuclei, the ratios $\mathcal{S}_{\rm x}(J^+)/\mathcal{S}_{\rm x}(2^+)$ of the individual terms in the effective Hamiltonian are also close to the $J(J+1)$ lines. On the other hand, some interactions do not obey the $J(J+1)$ rule or the J ordering, such as $0^+, 2^+, 4^+, \ldots$ or $\ldots, 4^+, 2^+, 0^+$, for the Mg nuclei, which is indicated from the results in Fig. 7.20.

It seems that the ratios $\mathcal{S}_{\rm x}(J^+)/\mathcal{S}_{\rm x}(2^+)$ in Fig. 7.24 tend to deviate from the $J(J+1)$ lines more than those for the deformed HF solutions in Figs. 7.1 and 7.2. Since the pair correlations can reduce the values of a_{20}, as shown in Fig. 7.17, the ratios $\mathcal{S}_{\rm x}(J^+)/\mathcal{S}_{\rm x}(2^+)$ for the HFB solutions could deviate from the $J(J+1)$ lines more than those for the HF solutions. The values of the deformation parameter a_{20} in Eq. (7.4) for ${}^{24}_{12}$Mg, ${}^{34}_{12}$Mg, ${}^{40}_{12}$Mg, ${}^{80}_{40}$Zr, ${}^{100}_{40}$Zr, and ${}^{104}_{40}$Zr at their lowest minima in the deformed HFB solutions are 0.54, 0.44, 0.43, 0.53, 0.41, and 0.43, respectively. Considering the results in Fig. 7.17, the values of a_{20} for the HFB solutions are smaller than those for the HF solutions of ${}^{34,40}_{12}$Mg and ${}^{100}_{40}$Zr.

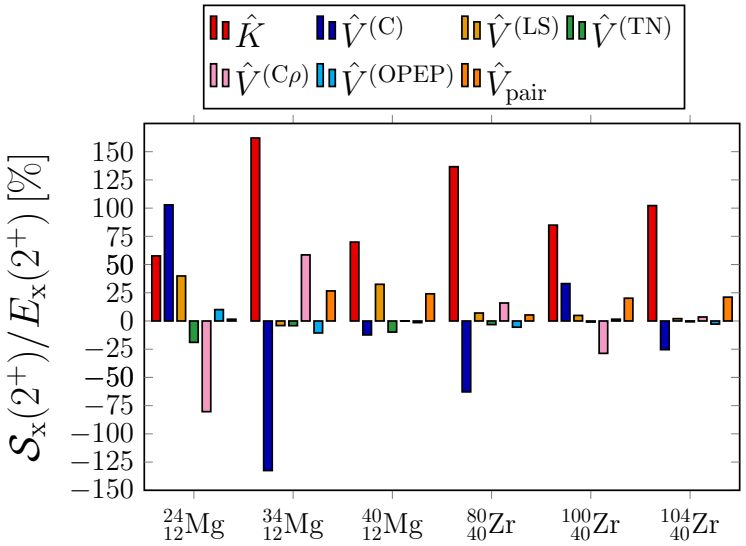

Figure 7.25: The ratios $\mathcal{S}_{\rm x}(2^+)/E_{\rm x}(2^+)$ for the deformed nuclei at their lowest minima in the HFB solutions.

In Fig. 7.25, the ratios $\mathcal{S}_{\rm x}(2^+)/E_{\rm x}(2^+)$ for the deformed ${}^{24,34,40}_{12}$Mg and ${}^{80,100,104}_{40}$Zr nuclei at their lowest minima in the HFB solutions are shown. The results significantly depend on the nuclei. The contributions of the interactions $\hat{V}^{(\rm C)}$ and $\hat{V}^{(\rm C\rho)}$ to the rotational energy shown in Fig. 7.25, including their signs, are greatly different from them shown in Fig. 7.3 for some nuclei, as indicated in Fig. 7.21. Additionally, the small deformation of the HFB solutions compared with that of the HF solutions for the ${}^{34,40}_{12}$Mg and the ${}^{100}_{40}$Zr nuclei could contribute to the results in Fig. 7.25.

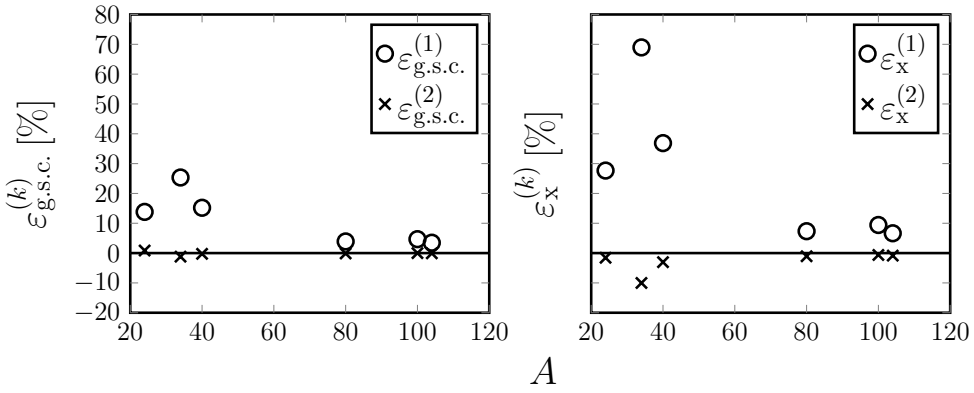

Figure 7.26: The values of $\varepsilon^{(k)}_{\rm g.s.c.}$ and $\varepsilon^{(k)}_{\rm x}$ for $k = 1, 2$ in Eq. (7.6) for the deformed ${}^{24,34,40}_{12}$Mg and ${}^{80,100,104}_{40}$Zr isotopes at their lowest minima in the HFB solutions.

The values of $\varepsilon^{(k)}_{\rm g.s.c.}$ and $\varepsilon^{(k)}_{\rm x}$ for $k = 1, 2$ in Eq. (7.6) are shown for the deformed ${}^{24,34,40}_{12}$Mg and ${}^{80,100,104}_{40}$Zr nuclei at their lowest minima in the HFB solutions in Fig. 7.26. For the ${}_{40}$Zr nuclei, both the values of $\varepsilon^{(1)}_{\rm g.s.c.}$ and $\varepsilon^{(1)}_{\rm x}$ are less than 10%. Thus, the Peierls and Yoccoz approximation in Eq. (4.38) is good. For the ${}_{12}$Mg nuclei, both $|\varepsilon^{(1)}_{\rm g.s.c.}|$ and $|\varepsilon^{(1)}_{\rm x}|$ are larger than $|\varepsilon^{(2)}_{\rm g.s.c.}|$ and $|\varepsilon^{(2)}_{\rm x}|$, respectively. The contributions of the s_4 terms to the ground-state correlations $\Delta E_{\rm g.s.c.}$ in Eq. (4.32) and the first excitation energies $E_{\rm x}(2^+)$ (or the moment of inertia in Eq. (4.37)) are not negligible for the ${}_{12}$Mg nuclei. Therefore, it is suggested that the higher-order s_{2n} terms in the cumulant expansion play an important rule in the light nuclei, contributing to the ground-state correlations and the moment of inertia.

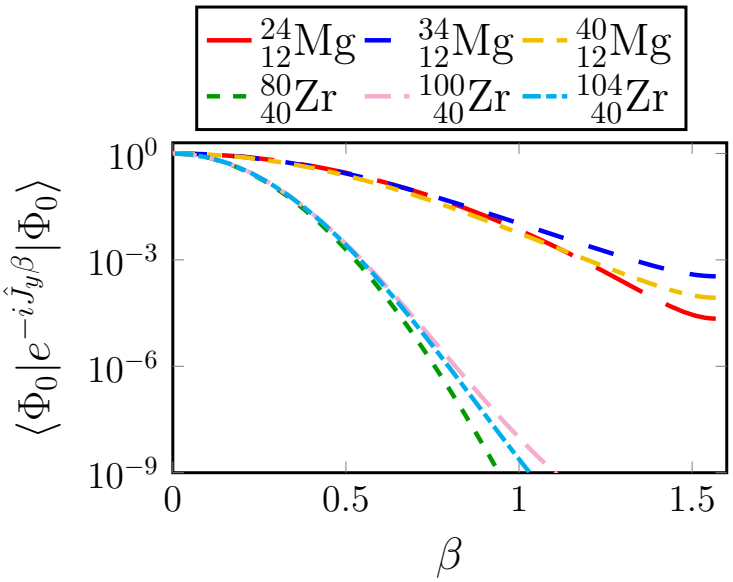

Figure 7.27: The overlap functions $\langle\Phi_0|e^{-i\hat{J}_y\beta}|\Phi_0\rangle$ for the deformed ${}^{24,34,40}_{12}$Mg and ${}^{80,100,104}_{40}$Zr isotopes at their lowest minima in the HFB solutions.

Figure 7.27 shows the overlap functions $\langle\Phi_0|e^{-i\hat{J}_y\beta}|\Phi_0\rangle$ for the deformed ${}^{24,34,40}_{12}$Mg and ${}^{80,100,104}_{40}$Zr isotopes at their lowest minima in the HFB solutions. The overlap

functions for the $^{80,100,104}_{40}$Zr nuclei have sharper peaks than those for the $^{24,34,40}_{12}$Mg nuclei. The overlap functions $\langle\Phi_0|e^{-i\hat{J}_y\beta}|\Phi_0\rangle$ in Fig. 7.27 have broader peaks than those in Fig. 7.11. The values of $(\sigma[\hat{J}_y])^2$ for $^{24}_{12}$Mg, $^{34}_{12}$Mg, $^{80}_{40}$Zr, and $^{104}_{40}$Zr, which are calculated from $\langle\Phi_0|\hat{\boldsymbol{J}}^2|\Phi_0\rangle$ [see Eq. (4.15b)], are 10.0, 10.8, 51.2, and 49.9, respectively. In the $^{80}_{40}$Zr nucleus, the value of $(\sigma[\hat{J}_y])^2$ for the HFB state is smaller than that for the HF state, although the value of the deformation parameter a_{20} for the HFB state is larger than that for the HF state, as shown in Fig. 7.17. While the latter considers only the spatial correlations, the former considers the spin correlations, additionally.

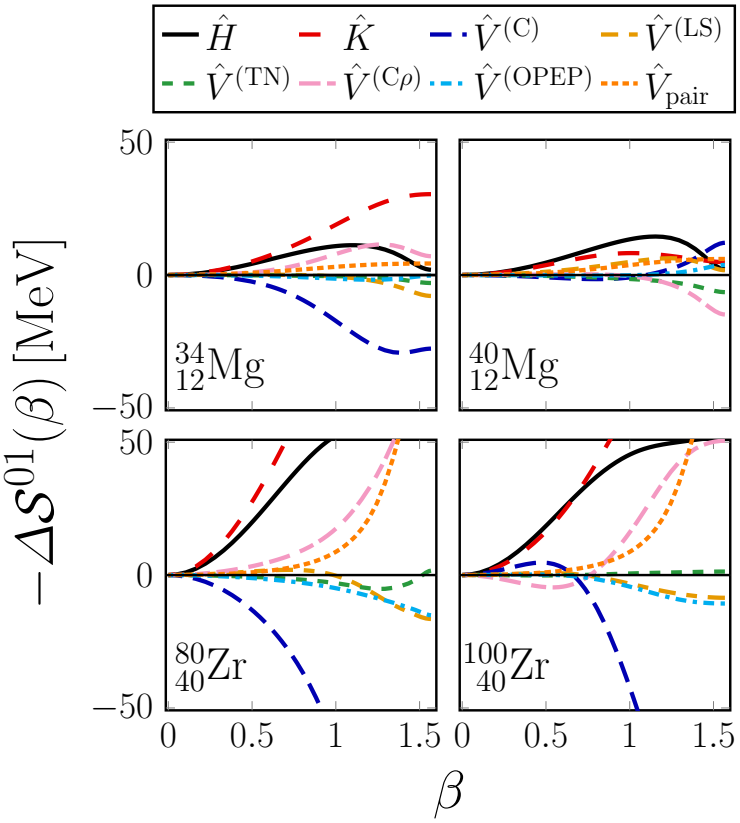

Figure 7.28: The behavior of $-\Delta\mathcal{S}^{01}(\beta)$ for the individual terms of the Hamiltonian for the deformed $^{34,40}_{12}$Mg and $^{80,100}_{40}$Zr nuclei at their lowest minima in the HFB solutions.

In Fig. 7.28, we show $-\Delta\mathcal{S}^{01}(\beta)$ in Eq. (7.7) for the deformed $^{34,40}_{12}$Mg and $^{80,100}_{40}$Zr nuclei at their lowest minima in the HFB solutions. Considering Eq. (7.8), the values of $|C[\hat{\mathcal{S}}, \hat{J}_y^2]|$ increase significantly for $\hat{\mathcal{S}} = \hat{K}$, $\hat{V}^{(\mathrm{C})}$, and $\hat{V}^{(\mathrm{C}\rho)}$ as the mass number increases. The signs of $C[\hat{\mathcal{S}}, \hat{J}_y^2]$ for $\hat{V}_{\mathrm{pair}}$ are positive without exceptions. The signs of $C[\hat{\mathcal{S}}, \hat{J}_y^2]$ for $\hat{\mathcal{S}} = \hat{V}^{(\mathrm{C})}$ are negative, and those for $\hat{V}^{(\mathrm{C}\rho)}$ are positive for the $^{34}_{12}$Mg and $^{80}_{40}$Zr nuclei, which are different from those in Fig. 7.14. The pair correlations could change the signs of $C[\hat{\mathcal{S}}, \hat{J}_y^2]$ for $\hat{\mathcal{S}} = \hat{V}^{(\mathrm{C})}$ and $\hat{V}^{(\mathrm{C}\rho)}$, contributing to the results in Fig. 7.25. Even though the HFB solution of $^{100}_{40}$Zr has the pair correlations, the value of $C[\hat{\mathcal{S}}, \hat{J}_y^2]$ for $\hat{\mathcal{S}} = \hat{V}^{(\mathrm{C})}$ ($\hat{V}^{(\mathrm{C}\rho)}$) is positive (negative). The result for the $^{100}_{40}$Zr nuclei could be influenced by the discrepancy of the deformation parameter between the HF and HFB states in Fig. 7.17]. The flat structure of $-\Delta\mathcal{S}^{01}(\beta)$ for $\hat{\mathcal{S}} = \hat{V}^{(\mathrm{LS})}$ in $^{34}_{12}$Mg

and $\hat{V}^{(\mathrm{C}\rho)}$ in ${}^{40}_{12}$Mg could correspond to the deviation from the $J(J+1)$ line or out of the J ordering in Fig. 7.24. The results in Fig. 7.28 correspond well to those in Figs. 7.24 and 7.25.

7.5 Degree of proximity for nucleons associated with nucleonic interaction

We have further investigated what governs the g dependence of the contributions of the nucleonic interactions to the pure rotational energy, including their signs of $\hat{V}^{(\mathrm{C})}$ and $\hat{V}^{(\mathrm{C}\rho)}$ in Fig. 7.21. We have calculated the degree of proximity $\langle\hat{\delta}^{(2)}\rangle$ by using the AMP in order to understand contributions of the interactions for the rotational energy of nuclei, as noticed in Chap. 5. In this section, the degree of proximity is discussed with numerical results for the deformed HF, HF+BCS, and HFB solutions of ${}^{34}_{12}$Mg and ${}^{80,100}_{40}$Zr.

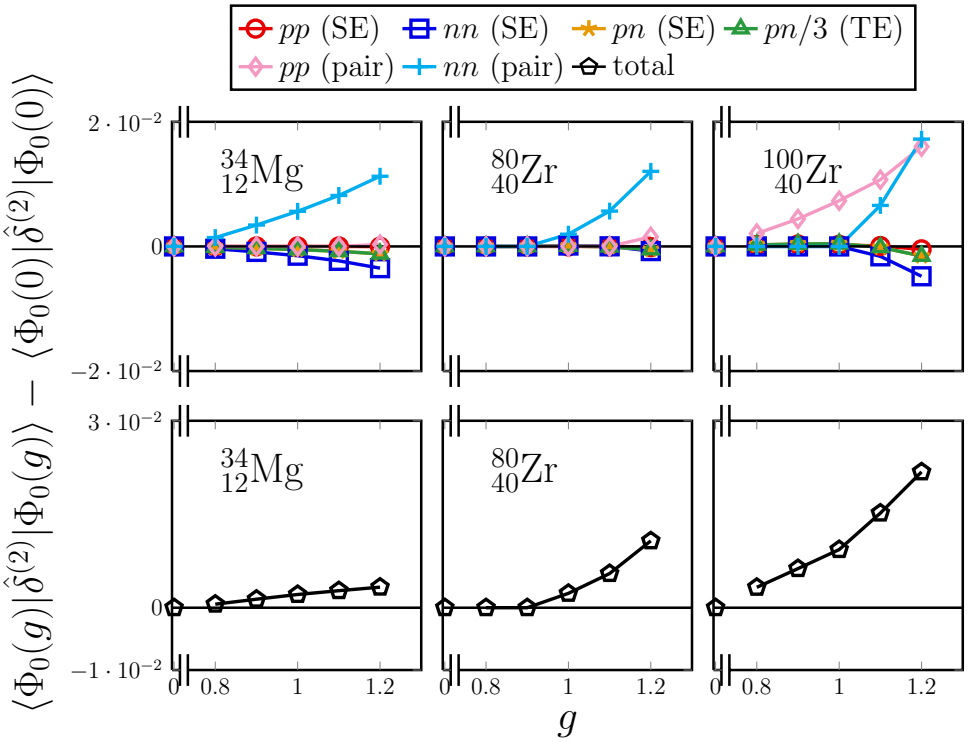

Figure 7.29: The g dependence of $\langle\Phi_0(g)|\hat{\delta}^{(2)}|\Phi_0(g)\rangle - \langle\Phi_0(0)|\hat{\delta}^{(2)}|\Phi_0(0)\rangle$ for the deformed HF+BCS solutions of ${}^{34}_{12}$Mg and ${}^{80,100}_{40}$Zr. The black pentagons are the total values of $\langle\Phi_0(g)|\hat{\delta}^{(2)}|\Phi_0(g)\rangle - \langle\Phi_0(0)|\hat{\delta}^{(2)}|\Phi_0(0)\rangle$. The proton (neutron) is represented by $p(n)$. The separated values of $\langle\Phi_0(g)|\hat{\delta}^{(2)}|\Phi_0(g)\rangle - \langle\Phi_0(0)|\hat{\delta}^{(2)}|\Phi_0(0)\rangle$ into the TE and SE channels in Eq. (6.32) are also shown; in concrete, red circles represent pp in the HF term, blue squares nn in the HF term, yellow stars pn of the SE channel in the HF term, green triangles pn of the TE channel in the HF term, pink diamonds pp in the pairing term, and sky-blue pluses nn in the pairing term. The values in the TE channel are divided by three, denoted as $pn/3$ (TE).

In Fig. 7.29, the g dependence of $\langle\Phi_0(g)|\hat{\delta}^{(2)}|\Phi_0(g)\rangle - \langle\Phi_0(0)|\hat{\delta}^{(2)}|\Phi_0(0)\rangle$ is shown for the deformed HF+BCS solutions of ${}^{34}_{12}$Mg and ${}^{80,100}_{40}$Zr. The values of $\langle\Phi_0(0)|\hat{\delta}^{(2)}|\Phi_0(0)\rangle$ for the ${}^{34}_{12}$Mg, ${}^{80}_{40}$Zr, and ${}^{100}_{40}$Zr nuclei are 1.22, 3.43, and 4.28, respectively. As g increases, $\langle\Phi_0(g)|\hat{\delta}^{(2)}|\Phi_0(g)\rangle - \langle\Phi_0(0)|\hat{\delta}^{(2)}|\Phi_0(0)\rangle$ does. Thus, the degree of proximity $\langle\Phi_0(g)|\hat{\delta}^{(2)}|\Phi_0(g)\rangle$ increases by the pair correlations. The values of $\langle\Phi_0(g)|\hat{\delta}^{(2)}|\Phi_0(g)\rangle$ are separated into the isospin components, in concrete, the SE and the TE channels [see also Sec. 2.4] for the HF and the pairing terms in Eq. (6.32), respectively. The value of $\langle\Phi_0(g)|\hat{\delta}^{(2)}|\Phi_0(g)\rangle$ for the TE channel is almost three times larger than that for the SE channel due to the spin triplet. Thus, it is fair to divide the values of $\langle\Phi_0(g)|\hat{\delta}^{(2)}|\Phi_0(g)\rangle$ for the TE channel by three. The contributions of the pairing terms to $\langle\Phi_0(g)|\hat{\delta}^{(2)}|\Phi_0(g)\rangle - \langle\Phi_0(0)|\hat{\delta}^{(2)}|\Phi_0(0)\rangle$ are large, and those of the HF terms are small. The critical points of the proton and the neutron are different in general.

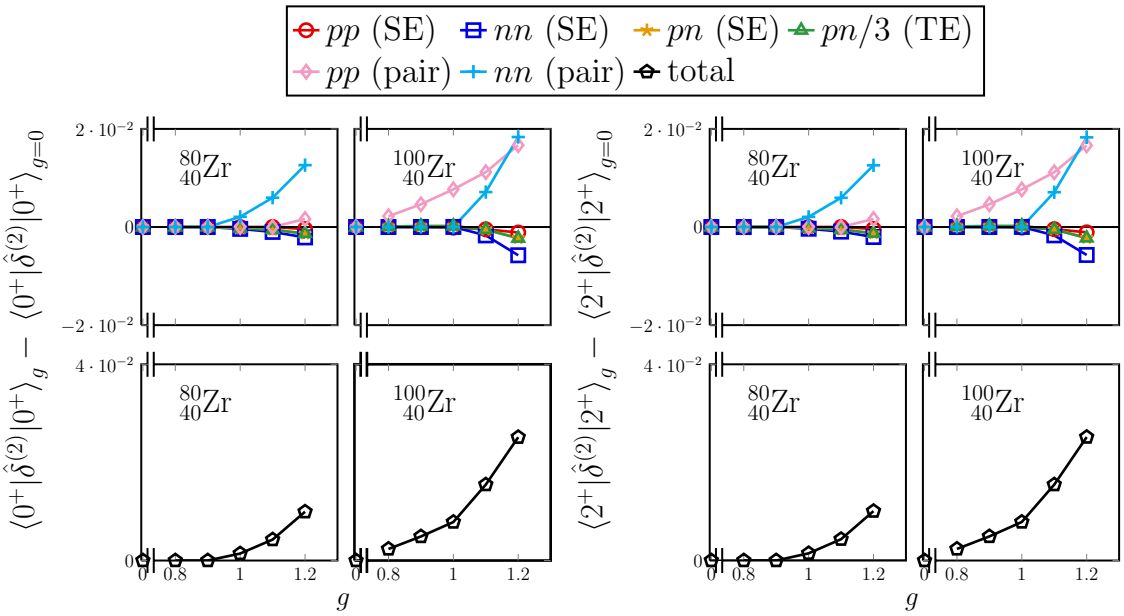

Figure 7.30: The g dependence of $\langle J^+|\hat{\delta}^{(2)}|J^+\rangle_g - \langle J^+|\hat{\delta}^{(2)}|J^+\rangle_{g=0}$ for $J = 0, 2$ in Eq. (7.11).

We have calculated the degree of proximity for eigenstates of J by using the AMP for the deformed HF, HF+BCS, and HFB solutions of ${}^{34}_{12}$Mg and ${}^{80,100}_{40}$Zr. By using Eqs. (4.10) and (5.1), $\langle J^+|\hat{\delta}^{(2)}|J^+\rangle_g$ is defined as

$$\langle J^+|\hat{\delta}^{(2)}|J^+\rangle_g := \frac{\langle\Phi_0(g)|\hat{\delta}^{(2)}\hat{P}^{(J)}_{00}|\Phi_0(g)\rangle}{\langle\Phi_0(g)|\hat{P}^{(J)}_{00}|\Phi_0(g)\rangle}. \tag{7.11}$$

The g dependence of $\langle J^+|\hat{\delta}^{(2)}|J^+\rangle_g - \langle J^+|\hat{\delta}^{(2)}|J^+\rangle_{g=0}$ for $J = 0, 2$ of ${}^{80,100}_{40}$Zr is shown in Fig. 7.30. The results for both $J = 0, 2$ in Fig. 7.30 are almost the same as those in Fig. 7.29.

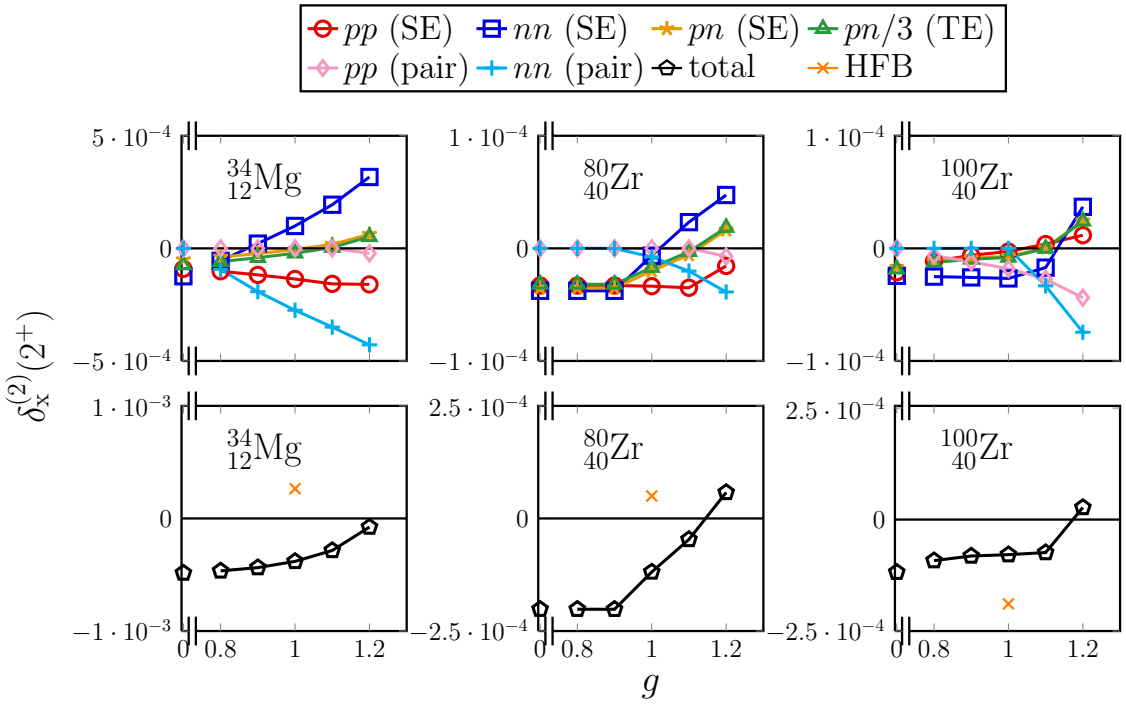

Figure 7.31: The g dependence of $\delta^{(2)}_{\rm x}(2^+)$ in Eq. (7.12). The orange crosses are the total values of $\delta^{(2)}_{\rm x}(2^+)$ for the HFB solutions at their lowest minima.

We define $\delta^{(2)}_{\rm x}(J^+)$ as

$$\delta^{(2)}_{\rm x}(J^+) := \langle J^+|\hat{\delta}^{(2)}|J^+\rangle - \langle 0^+|\hat{\delta}^{(2)}|0^+\rangle\,, \tag{7.12}$$

which corresponds to Eq. (7.1) for $\hat{\mathcal{S}} = \hat{\delta}^{(2)}$. The g dependence of $\delta^{(2)}_{\rm x}(2^+)$ for the deformed HF+BCS solutions of $^{34}_{12}$Mg and $^{80,100}_{40}$Zr are shown in Fig. 7.31. The values of $\delta^{(2)}_{\rm x}(2^+)$ for the deformed HFB solutions at their lowest minima are also shown there. The value of $\delta^{(2)}_{\rm x}(2^+)$ for the HFB solution of $^{80}_{40}$Zr is close to those for the HF+BCS solutions near $g = 1.2$, while there is a discrepancy between them for $^{34}_{12}$Mg and $^{100}_{40}$Zr. This discrepancy seems to be associated with the discrepancy of the deformation parameter between the HFB and HF+BCS solutions in Fig. 7.17, which is associated with the matrix D in Eq. (6.21).

For the deformed HF (or $g = 0$) solutions, the values of $\delta^{(2)}_{\rm x}(2^+)$ are negative. Thus, the degree of proximity $\langle J^+|\hat{\delta}^{(2)}|J^+\rangle$ decreases, i.e., the nucleons spread, as J increases for the deformed HF solutions. As g increases, the values of $\delta^{(2)}_{\rm x}(2^+)$ do from the critical points. Thus, the pair correlations ease the effect that the nucleons spread with increasing J. The signs of $\delta^{(2)}_{\rm x}(2^+)$ change between $g = 1.1$ and $g = 1.2$. The pair correlations enable to increase the degree of proximity $\langle J^+|\hat{\delta}^{(2)}|J^+\rangle$, i.e., the nucleons gather, as J increases. For actual nuclei, gradual stretching of the intrinsic state with increasing J could ease the degree of proximity, as handled in the cranking model [3, 9, 13] and the variation after projection (VAP) schemes [3].

The values of $\delta^{(2)}_{\rm x}(2^+)$ are separated into the isospin components. As g increases, the four channels of $T = 0, 1$ in the HF term also do, and the two channels of $T = 1$ in the pairing term decrease from zero. Although we have excluded the proton-neutron

pairing, the proton-neutron correlations in the HF term are sizable. The results in Fig. 7.31 well correlate with those for the interactions in Fig. 7.21, i.e., $\delta_{\rm x}^{(2)}(2^+)$ corresponds to $\mathcal{S}_{\rm x}(2^+)/E_{\rm x}(2^+)$ or $\mathcal{S}_{\rm x}(2^+)$ for $\hat{\mathcal{S}} = \hat{V}^{(\rm C)}$, $\hat{V}^{(\rm C\rho)}$, and $\hat{V}_{\rm pair}$ except minor quantitative differences. Therefore, for example, the negative (positive) contributions of the repulsive forces to the rotational energy in Fig. 7.21 can be interpreted approximately as the degree of proximity $\langle J^+|\hat{\delta}^{(2)}|J^+\rangle$ decreases (increases), i.e., the nucleons spread (gather), as J increases. If the rotational energy is roughly composed of only the kinetic energy, the degree of proximity $\langle J^+|\hat{\delta}^{(2)}|J^+\rangle$ will not depend on J so much. The contributions of the nucleonic interactions to the rotational energy could correspond to the J dependence of the degree of proximity $\langle J^+|\hat{\delta}^{(2)}|J^+\rangle$.

According to the above analysis, it is revealed that the the spatial correlations between nucleons could explain the contributions of the nucleonic interactions for the rotational energy.

7.6 Comparison of $E_{\rm x}(2^+)$ with rigid-rotor model and experiment

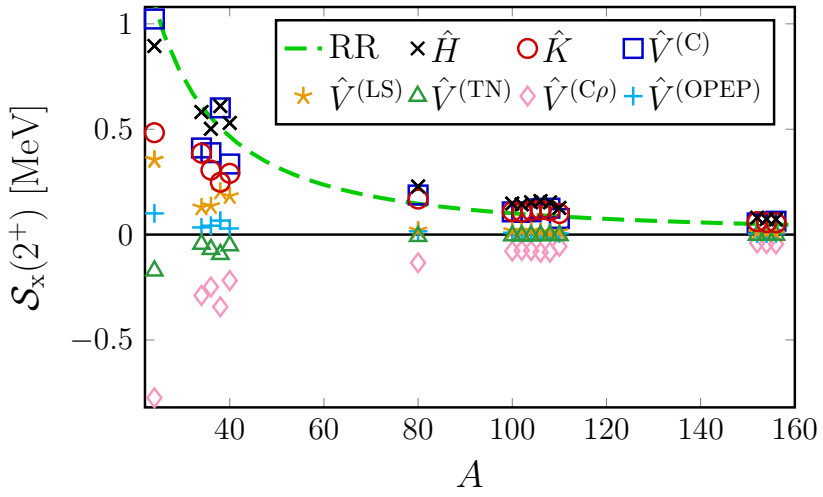

Figure 7.32: The excitation energies $E_{\rm x}(2^+)$ for the deformed ${}^{24,34-40}_{12}$Mg, ${}^{80,100-110}_{40}$Zr, and ${}^{152-156}_{62}$Sm isotopes at their lowest minima in the HF solutions. The black cross symbols represent the values of $E_{\rm x}(2^+)$ in the present calculations. The corresponding values of $\mathcal{S}_{\rm x}(2^+)$ are also shown. The green dashed line is the rigid-rotor value in Eq. (7.13) [1].

Figure 7.32 shows the calculated excitation energies $E_{\rm x}(2^+)$ and $\mathcal{S}_{\rm x}(2^+)$, the latter of which is the contribution of the individual terms of the effective Hamiltonian to the rotational energies [see Eq. (7.1)], for the deformed ${}_{12}$Mg, ${}_{40}$Zr, and ${}_{62}$Sm isotopes at their lowest minima in the HF solutions. As expected, the calculated $E_{\rm x}(2^+)$ tends to decrease as A increases. The absolute values of $\mathcal{S}_{\rm x}(2^+)$ for the individual terms of the

effective Hamiltonian do, as well. The rigid-rotor value [1] in Eq. (A.12) is also shown,

$$E_{\rm x}^{(\rm RR)}(J^+) = \frac{J(J+1)}{2\mathcal{I}^{(\rm RR)}}, \qquad \mathcal{I}^{(\rm RR)} \approx 0.0138\, A^{5/3}[\rm MeV^{-1}]. \tag{7.13}$$

In the classical mechanics, the rotational energy of the rigid body comes from kinetic energy. Interestingly, the values of $\mathcal{S}_{\rm x}(2^+)$ for $\hat{\mathcal{S}} = \hat{K}$ are close to the rigid-rotor value in the $_{40}$Zr and $_{62}$Sm regions.

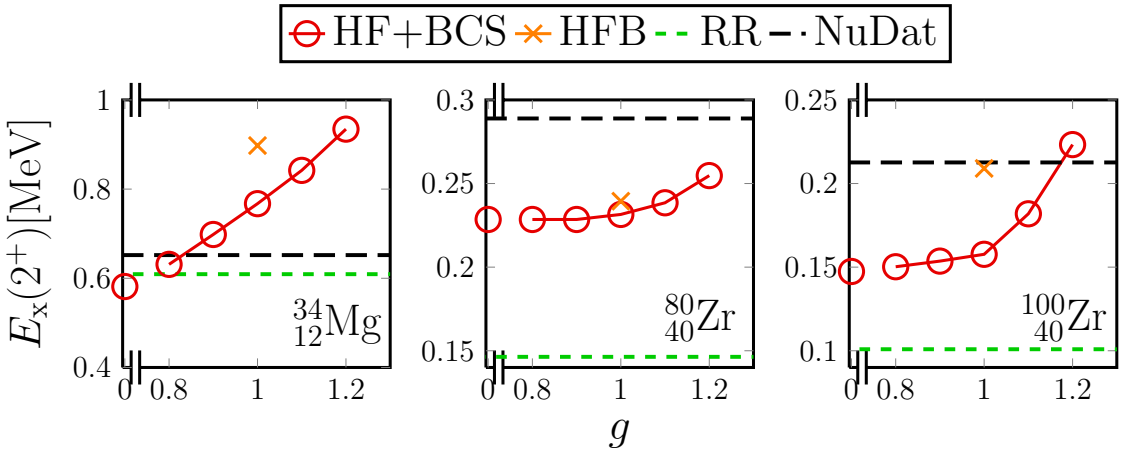

Figure 7.33: The g dependence of the excitation energies $E_{\rm x}(2^+)$ for the deformed HF+BCS solutions of $^{34}_{12}$Mg and $^{80,100}_{40}$Zr, which is represented by the red circles. The orange crosses represent the values for the deformed HFB solutions at their lowest minima. The experimental values are displayed by black dashed lines [2]. The green dashed lines are the rigid-rotor values in Eq. (7.13) [1].

Figure 7.33 shows the g dependence of the excitation energies $E_{\rm x}(2^+)$ for the deformed HF+BCS solutions of $^{34}_{12}$Mg and $^{80,100}_{40}$Zr. The results for the deformed HFB solutions at their lowest minima are also shown. The chemical-potential terms in Eq. (6.65) are considered. As g increases, the excitation energies $E_{\rm x}(2^+)$ do. This result corresponds with that derived from the Belyaev formula in Eq. (D.3) qualitatively. The Belyaev formula considers the correlations breaking time-reversal symmetry. On the other hand, the time-reversal symmetry is assumed in the present AMP calculations. Thus, the pair correlations can reduce the moment of inertia with the time-reversal symmetry. Compared to the experimental values, the values of $E_{\rm x}(2^+)$ for the deformed HFB solutions are large for the $^{34}_{12}$Mg nucleus, while they are slightly small for the $^{80,100}_{40}$Zr nuclei. The rigid-rotor values are smaller than the values of $E_{\rm x}(2^+)$ for the deformed HFB sloutions.

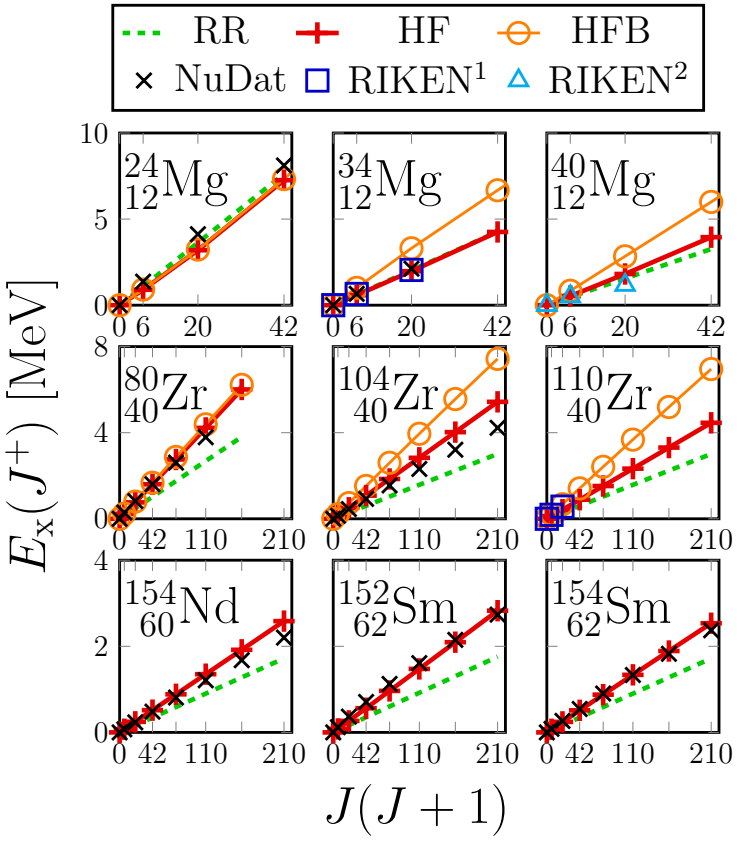

Figure 7.34: The excitation energies for the deformed nuclei at their lowest minima. The experimental values are displayed by black cross [2], blue square [92], and sky-blue triangle symbols [97]. The green dashed lines are the rigid-rotor values calculated from Eq. (7.13). The red plus (orange circle) symbols are obtained by the deformed HF (HFB) solutions in the present work.

Figure 7.34 shows the excitation energies for the deformed nuclei at their lowest minima, all of which have prolate shapes. Since the numerical cost of the axial-HFB calculations for $_{60}$Nd and $_{62}$Sm isotopes is high, we could not obtain the convergence of the solutions in this work. The rigid-rotor energies are low compared to the experimental ones, *e.g.*, for the $_{40}$Zr, $_{60}$Nd, and $_{62}$Sm regions. The excitation energies obtained by the present calculations for the HF solutions are close to the experimental values of $E_x(2^+)$ for all nuclides, while those for the HFB solutions are higher than them. However, we should be careful in comparing the values obtained by the present AMP calculations with those of the experiment. The intrinsic state is not always stable for increasing J, tending to decrease the excitation energies. It should also be noted that there is uncertainty in treating the density-dependent terms in the AMP calculations.

Chapter 8

Conclusion

In this study, the source code of the AMP calculations has been newly developed by using the GEM, so that it could be applied with the M3Y-type interactions for the self-consistent axially-deformed MF solutions. By using it, the AMP calculations have been implemented for the MF solutions of even-even nuclei with the semi-realistic effective Hamiltonian M3Y-P6. The pure rotational energies of nuclei for the fixed intrinsic states have been analyzed. The ratios of the individual terms of the Hamiltonian to the total rotational energies have been calculated.

In the case of the HF solutions, except for the light nuclei or the weakly-deformed solutions, their ratios are insensitive to nuclides and states. The contributions of the kinetic energies are large and close to the rigid-rotor values. A large cancellation occurs between the density-dependent channel and the density-independent one in the central force, although their sum is still sizable. The contributions of the noncentral forces are small. In contrast, the results significantly depend on nuclei and deformation for the light nuclei or the weakly-deformed solutions. The contributions of the noncentral forces are not negligible. Regardless of nuclides, the attractive forces decrease the moment of inertia, and the repulsive forces increase it.

The pair correlations significantly change the composition of the rotational energy. Therefore, the ratios could depend on nuclei and states, even for the well-deformed nuclei. As the pair correlations become strong, the contributions of the kinetic energies increase, those of the attractive forces decrease, and those of the repulsive forces increase. The nucleonic correlations between two nucleons contribute to the rotation and could explain the effects of nucleonic interactions on the rotational energy. The nucleons spread as the angular momentum J increases, while the pair correlations can reduce or change the effect. The J dependence of the intrinsic state may influence the results for actual nuclei, and we leave them for future works.

By using the cumulant expansion, a general formula for the rotational energy with axial symmetry is derived on the basis of the AMP. This formula is a generalization of those in Refs. [3, 7, 8, 10, 11, 13]. It is suggested that the newly found higher-order terms of the cumulant expansion play roles in the light nuclei or the weakly-deformed solutions, contributing to the rotational energy.

In this study, the author has revealed the components of the pure rotational energy of nuclei and contributed to further understanding of the rotational energy of quantum many-body systems generally.

Acknowledgments

I express my gratitude to Prof. H. Nakada for various advice and discussion. We have used his MF source code and also developed the AMP one. I am grateful to Prof. Emeritus H. Kurasawa for various advice on physics and computers with research environments. I would like to express my sincere thanks to Prof. Emeritus S. Iwasaki for his warm hospitality. I studied physics, mathematics, and numerical calculations with members of the nuclear-theory group and friends at Chiba University. I received valuable comments from many researchers or discussed with them, especially via my presentations in the meetings of JPS (the Physical Society of Japan), [1] the CCS (Center for Computational Sciences) international symposium 2021, [2] the workshop of YITP (Yukawa Institute for Theoretical Physics) in 2021, [3] and the MCD2022 (Mean-field and Cluster Dynamics in nuclear systems 2022). [4] I sincerely thank them. The authors are grateful to K. Yoshida and K. Washiyama for discussions in the MCD2022. I thank K. Neergard for drawing my attention to references proving the non-negativity of matrices in Appendix H. I appreciate that my family and friends have encouraged my research activities under the pandemic of COVID-19.

In this research, the numerical calculations were carried out on Yukawa-21 at YITP in Kyoto University. This research also used computational resources of Oakforest PACS and Wisteria provided by the MCRP (Multidisciplinary Cooperative Research Program) in CCS, University of Tsukuba, and HITACHI SR24000 at the IMIT (Institute of Management and Information Technologies), Chiba University. This research was supported by the research assistant program at Chiba University.

[1] https://www.jps.or.jp/english/meetings-and-awards/meeting.html
[2] https://www.ccs.tsukuba.ac.jp/sympo20211008en
[3] https://www2.yukawa.kyoto-u.ac.jp/~nsr-2021/index.php
[4] http://www2.yukawa.kyoto-u.ac.jp/~mcd2022/index.php

Appendix A

Phenomenological theory of deformation and rotation of nuclei

In this appendix, the phenomenological theory of deformation and rotation of nuclei is introduced, which is based on the rigid-rotor model [1].

A.1 Deformation parameter with ellipsoid of inertia

In this section, the deformation parameter is introduced. The ellipsoid of inertia is the following surface and its interior,

$$\left\{ x, y, z \;\middle|\; 0 \leq \left(\frac{x}{R_x}\right)^2 + \left(\frac{y}{R_y}\right)^2 + \left(\frac{z}{R_z}\right)^2 \leq 1 \right\}. \tag{A.1}$$

The deformation ratio δ is defined as

$$\delta := \frac{R_z - R_x}{R_0}, \tag{A.2}$$

where the spherical radius R_0 is defined as $R_0^3 := R_x R_y R_z$. We consider the case of axial symmetry $R_x = R_y$, then $R_0 = R_x^{2/3} R_z^{1/3}$. We call $\delta > 0$ "prolate shape" and $\delta < 0$ "oblate shape". [1] In the case of $|\delta| \ll 1$, we get

$$\begin{aligned} R_0 &= R_x + \frac{1}{3} R_0 \, \delta + O(\delta^2), \\ R_0 &= R_z - \frac{2}{3} R_0 \, \delta + O(\delta^2), \end{aligned} \tag{A.3}$$

thus,

$$\begin{aligned} R_x &= R_0 \left(1 - \frac{1}{3} \delta + O(\delta^2) \right), \\ R_z &= R_0 \left(1 + \frac{2}{3} \delta + O(\delta^2) \right). \end{aligned} \tag{A.4}$$

[1] The prolate and oblate shapes are not the same shape.

The deformation parameter a_{20} is now introduced as follows,

$$\begin{aligned} R(\theta) &= R_0 \left(1 + a_{20} Y_0^{(2)}(\theta, 0)\right) \\ &= R_0 \left(1 + a_{20} \sqrt{\frac{5}{16\pi}} \left(3\cos^2\theta - 1\right)\right), \end{aligned} \tag{A.5}$$

where θ is an angle from the positive z axis, and $R(\theta = 0)$ corresponds with R_z,

$$R_z = R(\theta = 0) = R_0 \left(1 + a_{20} \sqrt{\frac{5}{4\pi}}\right). \tag{A.6}$$

The parameter a_{20} represents the quadrupole deformation of the ellipsoid of inertia. By using Eqs. (A.4) and (A.6), the relation between a_{20} and δ is obtained,

$$a_{20} \approx \sqrt{\frac{16\pi}{45}}\, \delta \approx 1.06\, \delta. \tag{A.7}$$

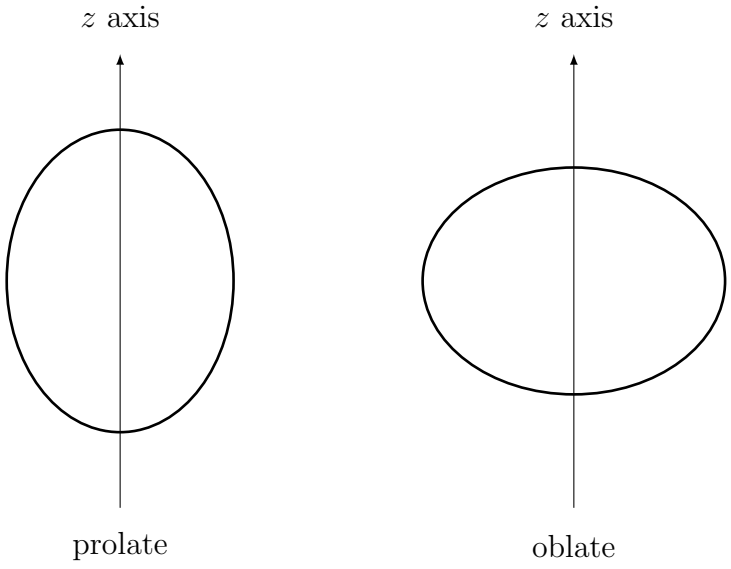

Figure A.1: Prolate and oblate shape.

A.2 Rigid-rotor value for moment of inertia of nuclei

In this section, the rigid-rotor value for the moment of inertia of nuclei is derived. The moment of inertia around y axis $\mathcal{I}$ is defined as

$$\mathcal{I} = \int_{0 \le \left(\frac{x}{R_x}\right)^2 + \left(\frac{y}{R_y}\right)^2 + \left(\frac{z}{R_z}\right)^2 \le 1} d^3r\, \rho(\mathbf{r})(x^2 + z^2), \tag{A.8}$$

where $\rho(\mathbf{r})$ is the mass density of the ellipsoid of inertia. Empirically, the stable nuclei have sharp surfaces, and their densities are almost constant values, $\rho \approx 0.16\,\mathrm{fm}^{-3}$. Thus, the volume of nuclei is proportional to the mass number A, $R \approx r_0 A^{1/3}$ with the radius R and $r_0 \approx 1.2\,\mathrm{fm}$. By using the saturation property for the density of nuclei,

$$\rho(\mathbf{r}) \approx \begin{cases} \dfrac{3AM}{4\pi R_0^3} (= \text{const.}), & 0 \leq \left(\dfrac{x}{R_x}\right)^2 + \left(\dfrac{y}{R_y}\right)^2 + \left(\dfrac{z}{R_z}\right)^2 \leq 1, \\ 0, & \text{otherwise}, \end{cases} \tag{A.9}$$

where M is the mass of nucleons, Eq. (A.8) is calculated as

$$\mathcal{I} = \frac{1}{5} AM(R_x^2 + R_z^2). \tag{A.10}$$

The moment of inertia of the ellipsoid in Eq. (A.10) does not depend on R_y. By assuming the axial symmetry $R_x = R_y$ and $|\delta| \ll 1$, Eq. (A.10) is approximated as

$$\mathcal{I} \approx \frac{2}{5} AMR_0^2 \left(1 + O(\delta)\right). \tag{A.11}$$

By using $R_0 \approx r_0 A^{1/3}$, and $r_0 \approx 1.2\,\mathrm{fm}$, the rigid-rotor value for the moment of inertia of nuclei is now derived,

$$\mathcal{I} \approx \frac{2}{5} r_0^2 M A^{5/3} \approx 0.0138 A^{5/3}. \tag{A.12}$$

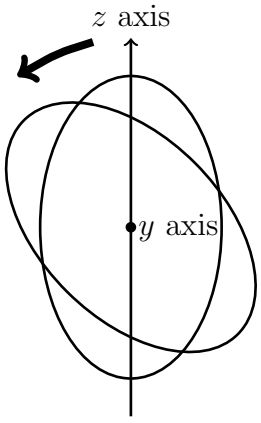

Figure A.2: Rotation of ellipsoid of inertia.

A.3 Rigid-rotor value for mass quadrupole moment of nuclei

In this section, the rigid-rotor value for the mass quadrupole moment of nuclei is derived. [2] The mass quadrupole moment for the ellipsoid of inertia with symmetry

[2]The mass quadrupole moment of nuclei could not be observed. The spectroscopic quadrupole moment in Eq. (4.67b) could be observed for nuclei experimentally.

around z axis in the rotating frame is defined as

$$Q_{\rm intrinsic} := \int_{0\leq\left(\frac{x}{R_x}\right)^2+\left(\frac{y}{R_y}\right)^2+\left(\frac{z}{R_z}\right)^2\leq 1} d^3r\,\rho(\mathbf{r})(3z^2-r^2). \tag{A.13}$$

By using the saturation property of the density of nuclei,

$$\rho(\mathbf{r}) \approx \begin{cases} \dfrac{3A}{4\pi R_0^3}(=\text{const.}), & 0 \leq \left(\dfrac{x}{R_x}\right)^2+\left(\dfrac{y}{R_y}\right)^2+\left(\dfrac{z}{R_z}\right)^2 \leq 1, \\ 0, & \text{otherwise}, \end{cases} \tag{A.14}$$

Eq. (A.13) is calculated as

$$Q_{\rm intrinsic} \approx \frac{1}{5}A(2R_z^2-R_x^2-R_y^2). \tag{A.15}$$

By using $R_x = R_y$, we get

$$Q_{\rm intrinsic} \approx \frac{2}{5}A(R_z^2-R_x^2). \tag{A.16}$$

From Eq. (A.16), $Q_{\rm intrinsic} > 0$ for the prolate shape, and $Q_{\rm intrinsic} < 0$ for the oblate shape. By using Eq. (A.4), Eq. (A.16) becomes

$$Q_{\rm intrinsic} \approx \frac{4}{5}AR_0^2\,\delta + O(\delta^2). \tag{A.17}$$

By using $R_0 \approx r_0 A^{1/3}$ and Eq. (A.7), the rigid-rotor value for the mass quadrupole moment of nuclei is now derived,

$$Q_{\rm intrinsic} \approx 1.09A^{5/3}a_{20}. \tag{A.18}$$

Appendix B

Projection operator with Wigner D-function

In this appendix, the projection operator on the angular-momentum eigenstates and its property are summarized with the Wigner D-function. An arbitrary three-dimensional rotation can be characterized by the Euler angles $\Omega = (\alpha, \beta, \gamma)$. The corresponding rotational operator $\hat{R}(\Omega)$ [67, 74] can be represented as

$$\hat{R}(\Omega) = e^{-i\hat{J}_z\alpha} e^{-i\hat{J}_y\beta} e^{-i\hat{J}_z\gamma}. \tag{B.1}$$

The matrix elements of the rotational operator $\hat{R}(\Omega)$ on the angular momentum eigenstates are well known as the Wigner D-function [3, 67, 74], which is defined,

$$\mathcal{D}^{(j)}_{mk}(\Omega) := \langle jm|\hat{R}(\Omega)|jk\rangle = e^{-i(m\alpha+k\gamma)} d^{(j)}_{mk}(\beta), \tag{B.2a}$$

$$d^{(j)}_{mk}(\beta) := \langle jm|e^{-i\hat{J}_y\beta}|jk\rangle, \tag{B.2b}$$

where $d^{(j)}_{mk}(\beta)$ is often called the Wigner (small) d-function. On the standard phase convention of the angular momentum, $d^{(j)}_{mk}(\beta)$ takes a real number. The Wigner D-function has the orthogonal property as follows:

$$\begin{aligned} \int d\Omega\, \mathcal{D}^{(j)*}_{mk}(\Omega)\mathcal{D}^{(j')}_{m'k'}(\Omega) &= \frac{16\pi^2}{2j+1}\delta_{jj'}\delta_{mm'}\delta_{kk'}, \\ \int d\Omega &:= \int_0^{2\pi} d\alpha \int_0^{\pi} d\beta \sin\beta \int_0^{4\pi} d\gamma. \end{aligned} \tag{B.3}$$

By using Eqs. (B.2) and (B.3), the generalized projection operator on the angular-momentum eigenstates is obtained, where we omit indices other than j, m, and k for simplicity,

$$\hat{P}^{(j)}_{mk} := |jm\rangle\langle jk| = \frac{2j+1}{16\pi^2} \int d\Omega\, \mathcal{D}^{(j)*}_{mk}(\Omega)\hat{R}(\Omega). \tag{B.4}$$

Equation (B.4) satisfies the following equations,

$$(\hat{P}^{(j)}_{mk})^\dagger = \hat{P}^{(j)}_{km}, \tag{B.5a}$$

$$(\hat{P}^{(j)}_{mk})^2 = \delta_{mk}\hat{P}^{(j)}_{mk}. \tag{B.5b}$$

The states which have the integer and the half-integer angular momentum do not mix practically, then the γ integration in Eq. (B.4) could be halved.

By using Eqs. (B.1) and (B.4), the generalized projection operator can be decomposed into the product of three operators as

$$\hat{P}^{(j)}_{mk} = \hat{P}_m \hat{P}^j_{mk} \hat{P}_k, \tag{B.6a}$$

where,

$$\hat{P}^j_{mk} := \frac{2j+1}{2} \int_0^\pi d\beta \sin\beta \, d^{(j)}_{mk}(\beta) \, e^{-i\hat{J}_y \beta}, \tag{B.7a}$$

$$\hat{P}_m := \frac{1}{2\pi} \int_0^{2\pi} d\alpha \, e^{-i(\hat{J}_z - m)\alpha}. \tag{B.7b}$$

Note that $\hat{P}^j_{mk}$ is not the projection operator if $m \neq k$.

By using the group property for the rotational operator $\hat{R}(\Omega)$, a spherical tensor $\hat{T}^{(\lambda)}_\mu$ satisfies the following equation [3, 17]:

$$(\hat{P}^{(j')}_{m'k'})^\dagger \hat{T}^{(\lambda)}_\mu \hat{P}^{(j)}_{mk} = \langle j\lambda m\mu | (j\lambda) j'm' \rangle \sum_{m''\mu'} \langle j\lambda m''\mu' | (j\lambda) j'k' \rangle \, \hat{T}^{(\lambda)}_{\mu'} \hat{P}^{(j)}_{m''k} \, . \tag{B.8}$$

Appendix C

Kamlah expansion

In this appendix, the Kamlah expansion [3,13,15] is introduced, which enables to derive not only the $J(J+1)$ rule but also the cranking model based on the AMP. The axial symmetry and the time-reversal symmetry for the intrinsic state $|\Phi\rangle$ are not assumed here. [1] If the intrinsic state is deformed well, the integrand in the projection operator could be expressed by the following exponential form with an integral for a single Euler angle, [2] then the energy could be expanded as follows:

$$\langle J|\hat{H}|J\rangle \approx \frac{\int_{\alpha\approx 0} d\alpha \, \langle\Phi|\hat{H}e^{-i(\hat{J}_x-\sqrt{J(J+1)})\alpha}|\Phi\rangle}{\int_{\alpha\approx 0} d\alpha \, \langle\Phi|e^{-i(\hat{J}_x-\sqrt{J(J+1)})\alpha}|\Phi\rangle} \tag{C.1a}$$

$$\approx \sum_{n=0}^{n_{\max}} h_n \left(\sqrt{J(J+1)} - \langle\Phi|\hat{J}_x|\Phi\rangle\right)^n . \tag{C.1b}$$

The value h_n in Eq. (C.1b) is determined step by step from $n = n_{\max}$ to $n = 0$ via

$$\langle\Phi|\hat{H}e^{-i\hat{J}_x\alpha}|\Phi\rangle \approx \sum_{n=0}^{n_{\max}} h_n \left(-\langle\Phi|\hat{J}_x|\Phi\rangle + \frac{1}{i}\frac{\partial}{\partial\alpha}\right)^n \langle\Phi|e^{-i\hat{J}_x\alpha}|\Phi\rangle , \tag{C.2}$$

with the Gaussian approximation,

$$\langle\Phi|e^{-i\hat{J}_x\alpha}|\Phi\rangle \approx \exp\left(i\langle\Phi|\hat{J}_x|\Phi\rangle\,\alpha - \frac{1}{2}(\sigma[\hat{J}_x])^2\alpha^2\right), \tag{C.3}$$

where $\sigma[\hat{J}_x]$ is the fluctuation of $\hat{J}_x$ for the state $|\Phi\rangle$. By taking $n_{\max} = 2$, we get

$$\begin{aligned}\langle J|\hat{H}|J\rangle \approx & h_0 + h_1\left(\sqrt{J(J+1)} - \langle\Phi|\hat{J}_x|\Phi\rangle\right) + h_2\left(\sqrt{J(J+1)} - \langle\Phi|\hat{J}_x|\Phi\rangle\right)^2 , \\ h_0 = & \langle\Phi|\hat{H}|\Phi\rangle - \frac{C[\hat{H},(\Delta\hat{J}_x)^2]}{(\sigma[\hat{J}_x])^2}, \qquad h_1 = \frac{C[\hat{H},\hat{J}_x]}{(\sigma[\hat{J}_x)^2}, \qquad h_2 = \frac{C[\hat{H},(\Delta\hat{J}_x)^2]}{2(\sigma[\hat{J}_x])^4},\end{aligned} \tag{C.4}$$

[1] The intrinsic state could have the time-reversal symmetry if the axial symmetry is broken. The ground-state rotational band will be mainly composed of the axially-symmetric intrinsic states. It is well-known that the ground-state of many even-even nuclei have the pair correlations associated with the time-reversal symmetry. Therefore, it is considered that effects of breaking the time-reversal symmetry could be important for high angular momentum in the rotational band.

[2] We have reduced the three-dimensional integral of the projection operator in Eq. (B.4) by the one-dimensional integral for simplicity.

where $\Delta\hat{J}_x := \hat{J}_x - \langle\Phi|\hat{J}_x|\Phi\rangle$, and $C[\hat{H}, (\Delta\hat{J}_x)^2]$ is the correlation function between $\hat{H}$ and $(\Delta\hat{J}_x)^2$ for the state $|\Phi\rangle$, and so on. Equation (C.4) indicates that the $J(J+1)$ rule of the ground-state rotational energy could be influenced by the intrinsic state which has neither the axial symmetry nor the time-reversal symmetry. By neglecting the h_2 term and the second term in h_0 in Eq. (C.4) and taking the first variation for Eq. (C.4), the cranking equation is derived:

$$\begin{aligned} &\delta\,\langle\Phi|\hat{H}|\Phi\rangle - \omega\,\delta\,\langle\Phi|\hat{J}_x|\Phi\rangle = 0, \\ &\langle\Phi|\hat{J}_x|\Phi\rangle = \sqrt{J(J+1)}, \end{aligned} \tag{C.5}$$

where h_1 is regarded as a constant value ω, $h_1 = \omega$. The effect accompanied by breaking both the axial symmetry and the time-reversal symmetry with Eq. (C.5) is often called the cranking effect. If the intrinsic state has the axial symmetry, $\langle\Phi_0|\hat{J}_x|\Phi_0\rangle = 0$, and $h_1 = \omega = 0$, then the $J(J+1)$ rule with $2h_2 = \mathcal{I}_Y^{-1}$ in Eq. (4.25) is reproduced.

In this study, the axial and the time-reversal symmetry are assumed for the intrinsic states in the theory and numerical calculations of AMP, as explained in Sec. 6.3.

Appendix D

Moment of inertia derived from cranking model and RPA

In this appendix, the Inglis formula [4], the Belyaev formula [5], and the TV formula [6] is introduced as the moment of inertia derived from the cranking model and the RPA. As we have seen in Sec. 4.3, the cranking model is approximately connected to the AMP for the well-deformed intrinsic state, which may have neither axial symmetry nor time-reversal symmetry. The cranking Hamiltonian is

$$\hat{H}' = \hat{H} - \omega \hat{J}_x, \tag{D.1}$$

where the parameter ω is the angular velocity. By taking the term $-\omega \hat{J}_x$ in Eq. (D.1) as the perturbation, the Inglis formula [4] is derived with the restriction that the ground state is the HF vacuum $|\mathrm{HF}\rangle$, and the excited states are the one-particle one-hole (1p1h) states $a_p^\dagger a_h |\mathrm{HF}\rangle$,

$$\begin{aligned} \langle \Psi | \hat{J}_x | \Psi \rangle &\approx \langle \mathrm{HF} | \hat{J}_x | \mathrm{HF} \rangle + \omega \mathcal{I}^{(\mathrm{Inglis})}, \\ \mathcal{I}^{(\mathrm{Inglis})} &:= 2 \sum_{ph} \frac{|\langle p | \hat{J}_x | h \rangle|^2}{\varepsilon_p - \varepsilon_h}, \end{aligned} \tag{D.2}$$

where $|p\rangle$ ($|h\rangle$) is the particle (hole) state, and ε_p and ε_h is the single-particle energy.

The Belyaev formula [5] is derived similarly by using the BCS vacuum $|\mathrm{BCS}\rangle$ and two quasi-particle (q.p.) states $\alpha_i^\dagger \alpha_{i'}^\dagger |\mathrm{BCS}\rangle$, $i > 0$ and $i' < 0$. According to the HFB theory, the Belyaev formula can be generalized with the HFB vacuum $|\mathrm{HFB}\rangle$ and two quasi-particle (q.p.) states $\alpha_i^\dagger \alpha_{i'}^\dagger |\mathrm{HFB}\rangle$, $i > 0$ and $i' < 0$ as

$$\begin{aligned} \langle \Psi | \hat{J}_x | \Psi \rangle &\approx \langle \mathrm{HFB} | \hat{J}_x | \mathrm{HFB} \rangle + \omega \mathcal{I}^{(\mathrm{Belyaev})}, \\ \mathcal{I}^{(\mathrm{Belyaev})} &:= 2 \sum_{i>0,\, i'<0} \frac{|\langle i | \hat{J}_x | i' \rangle|^2 (u_i v_{i'} - u_{i'} v_i)^2}{\varepsilon_i + \varepsilon_{i'}}, \end{aligned} \tag{D.3}$$

where ε_i is the quasi-particle energy, $|i\rangle$ is the canonical bases, and u_i and v_i are the coefficient of the Bogoliubov transformation [see Sec. 6.2]. Because of the presence of $0 \leq |u_i| \leq 1$ and $0 \leq |v_i| \leq 1$, the denominator in Eq. (D.3) is larger than that in Eq. (D.2), and the numerator in Eq. (D.3) is smaller than that in Eq. (D.2). Therefore, the pair correlations reduce the moment of inertia $\mathcal{I}$.

The TV formula [6] is derived in the RPA [3]. We introduce more modern derivation based on Refs. [85, 98]. Considering the 1p1h correlations based on the HF vacuum, the RPA equation is obtained with the stability matrix S for the HF state [3],

$$\mathsf{S}\boldsymbol{x}_\nu = \omega_\nu \mathsf{N}\boldsymbol{x}_\nu, \quad \mathsf{S} := \begin{pmatrix} \mathsf{A} & \mathsf{B} \\ \mathsf{B}^* & \mathsf{A}^* \end{pmatrix}, \quad \mathsf{N} := \begin{pmatrix} 1 & 0 \\ 0 & -1 \end{pmatrix}, \quad \boldsymbol{x}_\nu := \begin{pmatrix} X^{(\nu)} \\ Y^{(\nu)} \end{pmatrix}, \tag{D.4}$$

with the normalization condition $\boldsymbol{x}_\nu^\dagger \mathsf{N}\boldsymbol{x}_\nu = 1$. According to $\mathsf{A} = \mathsf{A}^\dagger$ and $\mathsf{B} = \mathsf{B}^{\mathrm{T}}$, the stability matrix S is hermitian, $\mathsf{S} = \mathsf{S}^\dagger$. The TV formula considers the ground-state correlations, where the ground state changes from the HF vacuum by the 1p1h excitations. If $\mathsf{B} = \mathsf{0}$, then $Y^{(\nu)} = \mathbf{0}$ for all ν, and the RPA corresponds with the Tamm-Dancoff approximation (TDA) [3]. We express the matrix elements of $\hat{J}_x$ for the s.p. states obtained by the HF calculation as $p_{ii'} := \langle i|\hat{J}_x|i'\rangle$. We here consider that the rotational symmetry is spontaneously broken in the HF state, $\hat{J}_x\,|\mathrm{HF}\rangle \neq 0$. For the NG mode, the following RPA equation is satisfied for the HF state with the stability matrix S,

$$\mathsf{S}\boldsymbol{p} = \mathbf{0}, \quad \boldsymbol{p} := \begin{pmatrix} p_{\mathrm{ph}} \\ -p_{\mathrm{ph}}^* \end{pmatrix}. \tag{D.5}$$

From Eq. (D.5), $\det \mathsf{S} = 0$, though S is positive semi-definite. If $\boldsymbol{p}$ belongs to by the doubly self-dual Jordan block [85, 98] where the dimension of the Jordan Block is 2, the canonical variables $\boldsymbol{q}$ are constructed as follows:

$$^\exists\boldsymbol{q} \text{ such that } \mathsf{S}\boldsymbol{q} = i\zeta \boldsymbol{q}^\dagger \mathsf{N}\boldsymbol{p}, \tag{D.6}$$

where $\zeta > 0$, and the normalization condition is $\boldsymbol{q}\mathsf{N}\boldsymbol{p} = -i$. The moment of inertia $\mathcal{I}^{(\mathrm{TV})}$ is defined as $\mathcal{I}^{(\mathrm{TV})} := \zeta^{-1}$, then

$$\frac{1}{\mathcal{I}^{(\mathrm{TV})}} = \boldsymbol{q}^\dagger \mathsf{S}\boldsymbol{q}. \tag{D.7}$$

The TV formula for the moment of inertia is now derived. The TV formula is also represented as [3]

$$\begin{aligned} \langle\Psi|\hat{J}_x|\Psi\rangle &= \langle \mathrm{HF}|\hat{J}_x|\mathrm{HF}\rangle + \omega\mathcal{I}^{(\mathrm{TV})}, \\ \mathcal{I}^{(\mathrm{TV})} &= 2\sum_{pp'hh'} \frac{\langle h|\hat{J}_x|p\rangle\ \langle p'|\hat{J}_x|h'\rangle}{\delta_{pp'}\delta_{hh'}(\varepsilon_p - \varepsilon_h) + \bar{v}_{ph'hp'} + \bar{v}_{pp'hh'}}. \end{aligned} \tag{D.8}$$

where $\bar{v}_{ph'hp'}$ and $\bar{v}_{pp'hh'}$ are the residual interactions connected with the HF vacuum. In the case of the TDA, $\bar{v}_{pp'hh'}$ is neglected. If the residual interactions of the TV formula in Eq. (D.8) are neglected, the Inglis formula in Eq. (D.2) is obtained. The TV formula for the QRPA is extended straightforwardly, which reduces to the Belyaev formula in Eq. (D.3) if the residual interactions are neglected.

We compare the moment of inertia derived from the cranking model and the RPA with the AMP in Eq. (4.18). The TV formula in the RPA (QRPA) connected with the HF (HFB) vacuum includes the Inglis formula (the Belyaev formula). Thus, it is considered that the cranking effect is included in the TV formula, accompanied by the intrinsic state, which neither has axial symmetry nor time-reversal symmetry. Indeed,

the rotation of the intrinsic state around the x axis breaks the axial symmetry. The TV formula considers only small amplitude of corresponding NG mode, while the AMP in Eq. (4.18) could also consider large amplitude. The state $e^{-i\hat{J}_y\beta}|\Phi_0\rangle$ does not have the axial symmetry but keeps the time-reversal symmetry. Since the RPA considers only 1p1h excitations, the TV formula in Eq. (D.7) could have a different value from the moment of inertia calculated by the AMP in Eq. (4.18), in general.

In this study, the AMP has been used in order to analyze the rotational energy near the ground-states of even-even nuclei.

Appendix E

Cumulant expansion

In this appendix, the cumulant expansion [75] is summarized. In the following, the bracket $\langle\,\rangle$ represents a general expectation value. The cumulant of operators $\hat{X}_1$, $\hat{X}_2$, …, $\hat{X}_n$ is defined as

$$\langle \hat{X}_1; \cdots ; \hat{X}_n \rangle_{\rm cum} := \frac{\partial}{\partial t_1} \cdots \frac{\partial}{\partial t_n} \ln \left\langle \exp\left(\sum_{i=1}^{n} t_i \hat{X}_i \right) \right\rangle \Bigg|_{t_1=\cdots=t_n=0} , \tag{E.1}$$

where $[\hat{X}_i, \hat{X}_j] = 0$ for all i and j. For instance,

$$\begin{aligned} \langle \hat{X}_1 \rangle_{\rm cum} &= \langle \hat{X}_1 \rangle \,, \\ \langle \hat{X}_1; \hat{X}_2 \rangle_{\rm cum} &= \langle \hat{X}_1 \hat{X}_2 \rangle - \langle \hat{X}_1 \rangle \, \langle \hat{X}_2 \rangle =: C[\hat{X}_1, \hat{X}_2], \end{aligned} \tag{E.2}$$

in particular, $(\sigma[\hat{X}_1])^2 := \langle \hat{X}_1^2 \rangle - \langle \hat{X}_1 \rangle^2 = \langle \hat{X}_1; \hat{X}_1 \rangle_{\rm cum}$. In the case of $\hat{X} := \hat{X}_i$ for all i, and $t = \sum_{i=1}^{n} t_i$, we get

$$\langle \underbrace{\hat{X}; \cdots ; \hat{X}}_{n} \rangle_{\rm cum} = \frac{\partial^n}{\partial t^n} \ln \langle e^{t\hat{X}} \rangle \Big|_{t=0} , \tag{E.3}$$

then,

$$\ln \langle e^{t\hat{X}} \rangle = \sum_{n=1}^{\infty} \frac{t^n}{n!} \langle \underbrace{\hat{X}; \cdots ; \hat{X}}_{n} \rangle_{\rm cum} \,. \tag{E.4}$$

We also get the following equations,

$$\begin{aligned} \frac{\langle \hat{X}_1 e^{t\hat{X}_2} \rangle}{\langle e^{t\hat{X}_2} \rangle} &= \sum_{n=0}^{\infty} \frac{t^n}{n!} \frac{\partial}{\partial t_1} \frac{\partial^n}{\partial t_2^n} \ln \langle e^{t_1\hat{X}_1 + t_2\hat{X}_2} \rangle \Big|_{t_1=t_2=0} \\ &= \sum_{n=0}^{\infty} \frac{t^n}{n!} \langle \hat{X}_1; \underbrace{\hat{X}_2; \cdots ; \hat{X}_2}_{n} \rangle_{\rm cum} \,, \end{aligned} \tag{E.5}$$

$$\begin{aligned} \frac{\langle \hat{X}_1 e^{t\hat{X}_2} e^{u\hat{X}_3} \rangle}{\langle e^{t\hat{X}_2} e^{u\hat{X}_3} \rangle} &= \sum_{n=0}^{\infty} \sum_{m=0}^{\infty} \frac{t^n \, u^m}{n! \, m!} \frac{\partial}{\partial t_1} \frac{\partial^n}{\partial t_2^n} \frac{\partial^m}{\partial t_3^m} \ln \langle e^{t_1\hat{X}_1 + t_2\hat{X}_2 + t_3\hat{X}_3} \rangle \Big|_{t_1=t_2=t_3=0} \\ &= \sum_{n=0}^{\infty} \sum_{m=0}^{\infty} \frac{t^n \, u^m}{n! \, m!} \langle \hat{X}_1; \underbrace{\hat{X}_2; \cdots ; \hat{X}_2}_{n}; \underbrace{\hat{X}_3; \cdots ; \hat{X}_3}_{m} \rangle_{\rm cum} \,, \end{aligned} \tag{E.6}$$

and so on.

Appendix F

Gaussian approximation connected to AMP

In this appendix, the Gaussian approximation [3, 8, 11, 13] for the rotational energy in Sec. 4.4 is discussed with higher-s_{2n} terms in Eq. (4.35). There are certain cases that the overlap function $\langle\Phi_0|e^{-i\hat{J}_y\beta}|\Phi_0\rangle$ is well approximated by the Gaussian function as

$$\langle\Phi_0|e^{-i\hat{J}_y\beta}|\Phi_0\rangle = 1 - \frac{1}{2}\langle\Phi_0|\hat{J}_y^2|\Phi_0\rangle\,\beta^2 + \cdots \approx e^{-\frac{1}{2}(\sigma[\hat{J}_y])^2\beta^2}. \tag{F.1}$$

The width $(\sigma[\hat{J}_y])^{-1}$ is not always narrow. For $x > 0$, the following functions are defined as

$$N_{2n}^{(\mathrm{G})}(x) := \int_0^{\pi/2} d\beta \sin\beta\,\beta^{2n} e^{-\frac{1}{2}x\beta^2}, \tag{F.2a}$$

$$\Lambda_{2n}^{(\mathrm{G})}(x) := \frac{N_{2n}^{(\mathrm{G})}(x)}{N_0^{(\mathrm{G})}(x)}, \tag{F.2b}$$

analogously to Eq. (4.30). The function $\Lambda_2^{(\mathrm{G})}(x)$ is called universal function in Ref. [99].

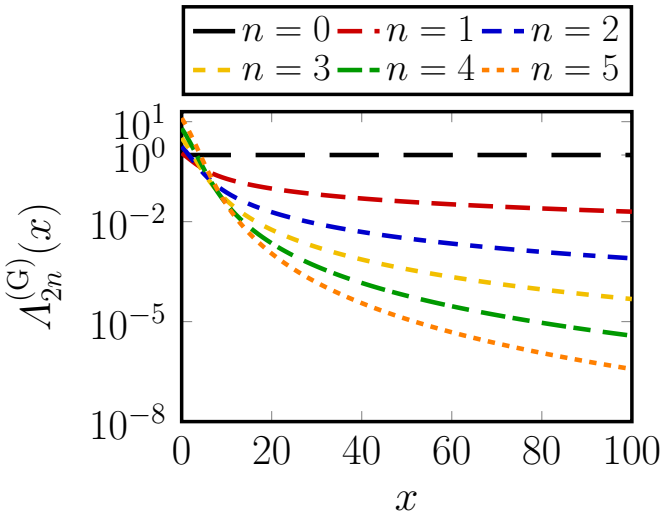

Figure F.1: $\Lambda_{2n}^{(\mathrm{G})}(x)$ for $n = 0, \ldots, 5$.

In Fig. F.1, $\Lambda_{2n}^{(\mathrm{G})}(x)$ in Eq. (F.2b) is shown. For small n and large x, the following relation is satisfied,

$$\Lambda_{2n}^{(\mathrm{G})}(x) > \Lambda_{2n+2}^{(\mathrm{G})}(x). \tag{F.3}$$

The recurrence relations of $N_{2n}^{(\mathrm{G})}(x)$ and $\Lambda_{2n}^{(\mathrm{G})}(x)$ are

$$\frac{d}{dx} N_{2n}^{(\mathrm{G})}(x) = -\frac{1}{2} N_{2n+2}^{(\mathrm{G})}(x), \tag{F.4a}$$

$$\frac{d}{dx} \Lambda_{2n}^{(\mathrm{G})}(x) = -\frac{1}{2} \left[\Lambda_{2n+2}^{(\mathrm{G})}(x) - \Lambda_{2n}^{(\mathrm{G})}(x) \Lambda_{2}^{(\mathrm{G})}(x) \right]. \tag{F.4b}$$

Equations (4.32) and (4.37) are approximated as

$$\langle 0|\hat{\mathcal{S}}|0\rangle \approx \sum_{n=0}^{\infty} s_{2n} \Lambda_{2n}^{(\mathrm{G})}(x) \Big|_{x=(\sigma[\hat{J}_y])^2}, \tag{F.5a}$$

$$\frac{1}{\mathcal{I}[\hat{\mathcal{S}}]} \approx \sum_{n=1}^{\infty} s_{2n} \frac{d}{dx} \Lambda_{2n}^{(\mathrm{G})}(x) \Big|_{x=(\sigma[\hat{J}_y])^2}, \tag{F.5b}$$

regardless of the value of $(\sigma[\hat{J}_y])^2$.

If the width of the Gaussian $(\sigma[\hat{J}_y])^{-1}$ is narrow enough, $N_{2n}^{(\mathrm{G})}(x)$ is approximated by taking $\sin\beta \approx \beta$ in Eq. (F.2a),

$$N_{2n}^{(\mathrm{G})}(x) \approx \int_0^{\pi/2} d\beta\, \beta^{2n+1} e^{-\frac{1}{2}x\beta^2} = 2^n \int_0^{\lambda} du\, u^n e^{-xu}, \tag{F.6}$$

where $\lambda := \pi^2/8$. The integral of Eq. (F.6) is a generalization of the gamma function $\Gamma(n+1)$, which corresponds with $\Gamma(n+1)$ in the case of $x = 1$ and $\lambda \to \infty$. The recurrence relation in Eq. (F.4a) is satisfied for the approximate $N_{2n}^{(\mathrm{G})}(x)$ in Eq. (F.6). For $n = 0$, the integration in Eq. (F.6) can be done analytically,

$$N_0^{(\mathrm{G})}(x) \approx \frac{1}{x}(1 - e^{-\lambda x}). \tag{F.7}$$

By using Eqs. (F.4a) and (F.7), an analytical expression of $N_{2n}^{(\mathrm{G})}(x)$ is obtained,

$$N_{2n}^{(\mathrm{G})}(x) \approx \frac{2^n n!}{x^{n+1}} \left(1 - e^{-\lambda x} \sum_{m=0}^{n} \frac{(\lambda x)^m}{m!} \right), \tag{F.8}$$

and then,

$$\Lambda_{2n}^{(\mathrm{G})}(x) \approx \frac{2^n n!}{x^n} \frac{1 - e^{-\lambda x} \sum_{m=0}^{n} \frac{(\lambda x)^m}{m!}}{1 - e^{-\lambda x}}. \tag{F.9}$$

By widening the range of integral $\pi/2 \to \infty$ (i.e., $\lambda \to \infty$) in Eq. (F.6), the following equation is obtained:

$$N_{2n}^{(\mathrm{G})}(x) \approx \frac{2^n n!}{x^{n+1}} \tag{F.10}$$

and

$$\Lambda_{2n}^{(\mathrm{G})}(x) \approx \frac{2^n n!}{x^n}. \tag{F.11}$$

Equation (F.11) satisfies Eq. (F.3) for small n and large x. Although Eq. (F.3) breaks down at extremely large n for any x, c_{2n} in Eq. (4.26b) eases a problem of convergence in Eq. (4.31) via

$$\langle J0|(\hat{J}_+ - \hat{J}_-)^{2n}|J0\rangle \sim \binom{2n}{n} (-)^n J^{2n} \tag{F.12}$$

and

$$c_{2n}\,\Lambda_{2n}^{(\mathrm{G})} \sim \frac{1}{n!}\left(-\frac{J^2}{2x}\right)^n. \tag{F.13}$$

If we neglect higher-s_{2n} terms in Eq. (F.5), $\langle 0|\hat{\mathcal{S}}|0\rangle$ and $\mathcal{I}[\hat{\mathcal{S}}]$ are approximated by using Eq. (F.11),

$$\langle 0|\hat{\mathcal{S}}|0\rangle \approx \langle \Phi_0|\hat{\mathcal{S}}|\Phi_0\rangle - \frac{C[\hat{\mathcal{S}}, \hat{J}_y^2]}{(\sigma[\hat{J}_y])^2}, \tag{F.14a}$$

$$\frac{1}{\mathcal{I}[\hat{\mathcal{S}}]} \approx \frac{C[\hat{\mathcal{S}}, \hat{J}_y^2]}{(\sigma[\hat{J}_y])^4}. \tag{F.14b}$$

Equation (F.14) is the result of the Kamlah expansion in Eq. (C.4) with axial symmetry, and Eq. (F.14b) is the Yoccoz moment of inertia in Eq. (4.25).

Appendix G

Pair-distribution function

In this appendix, the pair-distribution function is introduced. We define the local density operator as

$$\hat{\rho}(x) := \psi^\dagger(x)\psi(x), \quad x = (\mathbf{r}\sigma\tau). \tag{G.1}$$

We have defined the creation (annihilation) operator for the spinor field as $\psi^\dagger(x)(\psi(x))$. They satisfy the following fermionic anticommutation relations:

$$\{\psi(x_1), \psi^\dagger(x_2)\} = \delta(x_1 - x_2), \quad \{\psi(x_1), \psi(x_2)\} = 0, \quad \{\psi^\dagger(x_1), \psi^\dagger(x_2)\} = 0, \tag{G.2}$$

where $\delta(x_1 - x_2) := \delta(\mathbf{r}_1 - \mathbf{r}_2)\delta_{\sigma_1\sigma_2}\delta_{\tau_1\tau_2}$. The pair-distribution function is defined as

$$g(x_1, x_2) := \frac{\langle\hat{\rho}(x_1)\hat{\rho}(x_2)\rangle - \langle\hat{\rho}(x_1)\rangle\,\delta(x_1 - x_2)}{\langle\hat{\rho}(x_1)\rangle\,\langle\hat{\rho}(x_2)\rangle} \tag{G.3a}$$

$$= \frac{\langle\psi^\dagger(x_1)\psi^\dagger(x_2)\psi(x_2)\psi(x_1)\rangle}{\langle\hat{\rho}(x_1)\rangle\,\langle\hat{\rho}(x_2)\rangle}. \tag{G.3b}$$

By definition, $g(x_1, x_2) = 0$ for $x_1 = x_2$, and $g(x_1, x_2) \geq 0$. If $\langle\hat{\rho}(x_1)\hat{\rho}(x_2)\rangle \approx \langle\hat{\rho}(x_1)\rangle\,\langle\hat{\rho}(x_2)\rangle$ with $x_1 \neq x_2$ (*e.g.*, $|\mathbf{r}_1 - \mathbf{r}_2| \to \infty$), $\sigma_1 \neq \sigma_2$, or $\tau_1 \neq \tau_2$, then $g(x_1, x_2) \approx 1$. If the state is an arbitrary vacuum, the Wick's theorem could be applied for the RHS of Eq. (G.3b), then we get

$$g(x_1, x_2) = 1 - \frac{|\,\langle\psi^\dagger(x_2)\psi(x_1)\rangle\,|^2}{\langle\hat{\rho}(x_1)\rangle\,\langle\hat{\rho}(x_2)\rangle} + \frac{|\,\langle\psi(x_2)\psi(x_1)\rangle\,|^2}{\langle\hat{\rho}(x_1)\rangle\,\langle\hat{\rho}(x_2)\rangle}. \tag{G.4}$$

For the HF vacuum, the third term in the RHS of Eq. (G.4) vanishes, then $g(x_1, x_2) \leq 1$. Therefore, the pair-distribution function could be interpreted as the probability density of the existence of two particles at $\mathbf{r}_1$ and $\mathbf{r}_2$ simultaneously. On the other hand, for the HFB vacuum, where there are the pair correlations, the third term in the RHS of Eq. (G.4) does not vanish and increases the pair distribution function.

The pair-distribution function is related to the correlation function between the local density operators, which is defined as

$$\begin{aligned} C[\hat{\rho}(x_1), \hat{\rho}(x_2)] &:= \langle\hat{\rho}(x_1)\hat{\rho}(x_2)\rangle - \langle\hat{\rho}(x_1)\rangle\,\langle\hat{\rho}(x_2)\rangle \\ &= (g(x_1, x_2) - 1)\,\langle\hat{\rho}(x_1)\rangle\,\langle\hat{\rho}(x_2)\rangle + \langle\hat{\rho}(x_1)\rangle\,\delta(x_1 - x_2). \end{aligned} \tag{G.5}$$

If the state is an arbitrary vacuum, the Wick's theorem can be applied for Eq. (G.5) as

$$C[\hat{\rho}(x_1), \hat{\rho}(x_2)] = \langle \hat{\rho}(x_1) \rangle \, \delta(x_1 - x_2) - | \langle \psi^\dagger(x_2) \psi(x_1) \rangle |^2 + | \langle \psi(x_2) \psi(x_1) \rangle |^2. \quad \text{(G.6)}$$

The third term in the RHS of Eq. (G.6) vanishes for the HF vacuum. Then, if $x_1 \neq x_2$, $C[\hat{\rho}(x_1), \hat{\rho}(x_2)] \leq 0$. On the other hand, for the HFB vacuum, where there are the pair correlations, the third term in the RHS of Eq. (G.6) does not vanish and increases $C[\hat{\rho}(x_1), \hat{\rho}(x_2)]$. Therefore, the two particles get spatially close to each other by the pair correlations. This phenomenon is called the pair condensation.

In this study, the expectation value of the two-body delta function in Eq. (5.1) has been used for the spatial correlations between nucleons associated with contributions of the interactions for the rotational energy of nuclei, as noticed in Chap. 5. The expectation value of the two-body delta function is approximately related to the pair-distribution function, as noticed in Eq. (5.3).

Appendix H

Proof for non-negativity of overlap function

In this appendix, the non-negativity of the overlap function is proven for the HF states with time-reversal symmetry [39].

We define a $A \times A$ square matrix G for a HF state $|\Phi\rangle$ whose elements are $\langle i'|\hat{R}(\Omega)|i\rangle$, where i denotes the occupied s.p. state obtained by the HF calculation, i.e., $|\Phi(q)\rangle = \prod_{i=1}^{A} a_i^\dagger |0\rangle_c$. [1] The rotational operator $\hat{R}(\Omega)$ is defined in Eq. (B.1). We then have $\langle\Phi(q')|\hat{R}(\Omega)|\Phi(q)\rangle = \det(\mathsf{G})$. If $\hat{\mathcal{T}}|\Phi(q)\rangle = |\Phi(q)\rangle$ ($\hat{\mathcal{T}}$ is the time-reversal operator), $|\Phi(q)\rangle$ contains time-reversal partners $|i\rangle$ and $|\bar{i}\rangle$, which satisfy $\langle\bar{i'}|\hat{R}(\Omega)|\bar{i}\rangle = \langle i'|\hat{R}(\Omega)|i\rangle^*$ and $\langle\bar{i'}|\hat{R}(\Omega)|i\rangle = -\langle i'|\hat{R}(\Omega)|\bar{i}\rangle^*$ ($\because\ \hat{\mathcal{T}}\hat{R}(\Omega)\hat{\mathcal{T}}^{-1} = \hat{R}(\Omega)$). [2] Thus G has the following structure:

$$\mathsf{G} = \begin{pmatrix} \mathsf{A} & -\mathsf{B} \\ \mathsf{B}^* & \mathsf{A}^* \end{pmatrix}. \tag{H.1}$$

It is proven that the structure of Eq. (H.1) ensures $\det(\mathsf{G}) \geq 0$ as follows.

The structure of Eq. (H.1) derives the property

$$\Sigma_y \mathsf{G} \Sigma_y = \mathsf{G}^*, \quad \Sigma_y := \begin{pmatrix} 0 & -i \\ i & 0 \end{pmatrix}. \tag{H.2}$$

For the ν th eigenvalue and eigenvector of G,

$$\mathsf{G}\boldsymbol{x}_\nu = \lambda_\nu \boldsymbol{x}_\nu\,, \tag{H.3}$$

there always exists a partner

$$\mathsf{G}(\Sigma_y \boldsymbol{x}_\nu^*) = \lambda_\nu^*(\Sigma_y \boldsymbol{x}_\nu^*)\,, \tag{H.4}$$

because of Eq. (H.2). Even when $\lambda_\nu = \lambda_\nu^*$, the eigenvectors are linearly independent because $(\Sigma_y \boldsymbol{x}_\nu^*)^\dagger \boldsymbol{x}_\nu = \boldsymbol{x}_\nu^{\mathrm{T}} \Sigma_y \boldsymbol{x}_\nu = 0$. While a matrix with the property (H.2) is

[1] The parameter q represents the generator coordinate [3].

[2] Although the rotational operator $\hat{R}(\Omega)$ is assumed here, only the property $[\hat{R}(\Omega), \hat{\mathcal{T}}] = 0$ is used. Thus, the following statement can be generalized for an arbitrary unitary operator $\hat{\mathcal{U}}$ which commutes with the time-reversal operator $\hat{\mathcal{T}}$.

not necessarily diagonalizable, the Jordan blocks associated by λ_ν and λ_ν^* have equal dimensions, as were given in the duality argument in Ref. [85]. It is now proven

$$\det(\mathsf{G}) = \prod_\nu |\lambda_\nu|^2 \geq 0\,. \tag{H.5}$$

The non-negativity of matrices with the property (H.1) was proven for quaternion matrices in Refs. [100, 101].

Bibliography

[1] A. Bohr and B. R. Mottelson, *Nuclear Structure*, Vols. I, II (World Scientific, Singapore, 1998).

[2] National Nuclear Data Center, `https://www.nndc.bnl.gov/`.

[3] P. Ring and P. Schuck, *The Nuclear Many-Body Problem* (Springer-Verlag, Berlin, 1980).

[4] D. R. Inglis, Phys. Rev. **96**, 1059 (1954); **97**, 701 (1955).

[5] S. T. Belyaev, Mat. Fys. Medd. Dan. Vid. Selsk. **31**, No. 11 (1959).

[6] D. J. Thouless and J. G. Valatin, Nucl. Phys. **31**, 211 (1962).

[7] R. E. Peierls and J. Yoccoz, Proc. Phys. Soc. London, Sect. A **70**, 381 (1957).

[8] J. Yoccoz, Proc. Phys. Soc. London, Sect. A **70**, 388 (1957).

[9] R. E. Peierls and D. J. Thouless, Nucl. Phys. **38**, 154 (1962).

[10] B. J. Verhaar, Nucl. Phys. **45**, 129 (1963).

[11] B. J. Verhaar, Nucl. Phys. **54**, 641 (1964).

[12] N. Onishi and S. Yoshida, Nucl. Phys. **80**, 367 (1966).

[13] A. Kamlah, Z. Phys. **216**, 52 (1968).

[14] R. Balian and E. Brezin, Nuov Cim. B **64**, 37 (1969).

[15] H. J. Mang, Phys. Pep. **18**, No. 6, 325 (1975).

[16] K. Hara and S. Iwasaki, Nucl. Phys. **A332**, 61 (1979).

[17] P. R. Rodríguez-Guzmán, J. L. Egido, and L. M. Robledo, Nucl. Phys. A **709**, 201 (2002).

[18] B. Bally and M. Bender, Phys. Rev. C **103**, 024315 (2021).

[19] J. A. Sheikh, J. Dobaczewski, P. Ring, L. M. Robledo, and C. Yannouleas, J. Phys. G: Nucl. Part. Phys. **48**, 123001 (2021).

[20] M. E. Peskin and D. V. Schroeder, *An Introduction to Quantum Field Theory* (Perseus Books, Cambridge, 1995).

[21] H. Yukawa, Proc. Phys.-Math. Soc. Jpn. **17**, 48 (1935); Prog. Theor. Phys. Suppl. **1**, 1 (1955).

[22] G. Bertsch, J. Borysowicz, H. McManus, and W. G. Love, Nucl. Phys. A **284**, 399 (1977).

[23] W. N. Cottingham, M. Lacombe, B. Loiseau, J. M. Richard, and R. Vinh Mau, Phys. Rev. D **8**, 800 (1973).

[24] M. Lacombe, B. Loiseau, J. M. Richard, R. Vinh Mau, J. Côté, P. Pirés, and R. de Tourreil, Phys. Rev. C **21**, 861 (1980).

[25] N. Anantaraman, H. Toki, and G. F. Bertsch, Nucl. Phys. A **398**, 269 (1983).

[26] H. Nakada, Phys. Rev. C **68**, 014316 (2003).

[27] H. Nakada, Phys. Rev. C **87**, 014336 (2013).

[28] H. Nakada, Int. J. Mod. Phys. E **29**, 1930008 (2020).

[29] D. Davesne, A. Pastore, and J. Navarro, Prog. Part. Nucl. Phys. **120**, 103870 (2021).

[30] H. Nakada and K. Sugiura, Prog. Theor. Exp. Phys. **2014**, 033D02 (2014); **2016**, 099201 (2016).

[31] Y. Suzuki, H. Nakada, and S. Miyahara, Phys. Rev. C **94**, 024343 (2016).

[32] S. Miyahara and H. Nakada, Phys. Rev. C **98**, 064318 (2018).

[33] K. Hara, S. Iwasaki, and K. Tanabe, Nucl. Phys. **A332**, 69 (1979).

[34] K. Hara and S. Iwasaki, Nucl. Phys. **A348**, 200 (1980).

[35] K. W. Schmid, Prog. Part. Nucl. Phys. **52**, 565 (2004).

[36] M. Bender, P. H. Heenen, and P. G. Reinhard, Rev. Mod. Phys. **75**, 121 (2003).

[37] M. Bender and P. H. Heenen, Phys. Rev. C **78**, 024309 (2008).

[38] L. M. Robledo, T. R. Rodríguez, and P. R. Rodríguez-Guzmán, J. Phys. G: Nucl. Part. Phys. **46**, 013001 (2019).

[39] K. Abe and H. Nakada, Phys. Rev. C **106**, 054317 (2022).

[40] N. Ishii, S. Aoki, and T. Hatsuda, Phys. Rev. Lett. **99**, 022001 (2007).

[41] S. Aoki, T. Hatsuda, and N. Ishii, Prog. Theor. Phys. **123**, No.1, 89 (2010).

[42] S. Aoki, T. Doi, T. Hatsuda, Y. Ikeda, T. Inoue, N. Ishii, K. Murano, H. Nemura, and K. Sasaki, Prog. Theor. Exp. Phys. **2012**, 01A105 (2012).

[43] M. Creutz, *Quarks, gluons, and lattices* (Cambridge monographs on mathematical physics, 1983).

[44] E. Epelbaum, H.-W. Hammer, and U.-G. Meißner, Rev. Mod. Phys. **81**, 1773 (2009).

[45] R. Machleidt and D. R. Entem, J. Phys.: Conf. Ser. **20**, 77 (2005).

[46] R. Machleidt and D. R. Entem, Phys. Rep. **503**, 1 (2011).

[47] T. Hamada and I. D. Johnston, Nucl. Phys. **34**, 382 (1962).

[48] G. H. Herling and T. T. S. Kuo, Nucl. Phys. A **181**, 113 (1972).

[49] J. B. McGrory and T. T. S. Kuo, Nucl. Phys. A **247**, 283 (1975).

[50] P. V. Reid, Ann. Phys. (N.Y.) **50**, 411 (1968).

[51] R. Machleidt, K. Holinde, and Ch. Elster, Phys. Rep. **149**, 1 (1987).

[52] J. Haidenbauer and K. Holinde, Phys. Rev. C **40**, 2465 (1989).

[53] L. Coraggio, A. Covello, A. Gargano, N. Itaco, and T. T. S. Kuo, Phys. Rev. C **58**, 3346 (1998).

[54] K. A. Brückner and C. A. Levinson, Phys. Rev. **97**, 1344 (1955).

[55] K. A. Brückner, Phys. Rev. **100**, 36 (1955).

[56] K. A. Brückner and J. L. Gammel, Phys. Rev. **109**, 1023 (1958).

[57] M. Hjorth-Jensen, T. T. S. Kuo, and E. Osnes, Phys. Rep. **261**, 125 (1995).

[58] T. H. R. Skyrme, Phil. Mag. **1**, 1043 (1956).

[59] D. Vautherin and D. M. Brink, Phys. Rev. C **5**, 626 (1972).

[60] J. W. Negele and D. Vautherin. Phys. Rev. C **5**, 1472 (1972).

[61] D. Vautherin, Phys. Rev. C **7**, 296 (1973).

[62] J. W. Negele and D. Vautherin. Phys. Rev. C **11**, 1031 (1975).

[63] M. J. Giannoni and P. Quentin, Phys. Rev. C **21**, 2076 (1980).

[64] P. Hohenberg and W. Kohn, Phys. Rev. **136**, B864 (1964).

[65] W. Kohn and L. J. Sham, Phys. Rev. **140**, A1133 (1965).

[66] V. Sahni, K.-P. Bohnen, and M. K. Harbola, Phys. Rev. A **37**, 1895 (1988).

[67] J. J. Sakurai, *Modern Quantum Mechanics*, Revised Edition (Addison-Wesley Reading, 1994).

[68] H. A. Bethe, Phys. Rev. **103**, 1353 (1956).

[69] H. A. Bethe and J. Goldstone, Proc. Roy. Soc. A **238**, 551 (1957).

[70] J. Goldstone, Proc. Roy. Soc. A **239**, 267 (1957).

[71] Y. Nambu and G. Jona-Lasinio, Phys. Rev. **122**, 345 (1961).

[72] Y. Nambu and G. Jona-Lasinio, Phys. Rev. **124**, 246 (1961).

[73] A. R. Edmonds, *Angular Momentum in Quantum Mechanics* (Princeton, New Jersey, 1974).

[74] D. A. Varshalovich, A. N. Moskalev, and V. K. Khersonskii, *Quantum Theory of Angular Momentum* (World Scientific, Singapore, 1988).

[75] R. Kubo, J. Phys. Soc. Jpn. **17**, No. 7, 1100 (1962).

[76] B. R. Mottelson and J. G. Valatin, Phys. Rev. Lett. **5**, 511 (1960).

[77] J. M. Blatt and V. F. Weisskopf, *Theoretical Nuclear Physics* (John Wiley & Sons, New York, 1952).

[78] J. M. Eisenberg and W. Greiner, *Nuclear Theory, Vol. 2; Excitation Mechanisms of the Nucleus* (North-Holland, Amsterdam, 1988).

[79] G. Alaga, K. Alder, A. Bohr, and B. R. Mottelson, Mat. Fys. Medd. Dan. Vid. Selsk. **29**, No. 9 (1955).

[80] M. Matsuo, K. Mizuyama, and Y. Serizawa, Phys. Rev. C **71**, 064326 (2005).

[81] H. Nakada and M. Sato, Nucl. Phys. A **699**, 511 (2002); **714**, 696 (2003).

[82] H. Nakada, Nucl. Phys. A **764**, 117 (2006); **801**, 169 (2008).

[83] H. Nakada, Nucl. Phys. A **808**, 47 (2008).

[84] J. W. Negele and H. Orland, *Quantum Many-Particle Systems* (Addison-Wesley, 1995).

[85] H. Nakada, Prog. Theor. Exp. Phys. **2016**, 063D02 (2016); 099101 (2016).

[86] C. Bloch and A. Messiah, Nucl. Phys. **39**, 95 (1962).

[87] T. Ono, Y. R. Shimizu, N. Tajima, and S. Takahara, Phys. Rev. C **82**, 034310 (2010).

[88] K. Neergård and E. Wüst, Nucl. Phys. A **402**, 311 (1983).

[89] L. M. Robledo, Phys. Rev. C **79**, 021302(R) (2009).

[90] T. Sumikama, K. Yoshinaga, H. Watanabe, S. Nishimura, Y. Miyashita, K. Yamaguchi, *et al.*, Phys. Rev. Lett. **106**, 202501 (2011).

[91] N. Paul, A. Corsi, A. Obertelli, P. Doornenbal, G. Authelet, H. Baba, *et al.*, Phys. Rev. Lett. **118**, 032501 (2017).

[92] P. Doornenbal, H. Scheit, S. Takeuchi, N. Aoi, K. Li, M. Matsushita, *et al.*, Phys. Rev. Lett. **111**, 212502 (2013).

[93] T. Baumann, A. M. Amthor, D. Bazin, B. A. Brown, C. M. Folden III, A. Gade, *et al.*, Nature **449**, 1022 (2007).

[94] H. Nakada and K. Takayama, Phys. Rev. C **98**, 011301(R) (2018).

[95] C. J. Lister, M. Campbell, A. A. Chishti, W. Gelletly, L. Goettig, R. Moscrop, *et al.*, Phys. Rev. Lett. **59**, 1270 (1987).

[96] N. J. Stone, Atomic Data and Nuclear Data Tables **111-112**, 1 (2016).

[97] H. L. Crawford, P. Fallon, A. O. Macchiavelli, P. Doornenbal, N. Aoi, F. Browne, *et al.*, Phys. Rev. Lett. **122**, 052501 (2019).

[98] H. Nakada, Prog. Theor. Exp. Phys. **2017**, 023D03 (2017).

[99] J. L. Egido and L. M. Robledo, in *Extended Density Functionals in Nuclear Structure Physics*, edited by G. A. Lalazissis, P. Ring, and D. Vretenar (Springer, Berlin, 2004), Chap. 10, pp. 269−302.

[100] N. A. Wiegmann, Can. J. Math. **7**, 191 (1955).

[101] F. Zhang, Lin. Alg. Appl. **251**, 21 (1997).